University of Alberta

Simulation of Freshwater Processes Associated with the
Canadian Arctic Archipelago

by

Xianmin Hu

A thesis submitted to the Faculty of Graduate Studies and Research
in partial fulfillment of the requirements for the degree of

Doctor of Philosophy

Department of Earth and Atmospheric Sciences

Fall 2013
Edmonton, Alberta

Abstract

This thesis presents the numerical simulations related to freshwater processes within the Canadian Arctic Archipelago (CAA) using a coupled ocean and sea ice pan-Arctic model based on NEMO v3.1.

In this study, two major routes for the export of Pacific water to the North Atlantic, via either Fram Strait or the CAA, are identified using three dimensional (3D) Lagrangian particle tracking. More than 70% of the Pacific water is exported out of the Arctic Ocean within 10 years using either the Transpolar route or the Alaskan route. About 50% of the above water is delivered to the North Atlantic through the central CAA. The proportion of Pacific water transported along the two routes is found to be associated with the spatial distribution of freshwater within the Canadian Basin.

The impacts of Greenland melt are studied through a series of sensitivity experiments that add different amounts of freshwater along the coast of Greenland. Compared to the control run, enhanced Greenland melt significantly increases the freshwater content within Baffin Bay, raising the dynamic heights and further weakening the CAA throughflows. Meanwhile, a strengthened outflow through Fram Strait is produced to compensate for the reductions in volume and freshwater transport through the CAA.

Using forcing data from global climate models under the IPCC 20C3M and A1B climate scenarios, sea ice and surface ocean conditions within the CAA and adjacent regions are studied in detail. Remarkable changes in sea ice (concentration and thickness) are shown in the simulation from the mid 2020s to the mid 2060s. A shrinking of 65% in concentration and a thinning of 75% in thickness are estimated over the 40 years. Lower albedo results in more heat absorbed by the ocean, increasing the sea surface temperature,

especially in summer. However, sea surface salinity within the CAA does not become fresher under the context of ice melting but demonstrates a strong decadal oscillation. Also an increase in the Arctic Ocean freshwater storage is simulated. Change in the sea surface height in Baffin Bay and Canadian Basin impacts the central CAA throughflow and pathway of Pacific water in the Arctic Ocean in the future.

Acknowledgements

I would like to express my sincere appreciation to my supervisor Dr. Paul G. Myers for his support and encouragement during my PhD study. His knowledge, advice and confidence inspired me these ideas and kept on the track to my goal. His careful editing greatly improved this thesis.

Besides my supervisor, I also would like to thank all the rest of my committee members Dr. Andrew B.G. Bush and Dr. Christian Haas for their insightful advices during my study. Thank my examiners Dr. Gerhard W. Reuter and Dr. Bruno Tremblay for their valuable comments to help me get closer to my degree.

Thanks also go to all my colleagues no matter how long we had been together and where you are now. Big thanks to Praveen Veluthedathekuzhiyil (whose last name is even longer than my thesis), Laura Castro de la Guardia, Duanni Mary Qian, Claudia Wekerle for their valuable discussion and kind assistance in my study.

Last but not least, all my rocky friends and coffee mates, especially Linglin Chu, Andreas Enggist, Hongwen Zhao, Yi Zhao, Rares Bistran, Jean-Baptiste Tary, are so awesome that made me a happy and enjoyable life in Edmonton!

Contents

List of Tables

List of Figures

Chapter 1

Introduction

1.1 Arctic Ocean stratification

The Arctic Ocean is a Mediterranean-style ocean with limited communication with the other main oceans (e.g., *Jones*, 2001). It connects the Pacific Ocean through the narrow ($\sim 85\,km$), shallow ($\sim 50\,m$) Bering Strait, and the Atlantic Ocean via the Canadian Arctic Archipelago (CAA) channels, Fram Strait and Barents Sea Opening (figure 1.1). The Arctic Ocean consists of a broad continental shelf on the Eurasian side, a narrow shelf on the American side, and a deep central basin. There are seven epicontinental seas, i.e. the Barents, Kara, Laptev, East Siberian, Chukchi, Beaufort, and Lincoln Seas. The deep basin is divided by the Lomonosov Ridge ($\sim 1600\,m$) into two major sub-basins: the Eurasian Basin and Canadian Basin. The Eurasian Basin is further divided into the deeper Amundsen Basin ($\sim 4500\,m$) and relatively shallower Nansen Basin ($4000\,m$) by the Gakkel Ridge. The Canadian Basin is separated by the Alpha and Mendeleyev ridges into the Makarov Basin ($\sim 4000\,m$) and the Canada Basin ($3800\,m$). These submarine ridges play an important role in setting up the large scale Arctic Ocean oceanographic circulation. More detailed physiographic information about the Arctic Ocean is given by *Jakobsson et al.* (2004).

Circulation patterns are different for the surface and deeper layers in the Arctic Ocean. At the surface ($< 200\,m$), the circulation of the water (sea

ice as well) is dominated by an anti-cyclonic flow, centered in the Beaufort Gyre, north of the North American continent, with the strong Transpolar Drift (TPD) flowing from the Laptev Sea to the north coast of Greenland, crossing the North Pole area. The deeper layer circulation is basically cyclonic along the continental slope and basin edges. More description about the circulation of Pacific and Atlantic waters is given later in chapter 3.

The Arctic Ocean waters are strongly stratified. In polar oceans, as the temperature does not change much from the surface to the bottom, the vertical stratification is determined by salinity difference (e.g *Aagaard et al.*, 1981; *Sigman et al.*, 2004; *Carmack*, 2007). The Arctic Ocean receives water mass mainly from two major sources, saline water of Atlantic origin entering the Arctic Ocean through Fram Strait and Barents Sea, and fresher warmer Pacific water flowing into the Arctic Ocean through Bering Strait. These two waters, combined with other freshwater sources, i.e., river discharge from the Eurasian and North America continents and positive precipitation minus evaporation (P - E), result in the three typical layers of the Arctic Ocean (*Rudels et al.*, 1994). On the top lies a well-mixed surface layer of very fresh waters with near-freezing temperature attributed to the river runoff and sea ice meltwater, followed by a pronounced cold halocline with salinity increasing rapidly with depth, below which is the warm and salty water of Atlantic origin spreading in a depth range of 200 to 1000 m. The deep waters, which have slowly decreasing temperature and increasing salinity with depth, fill the rest of the deeper basins.

Among the above three layers, the cold halocline plays a significant role in the maintenance of the Arctic Ocean stratification. Not only does it fill the density gap between the warm saline Atlantic layer and the cold very fresh surface layer, but it also acts as a strong pycnocline, allowing the surface layer to accumulate more freshwater, e.g., precipitation, river runoff and ice meltwater, and thus intensify the stratification (*Sigman et al.*, 2004). In addition, it insulates and limits the heat transfer from the warm Atlantic layer to the surface layer, which helps maintain the ice cover (*Martin and Cavalieri*, 1989; *Kikuchi et al.*, 2004). Previous studies (*Aagaard et al.*, 1981; *Melling and Lewis*, 1982; *Martin and Cavalieri*, 1989) have shown that the halocline

is unlikely to be locally formed by vertical mixing but is the product of cold, brine-enriched waters from the shelves. Because of different sources and processes, the haloclines within the different basins show different features (*Rudels et al.*, 2001). The halocline within the Eurasian Basin is characterized by a salinity of 34.3 and an almost constant close to freezing temperature down to $100\,m$. This water mass is defined as the lower halocline because it is denser than the halocline water in the Canadian Basin and can advect into the Canadian Basin. In contrast, the halocline in the Canada Basin has a wider salinity range (32–34.5) and a much more complex temperature structure, mainly due to multiple sources of water, especially the inflow of low salinity Pacific water from Bering Strait.

The thickness and distribution of the halocline impacts local processes ranging from heat storage and ice melting to biological productivity, as well as the steric heights and the large-scale circulation in the Arctic Ocean. The relatively fresher outflows from the Arctic Ocean also could trigger a salinity anomaly event in the North Atlantic similar to the Great Salinity Anomaly (GSA) of the 1970s (*Dickson et al.*, 1988). An increase in such outflow has been suggested to potentially affect the stratification and convection within the Greenland and Labrador Seas, and thus the meridional overturning circulation and global energy and mass distribution (e.g. *Aagaard and Carmack*, 1989; *Goosse et al.*, 1997; *Komuro and Hasumi*, 2005; *Curry and Mauritzen*, 2005; *Koenigk et al.*, 2007), although there are still some open questions such as the exchange of freshwater between the Labrador shelf and the interior of the Labrador Sea (e.g., *Rudels et al.*, 2005; *Myers*, 2005; *Fratantoni and McCartney*, 2010).

1.2 Arctic Ocean freshwater system

1.2.1 Calculation of freshwater

To estimate the salt-dependent stratification within the Arctic Ocean and its variation, several freshwater related definitions are introduced. Freshwater

can be divided into two categories, liquid and solid. Without specification, freshwater usually refers to the liquid phase freshwater because 'sea ice' is used instead of 'solid phase freshwater'. Freshwater is defined as the volume of pure freshwater needed to add into or be extracted from a water sample to reach a reference salinity (S_{ref}). In the case of the Arctic Ocean, a value of 34.8, which is the averaged salinity of the Arctic Ocean waters (*Aagaard and Carmack*, 1989), is commonly adopted. Freshwater content is used to describe how much freshwater there is within the water column at a given location (x, y):

$$FW_{content}(x,\, y) \,=\, \int_{H}^{0} 1 - \frac{S(x,y,z)}{S_{ref}}\, dz \tag{1.1}$$

where H is the depth of the water column, $S(x, y, z)$ is the salinity and z is the vertical coordinate.

By summing up the freshwater content within a given area, e.g., a basin, it results in the freshwater storage:

$$FW_{storage} \,=\, \iiint_{H}^{0} 1 - \frac{S(x,y,z)}{S_{ref}}\, dz\, dy\, dx \tag{1.2}$$

To calculate the freshwater budget, it also requires the freshwater flux through a section with a length of L:

$$FW_{flux} \,=\, \int_{0}^{L} \int_{H}^{0} (1 - \frac{S(l,z)}{S_{ref}}) U(l,z)\, dz\, dl \tag{1.3}$$

where l is the along section direction, and $U(l, z)$ is the normal to section velocity.

The freshwater (flux, content, and storage) is also a function of time.

1.2.2 Arctic Ocean freshwater storage and budget

The storage and budget of the Arctic Ocean freshwater were first systematically estimated by *Aagaard and Carmack* (1989), and later reassessed by *Serreze et al.* (2006) with updated observations. *Dickson et al.* (2007) also summarized previous studies of the Arctic Ocean freshwater fluxes, including numerical simulation results. With a reference salinity of 34.8, *Serreze et al.* (2006) estimated the annual mean of all phases freshwater stored within the

Arctic Ocean (enclosed by Bering Strait, the CAA, Fram Strait and Barents Sea Opening) to be as high as $84000\,km^3$, $10000\,km^3$ of which is for the sea ice. The freshwater is not evenly distributed in space. Most of the Arctic Ocean's freshwater is stored in the upper $200\,m$ of the deep basins, particularly the Beaufort Gyre of the Canadian Basin. This is a function of Ekman convergence caused by anti-cyclonic atmospheric circulation (e.g., *Aagaard and Carmack*, 1989; *Proshutinsky et al.*, 2002, 2009; *Serreze et al.*, 2006).

The annual input of freshwater is about 10% of the total freshwater storage in the Arctic Ocean (*Serreze et al.*, 2006). Among the three major sources, runoff contributes 38%, $3200 \pm 110 km^3$ estimated from both gauged and ungauged rivers (1980–1999), Pacific inflow contributes 30%, $2500 \pm 300 km^3$ from *Woodgate and Aagaard* (2005)'s observations (1990–2004), and P-E accounts for 24%, $2000 \pm 200 km^3$ based on the European Centre for Medium Range Forcasts (ECMWF) ERA-40 reanalysis data (1979–2001). The fresh Norwegian Coastal Current ($250 \pm 50\,km^3$) and the deep saline outflow through Fram Strait ($500 \pm 130\,km^3$) also act as small sources of Arctic Ocean freshwater.

The surplus of freshwater received by the Arctic Ocean is partly balanced by the sea ice and oceanic export through the lateral straits (Fram Strait, Barents Sea Opening and the CAA channels). As most of the salt is rejected into the ocean underneath during the ice formation process, freezing is the most effective way to distill the ocean in the polar region (*Aagaard and Carmack*, 1989). Sea ice delivered to south through Fram Strait, where basically all ice export from the Arctic Ocean occurs, contributes a loss of freshwater of $2300 \pm 340\,km^3$ per year, which is equivalent to the liquid freshwater export by the surface southward flows ($2400 \pm 400 km^3$ per year) (*Serreze et al.*, 2006). The inflow of saline Atlantic water as the West Spitsbergen Current and Barents Sea Branch provide each year freshwater sinks of $760 \pm 320\,km^3$ and $340 \pm 80\,km^3$, respectively.

The CAA is a complex network of narrow straits, shallow ocean sills and basins, providing the other major outlet for the Arctic Ocean water to the Atlantic. In the past, the CAA has had a lack of observations due to the harsh weather and severe ice condition (*Prinsenberg and Hamilton*, 2005), and it has

not been well resolved in numerical models (e.g. *Kliem and Greenberg*, 2003; *Solomon et al.*, 2007). The CAA throughflow was considered to be small, and its contribution the Arctic Ocean freshwater budget was underestimated even in *Aagaard and Carmack* (1989), of only $920\,km^3$ per year. However, combined with the three years of measurements (1998–2000) and model simulations, *Prinsenberg and Hamilton* (2005) later found it could be more than three times larger than previous estimate, of 2800–$3500\,km^3$ per year, suggesting the CAA throughflow to be the largest contributor of the oceanic freshwater outflow. This is supported by later longer term observations (*Melling et al.*, 2008) and high resolution numerical model simulations (e.g. *Aksenov et al.*, 2010; *McGeehan and Maslowski*, 2012; *Jahn et al.*, 2012). Recent satellite observations (*Kwok*, 2006; *Agnew et al.*, 2008) have shown there is also a net ice flux into the Arctic Ocean from the western CAA openings (Amundsen Gulf and M'Clure Strait). Ice exported to Baffin Bay is small and suggested to be locally formed within the CAA, $\sim$ 100–$160\,km^3$ per year (e.g *Agnew et al.*, 2008; *Prinsenberg and Hamilton*, 2005; *Lietaer et al.*, 2008).

1.2.3 Arctic Ocean freshwater variation

In recent years, dramatic changes have been observed in the Arctic, including warming (e.g., *Walsh et al.*, 1996; *Jones and Moberg*, 2003), shifting of the large scale circulation (e.g., *Walsh et al.*, 1996; *Maslanik et al.*, 2007; *Overland et al.*, 2012) in the atmosphere, shrinking of ice extent/area (e.g., *Parkinson et al.*, 1999; *Serreze et al.*, 2007; *Parkinson and Cavalieri*, 2008; *Comiso and Nishio*, 2008), thinning of ice thickness (e.g., *Rothrock et al.*, 1999; *Holloway and Sou*, 2002; *Rothrock et al.*, 2008; *Haas et al.*, 2008; *Kwok et al.*, 2009; *Kwok and Rothrock*, 2009), changing of the spatial pattern in ice drifting (e.g., *Kwok*, 2000, 2009), warming of the ocean both at the surface (*Steele et al.*, 2008), and in the Atlantic layer (e.g., *Carmack et al.*, 1995; *Polyakov et al.*, 2007; *Dmitrenko et al.*, 2008; *Polyakov et al.*, 2010), increasing river discharge (e.g., *Peterson et al.*, 2002) and enhanced melting of ice sheets (e.g. *Velicogna*, 2009; *van den Broeke et al.*, 2009; *Sharp et al.*, 2011; *Bamber et al.*, 2012).

These processes can all directly or indirectly affect the Arctic Ocean freshwater system.

Large inter-annual variability has been noticed in the Arctic Ocean liquid freshwater storage, especially within the Beaufort Gyre. The data used for freshwater estimated by *Serreze et al.* (2006) have some biases in sampling, as more collection was done in the 1970s and 1980s, when there was likely to have been more freshwater stored in the Arctic Ocean. From the 1980s, if not earlier, until the late 1990s, significant amounts of freshwater was released from the central Arctic Ocean. This is shown both in the sparse observational data (*Polyakov et al.*, 2008) and model simulations (*Köberle and Gerdes*, 2007; *Gerdes et al.*, 2008; *Long et al.*, 2012). After that, a quick recovery led to increased accumulation of freshwater, which has been continuing in recent years (*Proshutinsky et al.*, 2009; *McPhee et al.*, 2009; *Long et al.*, 2012; *Rabe et al.*, 2011). In their simulation, *Long et al.* (2012) found an increase of $2.5m$ of the freshwater between 1997 and 2009 following a decrease of $\sim 1\,m$ prior to that time period. Although these numbers are smaller than the observations (*Proshutinsky et al.*, 2009; *McPhee et al.*, 2009), the trends agree well with the data.

Two major factors have been proposed to explain the inter-annual variation in freshwater content. One is the ice transformation (formation and melting), and the other one is the Ekman pumping associated with the wind stress curl. *Polyakov et al.* (2008) studied the freshwater changes over the past 100 years using the hydrographic measurements in the high latitudes and concluded that the ice production and sustained draining of freshwater from the Arctic Ocean due to the winds drove the salinification of the upper Arctic Ocean in the past decades. Although they lacked historical data to quantify the impacts. Based on mooring observations, *Proshutinsky et al.* (2009) found, at least in recent years for the Beaufort Sea, the rapid increasing of freshwater content can be explained only by a positive trend of Ekman pumping caused by intensification of the anticyclonic wind circulation. This is partly supported by a later numerical simulation done by (*Long et al.*, 2012). *Long et al.* (2012) found that during 2004–2009, the variation of freshwater content within the

Beaufort Sea is mainly driven by the Ekman pumping while the ice processes contribute only one third of the total freshwater changes. In other time periods (1980–1987, and 1994–1997), the contributions of Ekman transport and ice transformation are similar. As the wind circulation patterns also affect the ice growth and export (e.g., *Köberle and Gerdes*, 2003), the large scale atmosphere circulation must play a profound role in regulating the variation of Arctic Ocean freshwater content. This has been found in various other model studies (e.g., *Condron et al.*, 2009; *Jahn et al.*, 2010).

In addition to the quantity of freshwater stored within the Arctic Ocean, its spatial pattern also varies. In the Beaufort Sea, the center of maximum freshwater content has shifted to the southeast in recent years (*Proshutinsky et al.*, 2009; *McPhee et al.*, 2009). How do these changes affect the oceanic circulation, e.g., via the sea surface height (SSH), will be an interesting topic for future study (e.g. *Lique et al.*, 2010).

1.3 Thesis objectives and outline

Many studies have been conducted to estimate the budget of Arctic Ocean freshwater, as previously mentioned. However, how does the state of this freshwater, as well as its different sinks and sources, affect the ocean circulation, quantitatively is still not well understood. Thus, to have a better understanding of the Arctic Ocean freshwater system, this thesis will focus on:

- circulation of the Pacific water within the Arctic Ocean and its pathways exiting to the Atlantic side, particularly through the CAA channels
- the impact of enhanced Greenland melt on adjacent waters and circulation, focusing on Baffin Bay and the CAA throughflow
- projected future CAA sea ice conditions as well as ocean surface properties (temperature, salinity) based on a future climate scenario

- projected Arctic Ocean freshwater budget and the CAA throughflow in a future climate scenario

The pathways of Pacific water have been mainly studied using observed chemical tracers and nutrients at limited locations and during specific time periods. In situ data with high resolution both in space and time are not available so far. Also the tracing of Pacific water directly using currents measurements is not workable in practice. In this study, we utilize a coupled ocean sea ice pan-Arctic model to produce the ocean fields (velocities and tracers) under climatologic forcing. The model is based on the Nucleus for European Modelling of the Ocean (NEMO) numerical framework version 3.1 (*Madec and the NEMO team*, 2008), which is described in chapter 2. A Lagrangian analysis package, ARINE (*Blanke and Raynaud*, 1997; *Blanke et al.*, 1999), is used to detect the pathway of the Pacific water within the Arctic Ocean. The volume of Pacific water carried by each major route through the Fram Strait and the CAA main straits are quantitatively estimated. Also the shifting of Pacific water routes caused by the spatial distribution of Arctic Ocean freshwater content are studied. Details of this work are given in chapter 3.

In our model, there is no glacier module. To study the second objective, we set up a series of sensitivity experiments by modifying the amount of runoff from west Greenland. The amount of enhanced melt ranges from almost zero to $1580\,km^3$ per year. Also the seasonal variation and spatial pattern of the melting are considered in the experiments. The results are provided in chapter 4.

The simulation of future Arctic Ocean freshwater storage and outflows as well as the CAA ice conditions is carried out with atmospheric forcing from the twentieth century simulation (20C3M, 1970–1999) and Special Report on Emission Scenario (SRES) A1B scenario (2000–2100) simulations provided by UK Met Office Hadley Centre Coupled Ocean Atmosphere GCM (HadCM3). The open boundary conditions of the ocean are taken from the corresponding simulations of Canadian Centre for Climate Modelling and Analysis (CCCma) CGCM3.1. The experiment setup is discussed in detail in chapter 5. Also the

ice and surface ocean conditions in different time periods are summarized in chapter 5. The trends in Arctic Ocean freshwater budgets, the CAA throughflow and possible changes of Pacific water pathways in the future are discussed in chapter 6. A summary and discussion of possible future work are detailed in chapter 7.

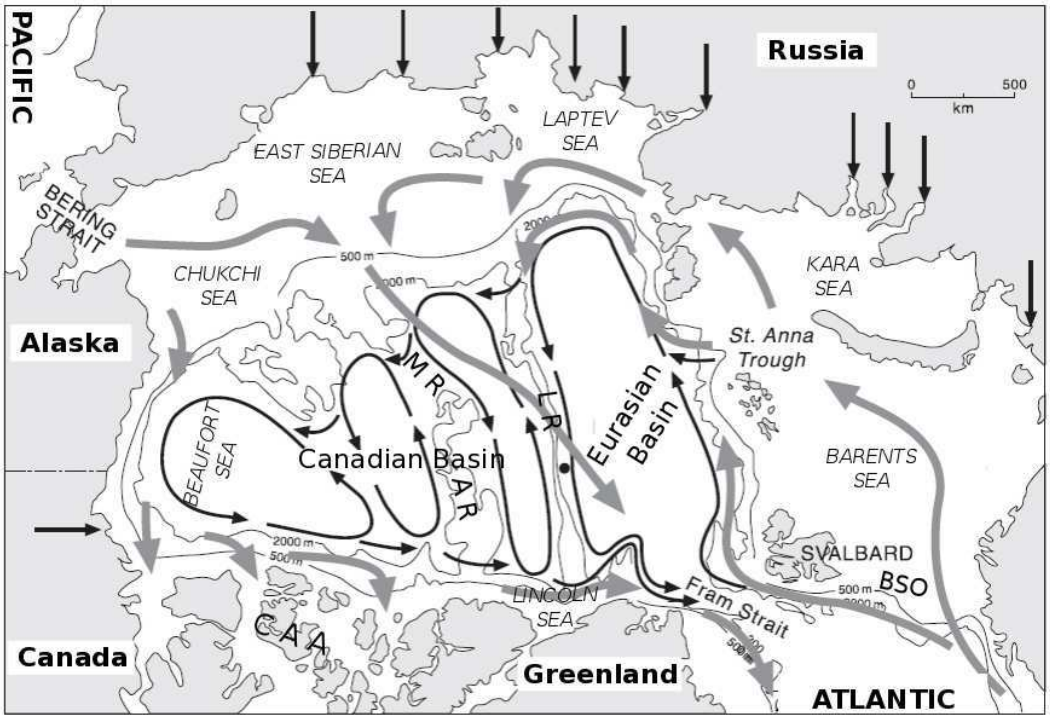

Figure 1.1: Schematic circulation of the Arctic Ocean circulation (gray arrows: surface water; black arrows: deep layer; strait arrows: river mouth; contour lines: water depth; MR: Mendeleyev Ridge; AR: Alpha Ridge; LR: Lomonosov Ridge; CAA: Canadian Arctic Archipelago; BSO: Barents Sea Opening). Figure is adapted from *Jones* (2001).

Bibliography

Aagaard, K., and E. C. Carmack (1989), The role of sea ice and other fresh water in the Arctic circulation, *Journal of Geophysical Research*, *94*(C10), 14,485–14,498.

Aagaard, K., L. K. Coachman, and E. C. Carmack (1981), On the halocline of the Arctic Ocean, *Deep Sea Research Part A. Oceanographic Research Papers*, *28*(6), 529–545.

Agnew, T., A. Lambe, and D. Long (2008), Estimating sea ice area flux across the Canadian Arctic Archipelago using enhanced AMSR-E, *Journal of Geophysical Research*, *113*(C10).

Aksenov, Y., S. Bacon, A. C. Coward, and N. P. Holliday (2010), Polar outflow from the Arctic Ocean: A high resolution model study, *Journal of Marine Systems*, *83*, 14–37.

Bamber, J., M. den Broeke, J. Ettema, J. Lenaerts, and E. Rignot (2012), Recent large increases in freshwater fluxes from Greenland into the North Atlantic, *Geophysical Research Letters*, *39*(19).

Blanke, B., and S. Raynaud (1997), Kinematics of the Pacific Equatorial Undercurrent: An Eulerian and Lagrangian approach from GCM results, *Journal of Physical Oceanography*, *27*(6), 1038–1053.

Blanke, B., M. Arhan, G. Madec, and S. Roche (1999), Warm water paths in the equatorial Atlantic as diagnosed with a general circulation model, *Journal of Physical Oceanography*, *29*(11), 2753–2768.

Carmack, E. C. (2007), The alpha/beta ocean distinction: A perspective on freshwater fluxes, convection, nutrients and productivity in high-latitude seas, *Deep Sea Research Part II: Topical Studies in Oceanography*, *54*(23-26), 2578–2598.

Carmack, E. C., R. W. Macdonald, R. G. Perkin, F. A. McLaughlin, and R. J. Pearson (1995), Evidence for warming of Atlantic water in the Southern Canadian Basin of the Arctic Ocean: Results from the Larsen-93 Expedition, *Geophysical Research Letters*, *22*(9), 1061–1064.

Comiso, J. C., and F. Nishio (2008), Trends in the sea ice cover using enhanced and compatible AMSR-E, SSM/I, and SMMR data, *Journal of Geophysical Research*, *113*(C2), C02S07.

Condron, A., P. Winsor, C. Hill, and D. Menemenlis (2009), Simulated response of the Arctic freshwater budget to extreme NAO wind forcing, *Journal of Climate*, *22*(9), 2422–2437.

Curry, R., and C. Mauritzen (2005), Dilution of the northern North Atlantic Ocean in recent decades, *Science*, *308*(5729), 1772.

Dickson, R., B. Rudels, S. Dye, M. Karcher, J. Meincke, and I. Yashayaev (2007), Current estimates of freshwater flux through Arctic and subarctic seas, *Progress in Oceanography*, *73*(3-4), 210–230.

Dickson, R. R., J. Meincke, S. Malmberg, and A. J. Lee (1988), The "great salinity anomaly" in the Northern North Atlantic 1968-1982, *Progress in Oceanography*, *20*(2), 103–151, doi:10.1016/0079.

Dmitrenko, I. A., I. V. Polyakov, S. A. Kirillov, L. A. Timokhov, I. E. Frolov, V. T. Sokolov, H. L. Simmons, V. V. Ivanov, and D. Walsh (2008), Toward a warmer Arctic Ocean: Spreading of the early 21st century Atlantic Water warm anomaly along the Eurasian Basin margins, *Journal of Geophysical Research*, *113*(C5), C05,023, doi:10.1029/2007JC004158.

Fratantoni, P. S., and M. S. McCartney (2010), Freshwater export from the Labrador Current to the North Atlantic Current at the Tail of the Grand Banks of Newfoundland, *Deep Sea Research Part I: Oceanographic Research Papers*, *57*(2), 258–283.

Gerdes, R., M. Karcher, C. Köberle, and K. Fieg (2008), Simulating the long-term variability of liquid freshwater export from the Arctic Ocean, in *Arctic–Subarctic Ocean Fluxes: Defining the Role of the Northern Seas in Climate*, edited by R. Dickson, J. Meincke, and P. Rhines, pp. 405–425, Springer Netherlands, doi:10.1007/978-1-4020-6774-7_18.

Goosse, H., T. Fichefet, and J.-M. Campin (1997), The effects of the water flow through the Canadian Archipelago in a global ice-ocean model, *Geophysical Research Letters*, *24*(12), 1507–1510, doi:10.1029/97GL01352.

Haas, C., A. Pfaffling, S. Hendricks, L. Rabenstein, J.-L. Etienne, and I. Rigor (2008), Reduced ice thickness in Arctic Transpolar Drift favors rapid ice retreat, *Geophysical Research Letters*, *35*(17), L17,501, doi:10.1029/2008GL034457.

Holloway, G., and T. Sou (2002), Has Arctic sea ice rapidly thinned?, *Journal of Climate*, *15*(13), 1691–1701.

Jahn, A., B. Tremblay, L. A. Mysak, and R. Newton (2010), Effect of the large-scale atmospheric circulation on the variability of the Arctic Ocean freshwater export, *Climate Dynamics*, *34*(2), 201–222.

Jahn, A., et al. (2012), Arctic Ocean freshwater: How robust are model simulations?, *Journal of Geophysical Research*, *117*(C8), C00D16, doi:10.1029/2012JC007907.

Jakobsson, M., A. Grantz, Y. Kristoffersen, R. Macnab, R. W. Macdonald, E. Sakshaug, R. Stein, and W. Jokat (2004), The Arctic Ocean: Boundary conditions and background information, in *The Organic Carbon Cycle in the Arctic Ocean*, pp. 1–32, Springer.

Jones, E. P. (2001), Circulation in the Arctic Ocean, *Polar Research*, *20*(2), 139–146.

Jones, P. D., and A. Moberg (2003), Hemispheric and large-scale surface air temperature variations: An extensive revision and an update to 2001, *Journal of Climate*, *16*(2), 206–223.

Kikuchi, T., K. Hatakeyama, and J. H. Morison (2004), Distribution of convective Lower Halocline Water in the eastern Arctic Ocean, *Journal of Geophysical Research*, *109*(C12), C12,030, doi:10.1029/2003JC002223.

Kliem, N., and D. A. Greenberg (2003), Diagnostic simulations of the summer circulation in the Canadian Arctic Archipelago, *Atmosphere-Ocean*, *41*(4), 273–289.

Köberle, C., and R. Gerdes (2003), Mechanisms determining the variability of Arctic sea ice conditions and export, *Journal of Climate*, *16*(17), 2843–2858.

Köberle, C., and R. Gerdes (2007), Simulated variability of the Arctic Ocean freshwater balance 1948-2001, *Journal of Physical Oceanography*, *37*(6), 1628–1644.

Koenigk, T., U. Mikolajewicz, H. Haak, and J. Jungclaus (2007), Arctic freshwater export in the 20th and 21st centuries, *Journal of Geophysical Research*, *112*(G4), G04S41, doi:10.1029/2006JG000274.

Komuro, Y., and H. Hasumi (2005), Intensification of the Atlantic deep circulation by the Canadian Archipelago throughflow, *Journal of Physical Oceanography*, *35*(5), 775–789.

Kwok, R. (2000), Recent changes in Arctic Ocean sea ice motion associated with the North Atlantic Oscillation, *Geophysical Research Letters*, *27*(6), 775–778.

Kwok, R. (2006), Exchange of sea ice between the Arctic Ocean and the Canadian Arctic Archipelago, *Geophysical Research Letters*, *33*(16), L16,501.

Kwok, R. (2009), Outflow of Arctic Ocean sea ice into the Greenland and Barents Seas: 1979–2007, *Journal of Climate*, *22*, 2438–2457.

Kwok, R., and D. A. Rothrock (2009), Decline in Arctic sea ice thickness from submarine and ICESat records: 1958–2008, *Geophysical Research Letters*, *36*(15), L15,501.

Kwok, R., G. F. Cunningham, M. Wensnahan, I. Rigor, H. J. Zwally, and D. Yi (2009), Thinning and volume loss of the Arctic Ocean sea ice cover: 2003–2008, *Journal of Geophysical Research*, *114*(C7), C07,005.

Lietaer, O., T. Fichefet, and V. Legat (2008), The effects of resolving the Canadian Arctic Archipelago in a finite element sea ice model, *Ocean Modelling*, *24*(3), 140–152.

Lique, C., A. M. Treguier, B. Blanke, and N. Grima (2010), On the origins of water masses exported along both sides of Greenland: A Lagrangian model analysis, *Journal of Geophysical Research*, *115*(C5), C05,019.

Long, Z., W. Perrie, C. L. Tang, E. Dunlap, and J. Wang (2012), Simulated Interannual Variations of Freshwater Content and Sea Surface Height in the Beaufort Sea, *Journal of Climate*, *25*(4), 1079–1095, doi:10.1175/2011JCLI4121.1.

Madec, G., and the NEMO team (2008), *NEMO ocean engine*, Note du Pôle de modélisation, Institut Pierre-Simon Laplace (IPSL), France, No 27, ISSN No 1288-1619.

Martin, S., and D. J. Cavalieri (1989), Contributions of the Siberian Shelf Polynyas to the Arctic Ocean intermediate and deep water, *Journal of Geophysical Research*, *94*(C9), 12,725–12.

Maslanik, J., S. Drobot, C. Fowler, W. Emery, and R. Barry (2007), On the Arctic climate paradox and the continuing role of atmospheric circulation in affecting sea ice conditions, *Geophysical Research Letters*, *34*(3), L03,711.

McGeehan, T., and W. Maslowski (2012), Evaluation and control mechanisms of volume and freshwater export through the Canadian Arctic Archipelago in a high-resolution pan-Arctic ice-ocean model, *Journal of Geophysical Research*, *117*(C8), C00D14, doi:10.1029/2011JC007261.

McPhee, M. G., A. Y. Proshutinsky, J. H. Morison, M. Steele, and M. B. Alkire (2009), Rapid change in freshwater content of the Arctic Ocean, *Geophysical Research Letters*, *36*(10), L10,602, doi:10.1029/2009GL037525.

Melling, H., and E. L. Lewis (1982), Shelf drainage flows in the Beaufort Sea and their effect on the Arctic Ocean pycnocline, *Deep Sea Research Part A. Oceanographic Research Papers*, *29*(8), 967–985.

Melling, H., et al. (2008), Fresh-water fluxes via Pacific and Arctic outflows across the Canadian polar shelf, *Arctic-Subarctic Ocean Fluxes: Defining the Role of the Northern Seas in Climate*, pp. 193–247.

Myers, P. G. (2005), Impact of freshwater from the Canadian Arctic Archipelago on Labrador Sea water formation, *Geophysical Research Letters*, *32*(6), L06,605.

Overland, J. E., J. A. Francis, E. Hanna, and M. Wang (2012), The recent shift in early summer Arctic atmospheric circulation, *Geophysical Research Letters*, *39*(19).

Parkinson, C. L., and D. J. Cavalieri (2008), Arctic sea ice variability and trends, 1979–2006, *Journal of Geophysical Research*, *113*(C7), C07,003.

Parkinson, C. L., D. J. Cavalieri, P. Gloersen, H. J. Zwally, and J. C. Comiso (1999), Arctic sea ice extents, areas, and trends, 1978–1996, *Journal of Geophysical Research*, *104*(C9), 20,837–20,856.

Peterson, B. J., R. M. Holmes, J. W. McClelland, C. J. Vorosmarty, R. B. Lammers, A. I. Shiklomanov, I. A. Shiklomanov, and S. Rahmstorf (2002), Increasing river discharge to the Arctic Ocean, *Science*, *298*(5601), 2171–2173.

Polyakov, I., et al. (2007), Observational program tracks Arctic Ocean transition to a warmer state, *Eos, Transactions American Geophysical Union*, *88*(40), 398.

Polyakov, I. V., et al. (2008), Arctic Ocean freshwater changes over the past 100 years and their causes, *Journal of Climate*, *21*(2), 364–384.

Polyakov, I. V., et al. (2010), Arctic Ocean warming contributes to reduced polar ice cap, *Journal of Physical Oceanography*, *40*(12), 2743–2756.

Prinsenberg, S. J., and J. Hamilton (2005), Monitoring the volume, freshwater and heat fluxes passing through Lancaster Sound in the Canadian Arctic Archipelago, *Atmosphere-Ocean*, *43*(1), 1–22.

Proshutinsky, A. Y., R. H. Bourke, and F. A. McLaughlin (2002), The role of the Beaufort Gyre in Arctic climate variability: Seasonal to decadal climate scales, *Geophysical Research Letters*, *29*(23), 2100.

Proshutinsky, A. Y., et al. (2009), Beaufort Gyre freshwater reservoir: State and variability from observations, *Journal of Geophysical Research*, *114*(C1), C00A10.

Rabe, B., M. Karcher, U. Schauer, J. M. Toole, R. A. Krishfield, S. Pisarev, F. Kauker, R. Gerdes, and T. Kikuchi (2011), An assessment of Arctic Ocean freshwater content changes from the 1990s to the 2006–2008 period, *Deep Sea Research Part I: Oceanographic Research*, *58*, 173–185.

Rothrock, D. A., Y. Yu, and G. A. Maykut (1999), Thinning of the Arctic sea-ice cover, *Geophysical Research Letters*, *26*(23), 3469–3472.

Rothrock, D. A., D. B. Percival, and M. Wensnahan (2008), The decline in arctic sea-ice thickness: Separating the spatial, annual, and interannual variability in a quarter century of submarine data, *Journal of Geophysical Research*, *113*, C05,003.

Rudels, B., E. P. Jones, L. G. Anderson, and G. Kattner (1994), On the intermediate depth waters of the Arctic Ocean, in *The Polar Oceans and Their*

Role in Shaping the Global Environment, edited by O. M. Johannessen, R. D. Muench, and J. E. Overland, pp. 33–46, American Geophysical Union, Washington, DC.

Rudels, B., E. P. Jones, U. Schauer, and P. Eriksson (2001), Two sources for the lower halocline in the Arctic Ocean, *ICES Annual Science Conference*.

Rudels, B., G. Bjork, J. Nilsson, P. Winsor, I. Lake, and C. Nohr (2005), The interaction between waters from the Arctic Ocean and the Nordic Seas north of Fram Strait and along the East Greenland Current: results from the Arctic Ocean-02 Oden expedition, *Journal of Marine Systems*, *55*(1-2), 1–30.

Serreze, M. C., et al. (2006), The large-scale freshwater cycle of the Arctic, *Journal of Geophysical Research*, *111*(C11), C11,010, doi:10.1029/2005JC003424.

Serreze, M. C., M. M. Holland, and J. Stroeve (2007), Perspectives on the Arctic's shrinking sea-ice cover, *Science*, *315*(5818), 1533–1536.

Sharp, M., D. O. Burgess, J. G. Cogley, M. Ecclestone, C. Labine, and G. J. Wolken (2011), Extreme melt on Canada's Arctic ice caps in the 21st century, *Geophysical Research Letters*, *38*(11), doi:10.1029/2011GL047381.

Sigman, D. M., S. L. Jaccard, and G. H. Haug (2004), Polar ocean stratification in a cold climate, *Nature*, *428*(6978), 59–63.

Solomon, S., D. Qin, M. Manning, Z. Chen, M. Marquis, K. B. Averyt, M. Tignor, H. L. Miller, et al. (2007), The physical science basis. Contribution of Working Group I to the Fourth Assessment Report of the Intergovernmental Panel on Climate Change, *4*.

Steele, M., W. Ermold, and J. Zhang (2008), Arctic Ocean surface warming trends over the past 100 years, *Geophysical Research Letters*, *35*(2), L02,614, doi:10.1029/2007GL031651.

van den Broeke, M., J. Bamber, J. Ettema, E. Rignot, E. Schrama, W. J. van de Berg, E. van Meijgaard, I. Velicogna, and B. Wouters (2009), Partitioning recent Greenland mass loss, *Science*, *326*(5955), 984–986, doi: 10.1126/science.1178176.

Velicogna, I. (2009), Increasing rates of ice mass loss from the Greenland and Antarctic ice sheets revealed by GRACE, *Geophysical Research Letters*, *36*(19), L19,503.

Walsh, J. E., W. L. Chapman, and T. L. Shy (1996), Recent decrease of sea level pressure in the central Arctic, *Journal of Climate*, *9*(2), 480–486.

Woodgate, R. A., and K. Aagaard (2005), Revising the Bering Strait freshwater flux into the Arctic Ocean, *Geophysical Research Letters*, *32*(2), L02,602.

Chapter 2

Nucleus for European Modelling of the Ocean (NEMO)

NEMO is a state-of-art modeling framework for oceanographic research, operational oceanography, seasonal forecasting and climate studies. It includes five major components in the latest version, the blue ocean (ocean dynamics), the white ocean (sea ice), the green ocean (biogeochemistry), the adaptive mesh refinement software and the assimilation component. The official announcement of NEMO is available from `http://www.nemo-ocean.eu/`. In this chapter we will only focus on the details of modules used in this study, that is, the ocean and sea ice parts.

2.1 Ocean component

The ocean component of NEMO has been developed from the Océan PArallélisé (OPA), which is a primitive equation model for both global and regional ocean circulation simulations (*Madec et al.*, 1998). An updated reference manual is published by (*Madec and the NEMO team*, 2008).

In OPA, the ocean is described as a set of primitive equations (section 2.1) written in a curvilinear coordinate system with the following six assumptions:

- Spherical earth approximation

It simplifies the earth gravity at a given point to be a function of the distance between the core and that point. Thus the geopotential surfaces are spheres, and the local vertical gravity is parallel to the earth's radius. the modified (combined with the centrifugal force from the Earth's rotation) gravity acceleration g used in the model is $9.8\,m\,s^{-2}$.

- Thin-shell approximation

  Compared to the earth's radius ($> 6000 \times 10^3\,m$), the water depth of the ocean, with an average of $< 4000\,m$ and maximum of $< 11 \times 10^3\,m$, is much smaller. This allows us to replace the radial coordinate by a constant value, the radius of the Earth. Also by scale analysis, the vertical motion is much slower than the horizontal motion for the large scale ocean circulation. Thus the Coriolis and viscous terms are ignored in the vertical momentum primitive equation (section 2.1.1).

- Turbulent closure hypothesis

  According to *Reynolds* (1895), an instantaneous flow can be decomposed into its mean motion (time mean flow) and relative motion (turbulent flow). Applying the Reynolds averaging on the Navier-Stokes (NS) equations always involves extra unknown turbulent fluxes terms. To close the whole system, eliminating the unknown turbulent fluxes terms, a common solution is to parameterize the turbulent fluxes in terms of the mean flow (see details in section 2.1.3).

- Boussinesq approximation

  The density variations can be neglected except through their contribution to the buoyancy force (multiplied with the gravity acceleration g) in this approximation.

- Hydrostatic Approximation

  In the vertical, the vertical pressure gradient is balanced by the buoyancy (gravitational) force, thus excluding the convective processes and vertical acceleration from the initial NS equations.

- Incompressibility approximation

  If the fluid is incompressible, its density (ρ) is constant following a controlled volume along the flow. Thus,

$$\frac{D\,\rho}{D\,t} = 0$$

  Combined with the continuity equation,

$$\frac{\partial \rho}{\partial t} + \nabla \cdot (\rho \mathbf{U}) = 0$$

  thus, it results in a zero divergence velocity field,

$$\rho \nabla \cdot \mathbf{U} = 0$$

  or

$$\nabla \cdot \mathbf{U} = 0$$

  where $\mathbf{U}$ is the three-dimensional (3D) velocity.

2.1.1 Primitive equations

A curvilinear coordinate system with a horizontal plane ($\mathbf{i}$, $\mathbf{j}$) and local upward vector $\mathbf{k}$ (figure 2.2) is used in the model (more details in section 2.1.2). With the above six assumptions, the set of six primitive equations is given below,

$$\frac{\partial \mathbf{U}_h}{\partial t} = \left[(\nabla \times \mathbf{U}) \times \mathbf{U} + \frac{1}{2} \nabla \left(\mathbf{U}^2 \right) \right]_h - f \mathbf{k} \times \mathbf{U}_h - \frac{1}{\rho} \nabla_h p + \mathbf{D}^{\mathbf{U}} + \mathbf{F}^{\mathbf{U}} \tag{2.1a}$$

$$\frac{\partial p}{\partial z} = -\rho\, g \tag{2.1b}$$

$$\nabla \cdot \mathbf{U} = 0 \tag{2.1c}$$

$$\frac{\partial T}{\partial t} = -\nabla \cdot (T\, \mathbf{U}) + D^T + F^T \tag{2.1d}$$

$$\frac{\partial S}{\partial t} = -\nabla \cdot (S\, \mathbf{U}) + D^S + F^S \tag{2.1e}$$

$$\rho = \rho\,(T,\, S,\, p) \tag{2.1f}$$

where the 3D velocity $\mathbf{U} = \mathbf{U}_h + w\,\mathbf{k}$, $\mathbf{U}_h$ is the horizontal velocity over the ($\mathbf{i}$, $\mathbf{j}$) plane, w is the vertical velocity, T is the potential temperature, S is the salinity, ρ is the in situ density, ρ_0 is a reference density, p is the pressure, g is the gravitational acceleration, and $f = 2\,\Omega\, sin(\varphi)$ is the Coriolis parameter

(Ω is the Earth's angular velocity and φ is the latitude). $\mathbf{D}^{\mathbf{U}}$, D^T, D^S are the parametrization of subgrid scale (SGS) physics for momentum, temperature and salinity, and $\mathbf{F}^{\mathbf{U}}$, F^T, F^S are the surface forcing terms.

In the model, the ocean is bounded by an air/ice-ocean interface on the top, complex lateral coastlines, and topography at the bottom (figure 2.1). The top and bottom interface of the ocean could be expressed as $z = \eta(i,j,k,t)$ and $z = -H(i,j)$ separately, where η is the height of the sea surface ($Z = 0$ is set to the mean sea surface) and H is the water depth.

At the bottom, heat and salt fluxes through the sea floor are so small (*Huang*, 1999) that these fluxes are set to zero in the model. For the momentum transfer, the velocity normal to the sea floor is assumed to be zero, that is, no flow crossing the solid boundaries. The kinematic boundary condition at the bottom is:

$$w|_{z=-H} = -\mathbf{U}_h \cdot \nabla H \tag{2.2}$$

At the atmosphere-ocean interface, the exchanges of heat, salt, freshwater and momentum are not negligible (more details are discussed in the surface boundary condition section). Considering the mass balance, the kinematic surface condition is given as:

$$w|_{z=\eta} = \frac{\partial \eta}{\partial t} + \mathbf{U}_h \cdot \nabla \eta|_{z=\eta} - (P - E + R + I) \tag{2.3}$$

where P is total precipitation, E is evaporation, R is runoff and I is ice melt flux. It includes all the dynamic effects that cause the free surface displacement. The prognostic equation of η can be obtained from vertical integration of the continuity equation (2.1c) applying the above bottom (2.2) and surface (2.3) kinematic conditions:

$$\frac{\partial \eta}{\partial t} = (P - E + R + I) - \nabla \cdot \left[(H + \eta)\, \overline{\mathbf{U}}_h \right] \tag{2.4}$$

where the vertical averaged horizontal velocity $\overline{\mathbf{U}}_h = \frac{1}{H+\eta} \int_{-H}^{\eta} \mathbf{U}_h \, dz$.

In this study, we focus on the processes on relatively larger time scales (climate studies), so a time step of $O(1hour)$ is used. Thus fast external gravity

waves (EGWs) can be considered as high frequency "noise". To solve the numerical stability problem, a linear filtered free surface model (*Roullet and Madec*, 2000) is used in our configuration. An additional force is introduced in the momentum equation (2.1a) to dampen the fast EGWs:

$$\frac{\partial \mathbf{U}_h}{\partial t} \;=\; \mathbf{M} \;-\; g\,\nabla\left(\tilde{\rho}\eta\right) \;-\; g\,T_c\,\nabla\left(\tilde{\rho}\frac{\partial \eta}{\partial t}\right) \tag{2.5}$$

where T_c is a parameter characterizing the force in time (*Roullet and Madec*, 2000), $\tilde{\rho} \;=\; \rho/\rho_0$ is the dimensionless density, and $\mathbf{M}$ the collected contributions of the Coriolis, hydrostatic pressure gradient, non-linear and viscous terms in (2.1a).

Free-slip is used for the lateral boundary condition. No-slip boundary condition is supposed to be a proper boundary condition for the Navier-Stokes equations and widely used in the past ocean models, however, in real ocean models, the simulated momentum flux with "no-slip" parameterization is similar to that using the classic 'free-slip' boundary condition because the no-slip parameterization actually does not represent the molecular processes. More details can be found in a recently published paper by *Deremble et al.* (2011).

2.1.2 Curvilinear coordinate system and spatial discretization

For the ocean model, a set of orthogonal curvilinear coordinates are used for spatial discretization. Based on the sphere and thin layer assumptions, the local upward vector $\mathbf{k}$ is chosen as the z-axis, and the horizontal plane (x, y) is chosen with the unit vectors ($\mathbf{i}$, $\mathbf{j}$) orthogonal to $\mathbf{k}$. Here it is noted that the direction of the horizontal axis (x, y) can be arbitrary as long as they are orthogonal to each other. Although it is convenient to have the x-axis and y-axis aligned with lines of longitude and latitude, respectively, the convergence of the meridians in the standard geographical latitude-longitude grid leads to a spherical coordinate singularity close to the poles (e.g., *Eby and Holloway*, 1994; *Murray*, 1996; *Roberts et al.*, 2006). To avoid the above issue, a rotated

or re-projected grid is widely used in global or polar regional ocean models. In this study, a re-projected horizontal mesh is used following the tri-pole transformation proposed by *Murray* (1996) (see details in the next chapter).

In the model, different variables are placed on a staggered horizontal Arakawa C grid (*Mesinger and Arakawa*, 1976), with scalar points (T, S, p, ρ) in the centre and vector points (U, V, W) at the centre of cell faces (figure 2.3). Both the relative (ξ) and planetary vorticity (f) are defined in the centre of each vertical edge (F point in figure 2.3). In addition, the cell size is defined by two horizontal grid scale factors (e_1 and e_2) and a vertical scale factor (e_3) locally (figure 2.3, right). Thus the partial derivatives can be expressed in a uniform mesh with a grid size of unity (see details in Appendix). In NEMO, a centered second order finite difference approximation is applied.

For the vertical grid, the z-coordinate with partial steps (*Barnier et al.*, 2006), which represents the topography better than traditional z-coordinate (figure 2.4). With the vertical column divided into levels with fixed thickness everywhere, the traditional z-coordinate approach is straightforward and accurate in the pressure gradient calculation. But it poorly resolves the topography (figure 2.4, left), thus performs not well in bottom boundary layer simulation. However, the partial steps approach, which uses variable thicknesses for the bottom-most cells (figure 2.4, right), can much better represent the sea floor in the model while keeping the advantages of traditional z-coordinate. The thicknesses of the bottom-most cells are determined by input bathymetry data.

2.1.3 Subgrid scale physics

In ocean models, the resolution, both in space and time, is always insufficient to resolve turbulent motions, coming from the advective terms in the Navier-Stokes (NS) equations. However, these processes are important to larger scale oceanic dynamic and thermodynamic quantities. To present the SGS physics in models (to close the equations as well), a parameterization approach is generally applied to link them to resolved larger scale fields. The SGS terms

($\mathbf{D}^{\mathbf{U}}$, D^T, D^S) in primitive equations (2.1a, 2.1d and 2.1e) are divided into horizontal and vertical components separately shown as follows.

For the horizontal components, a Laplacian operator is used for tracer (both temperature and salinity) diffusion (z-coordinates),

$$D_l^T \;=\; \nabla \cdot \big(A_l^T \, \mathfrak{R} \, \nabla T \big) \quad \text{with } \mathfrak{R} \;=\; \begin{pmatrix} 1 & 0 & -r_1 \\ 0 & 1 & -r_2 \\ -r_1 & -r_2 & r_1^2 + r_2^2 \end{pmatrix} \tag{2.6}$$

where r_1 and r_2 represent the slopes between the surface along which the diffusive operator acts and the model vertical level. In the case of z-coordinate, the above slopes are all zeros, that is, $r_1 \;=\; r_2 \;= 0$. Equation 2.6 can then be simplified into the follow form:

$$D_l^T \;=\; \frac{1}{e_1 \, e_2} \left[\frac{\partial}{\partial i} \left(\frac{e_2}{e_1} A_l^T \, \frac{\partial T}{\partial i} |_z \right) |_z \;+\; \frac{\partial}{\partial j} \left(\frac{e_1}{e_2} A_l^T \, \frac{\partial T}{\partial j} |_z \right) |_z \right] \tag{2.7}$$

A Laplacian operator on a vector could be separated into the divergent and rotational parts of the flow (see details in appendix). The horizontal divergence is given by:

$$\chi \;=\; \nabla \cdot \mathbf{U}_h \;=\; \frac{1}{e_1 \, e_2} \left[\frac{\partial (e_2 \, u)}{\partial i} \;+\; \frac{\partial (e_1 \, v)}{\partial j} \right]$$

The rotational part (relative vorticity) is defined as:

$$\zeta \;=\; \nabla \times \mathbf{U} \cdot \mathbf{k} \;=\; \frac{1}{e_1 \, e_2} \left[\frac{\partial (e_2 \, v)}{\partial i} \;-\; \frac{\partial (e_1 \, u)}{\partial j} \right]$$

The second order diffusion is given as follows:

$$\begin{aligned} D_l^{\mathbf{U}} \;&=\; \Delta_h \, (\, A_l^m \, \mathbf{U} \,) \\ &=\; \nabla_h \, (\, A_l^m \, \chi \,) \;-\; \nabla_h \;\times\; (\, A_l^m \, \zeta \mathbf{k} \,) \\ &=\; \begin{pmatrix} \frac{1}{e_1} \, \frac{\partial \big(\, A_l^m \, \chi \, \big)}{\partial i} \;-\; \frac{1}{e_2 \, e_3} \, \frac{\partial \big(\, A_l^m \, e_3 \, \zeta \, \big)}{\partial j} \\ \frac{1}{e_2} \, \frac{\partial \big(\, A_l^m \, \chi \, \big)}{\partial j} \;+\; \frac{1}{e_1 \, e_3} \, \frac{\partial \big(\, A_l^m \, e_3 \, \zeta \, \big)}{\partial i} \end{pmatrix} \end{aligned} \tag{2.8}$$

In our configuration, for the momentum diffusion, instead of a second order operator, a fourth order (bilaplacian) operator is used. In practice, a fourth

order operator is done by applying twice the second order operator (equation 2.8).

The vertical turbulent fluxes are assumed to be linearly dependent on the gradients of large-scale quantities, which is a similar form to that of molecular diffusion and dissipation. In NEMO, the vertical momentum and tracer diffusion are expressed as follows:

$$\begin{aligned} \mathbf{D}_v^{\mathbf{U}} &= \frac{\partial}{\partial z}\left(A_v^m \frac{\partial \mathbf{U}_h}{\partial z} \right) \\ D_v^T &= \frac{\partial}{\partial z}\left(A_v^T \frac{\partial T}{\partial z} \right) \\ D_v^S &= \frac{\partial}{\partial z}\left(A_v^T \frac{\partial S}{\partial z} \right) \end{aligned} \tag{2.9}$$

where A_v^m and A_v^T are the vertical eddy viscosity and diffusivity coefficients, respectively.

The vertical eddy viscosity and diffusivity coefficients are updated using a 1.5 order turbulent closure model from the initial values. The turbulent closure model is based on a prognostic equation of turbulent kinetic energy ($\bar{e}$) defined as:

$$\begin{aligned} \bar{e} &= 0.5\,(\overline{u'^2} + \overline{v'^2} + \overline{w'^2}) \\ \frac{\partial \bar{e}}{\partial t} &= \frac{A_v^m}{e_3}\left((\frac{\partial u}{\partial k})^2 + (\frac{\partial v}{\partial k})^2 \right) - A_v^T\, N^2 + \frac{1}{e_3}\frac{\partial}{\partial k}(\frac{A_v^m}{e_3}\frac{\partial \bar{e}}{\partial k}) - c_\epsilon \frac{\bar{e}^{3/2}}{l_\epsilon} \\ A_v^m &= c_k\, l_k \sqrt{\bar{e}} \\ A_v^T &= \frac{A_v^m}{P_{rt}} \end{aligned} \tag{2.10}$$

where u', v' and w' are the velocity turbulent components, N is the local Brunt-Vaisälä frequency, $c_\epsilon = \sqrt{2}/2$ and $c_k = 0.1$ are two constants, P_{rt} is the Prandtl number (a function of local Richardson number, R_i), l_ϵ and l_k are the dissipation and mixing length scales, estimated as:

$$\begin{aligned} l_k &= l_\epsilon = \sqrt{2\bar{e}}\,/\,N \\ \frac{1}{e_3}|\frac{\partial l}{\partial k}| &\leq 1 \;\text{ with }\; l = l_k = l_\epsilon \end{aligned} \tag{2.11}$$

2.1.4 Time discretization

The time stepping in NEMO uses a three level scheme which can be illustrated as follows,

$$x^{t+\Delta t} \;=\; x^{t-\Delta t} \;+\; 2\,\Delta t\, RHS_x^{t-\Delta t,\,t,\,t+\Delta t} \tag{2.12}$$

where x is the prognostic variable (u, v, $T\,or\,S$), RHS stands for the Right-Hand-Side of the corresponding time evolution equation, Δt is the time step, and the superscripts indicate the time level at which the variable is evaluated.

For the non-diffusive parts (momentum and tracer advection, pressure gradient and Coriolis terms), the Leapfrog scheme (*Mesinger and Arakawa*, 1976), which has second-order accuracy, is used for the time stepping. However, the drawback of Leapfrog scheme is the differencing decouples odd and even grid points at any given time step (e.g., gray dots in figure 2.5). To prevent the possible divergence of odd and even time steps, a Robert-Asselin time filter (*Robert*, 1966; *Asselin*, 1972) is utilized, mixing the odd and even time steps:

$$x_F^t \;=\; x^t \;+\; \gamma\,\left[\,x_F^{t-\Delta t} \;-\, 2\,x^t \;+\; x^{t+\Delta t}\,\right]$$

where γ is the Asselin filter coefficient. In this study, γ is set to 0.1.

For the diffusive parts, Leapfrog scheme can not be used because all the coefficients of even derivative terms are zero. Instead, a forward or backward (implicit) time differencing scheme is used. The forward time discretization scheme,

$$x^{t+\Delta t} \;=\; x^{t-\Delta t} \;+\; 2\,\Delta t\, D_x^{t-\Delta t}$$

is used for the horizontal diffusion terms and tracer restoring terms. According to *Griffies* (2004), the following conditions must be met for numerical stability:

$$A_h \;<\; \begin{cases} \frac{e^2}{8\,\Delta t} & \text{laplacian diffusion} \\ \frac{e^4}{64\,\Delta t} & \text{bilaplacian diffusion} \end{cases} \tag{2.13}$$

In our study, the Laplacian and bilaplacian schemes are used for horizontal tracer and momentum diffusion, respectively. Thus given a time step

$\Delta t = 1800s$ and maximum horizontal grid size $e = 14450m$, it requires a maximum of $1.45 \times 10^4\, m^2\, s^{-1}$ for A_h^T and $3.78 \times 10^{11}\, m^4\, s^{-1}$ for A_h^m. For vertical diffusion, a backward (implicit) time differencing scheme, which is unconditionally stable, is used:

$$x^{t+\Delta t} = x^{t-\Delta t} + +2\,\Delta t\, RHS_x^{t+\Delta t}$$

2.2 Sea ice component

The sea ice model coupled to OPA in our study is the Louvain-la-Neuve sea Ice Model (LIM2) (*Fichefet and Maqueda*, 1997), which includes both dynamic and thermodynamics processes. It is based on a three-layer (one snow layer and two ice layers of equal thickness) model proposed by *Semtner Jr* (1976) with two ice thickness categories (mean thickness and open water). Ice internal stress is calculated based on an elastic-viscous-plastic rheology assumption (EVP, *Hunke and Dukowicz* (1997)).

2.2.1 Dynamics of sea ice

The sea ice is assumed to move in a two-dimensional plane with a momentum balance given by:

$$m\,\frac{\partial \mathbf{u}}{\partial t} = A\,(\tau_a + \tau_w) - m\,f\mathbf{k} \times \mathbf{u} - m\,g\,\nabla\eta + \nabla \cdot \sigma \tag{2.14}$$

where m is the mass of snow and ice per unit area, A is the ice concentration, τ_a and τ_w are the atmosphere-ice and water-ice interfacial stresses, f, g, η and $\mathbf{k}$ are the Coriolis parameter, the acceleration of gravity and sea surface elevation and vertical upwards unit vector respectively, and $\nabla\cdot\sigma$ is the internal stress term.

The air and water stress terms (τ_a and τ_w) are computed from the input

wind data and simulated ocean currents as follows,

$$\tau_a = \rho_a C_a |\mathbf{u}_a| \mathbf{u}_a \tag{2.15a}$$

$$\tau_w = \rho_w C_w |\mathbf{u}_o - \mathbf{u}_i| (\mathbf{u}_o - \mathbf{u}_i) \tag{2.15b}$$

where ρ_a is the air density, C_a is the air drag coefficient, $\mathbf{u}_a$ is the surface wind velocity (typically at $10\,m$ height), ρ_w is the seawater density, C_w is the ocean drag coefficient, $\mathbf{u}_w$ is the surface layer ocean velocity and $\mathbf{u}_i$ is the ice velocity. The air drag coefficient is obtained from the CORE bulk formula (*Large and Yeager*, 2004).

The force due to sea ice internal stress is given by the divergence of the stress tensor σ, which is calculated in the EVP approach as:

$$\sigma_1 = \sigma_{11} + \sigma_{22} \tag{2.16a}$$

$$\sigma_2 = \sigma_{11} - \sigma_{22} \tag{2.16b}$$

$$D_D = \frac{1}{e_1\, e_2} \left(\frac{\partial (e_2\, u)}{\partial i} + \frac{\partial (e_1\, v)}{\partial j} \right) \tag{2.16c}$$

$$D_T = \frac{1}{e_1\, e_2} \left(e_2^2 \frac{\partial (u/e_2)}{\partial i} - e_1^2 \frac{\partial (v/e_1)}{\partial j} \right) \tag{2.16d}$$

$$D_S = \frac{1}{e_1\, e_2} \left(e_1^2 \frac{\partial (u/e_1)}{\partial j} + e_2^2 \frac{\partial (v/e_2)}{\partial i} \right) \tag{2.16e}$$

where D_D is the divergence, D_T and D_S are the horizontal tension and shearing strain rates, and in the EVP rheology of *Hunke and Dukowicz* (1997),

$$2\, T_e \frac{\partial \sigma_1}{\partial t} + \sigma_1 = \left(\frac{D_D}{\Delta} - 1 \right) P \tag{2.17a}$$

$$\frac{2\, T_e}{e^2} \frac{\partial \sigma_2}{\partial t} + \sigma_2 = \frac{D_T}{e^2\, \Delta} P \tag{2.17b}$$

$$\frac{2\, T_e}{e^2} \frac{\partial \sigma_{12}}{\partial t} + \sigma_{12} = \frac{D_S}{2\, e^2\, \Delta} P \tag{2.17c}$$

where T_e is an elastic time scale (needing to be small enough to damp the elastic waves), e is the eccentricity of the ice elliptical curve (which describes the relation of the two principal components of a two dimensional stress tensor), and $\Delta = \sqrt{D_D^2 + \frac{1}{e^2}(D_T^2 + D_S^2)}$ is the deformation rate. P is the ice compressive strength given by a function of mean ice thickness (h) and concentration

(A),

$$P \;=\; P^{*}\, h\, e^{-\,C_{reh}\,(1\,-\,A)} \tag{2.18}$$

where P^{*} and C_{reh} are two empirical constants.

Compared to the viscous-plastic (VP) rheology (*Hibler*, 1979), in each equation (2.17), a time dependent artificial elastic term is added, which introduces a split time step to the ice model, updating the ice stress on a short time step and resolving the elastic wave velocity. EVP is used as the equations have more numerical computation advantages, such as allowing a fully explicit discretization (*Hunke and Dukowicz*, 1997).

2.2.2 Thermodynamics of sea ice

Ice thermodynamics are the processes related to the energy passing through or stored in the ice layer, which are associated with the vertical and lateral evolution (growth and decay) of sea ice. This section follows closely the model description section of *Fichefet and Maqueda* (1997).

To calculate the conductive heat flux (Q_c) in the vertical (z), a one dimensional heat diffusion equation is used to describe the heat conduction and storage in a snow-ice system (*Fichefet and Maqueda*, 1997):

$$\rho\, c_p\, \frac{\partial T}{\partial t} \;=\; G\, k\, \frac{\partial^2 T}{\partial z^2} \tag{2.19}$$

where ρ, c_p and k are the snow/ice density, specific heat and thermal conductivity, T is the temperature, t is the time, G is a correction factor used to convert the heat conduction change to the corresponding ice thickness variations. Details are provided in *Fichefet and Maqueda* (1997).

The snow-ice surface heat flux balance (B_{si}, which is a function of surface temperature T_{su}) includes five components, shortwave solar radiation (Q_{sw}), longwave radiation (Q_{lw}), sensible heat (Q_h), latent heat (Q_{le}) and conductive heat (Q_c) from below the surface.

$$B_{si} \;=\; Q_{sw} \;+\; Q_{lw} \;+\; Q_h \;+\; Q_{le} \;+\; Q_c \tag{2.20}$$

The first four terms are computed from bulk formula given by *Large and Yeager* (2004) as follows:

$$Q_{sw} = (1 - i_0)(1 - \alpha)\, Q_{ds} \tag{2.21a}$$

$$Q_{lw} = \epsilon\,(Q_{dl} - \sigma\, SST^4) \tag{2.21b}$$

$$Q_h = \rho_a\, c_p\, C_h\, (T_a - SST)\, |\mathbf{u}_a - \mathbf{u}_o| \tag{2.21c}$$

$$Q_{le} = \rho_a\, L_e\, C_e\, (q - q_s)\, |\mathbf{u}_a - \mathbf{u}_o| \tag{2.21d}$$

where Q_{ds} and Q_{dl} are the downwelling shortwave and longwave flux from the atmosphere, T_a and q are the near surface ($10\,m$) atmosphere temperature and specific humidity, q_s is the saturated specific humidity (a function of sea surface temperature SST) at the ocean surface, i_0 is the fraction of net shortwave radiation that penetrates the snow/ice; α is the ocean albedo, ϵ is the emissivity; σ is the Stefan-Boltzmann constant, L_e is the latent heat of vaporization of water, C_h, C_e are the transfer coefficients of sensible heat and latent heat, respectively. If the surface temperature T_{sf} is greater than the melting point, the excess of energy will be used for snow or ice melting:

$$\left(\frac{\partial h_*}{\partial t}\right)_{surface} = \frac{B_{si}}{L_*} \tag{2.22}$$

where L is the volumetric latent heat of fusion, subscript $*$ represents the snow (s) if it exists, otherwise it represents the ice (i).

At the ice-ocean interface, such as the bottom of an ice slab, any imbalance in energy (B_{io}) between the conductive heat flux ($Q_{c,\,bot}$) and heat flux from the ocean (B_{io}) is used for ice formation or melting:

$$\left(\frac{\partial h_i}{\partial t}\right)_{oi} = \frac{Q_{c,\,bot} - Q_{oi}}{L_i} \tag{2.23}$$

The lateral growth and decay of the ice is mainly associated with another important ice property, concentration (A), which is the fraction of a grid cell covered by ice. Its evolution is related to the heat flux budget from the open water (B_l):

$$\frac{\partial A}{\partial t} = (1 - A^2)^{1/2}\, \frac{(1 - A) B_l}{L_i\, h_0} \tag{2.24}$$

where the h_0 is the thickness of ice formed in a lead. When $B_l > 0$, all the heat gained in a lead is used for melting from below through Q_{oi} in equation (2.23).

2.2.3 Ice-ocean coupling

The existence of ice affects the heat, salt and momentum fluxes into the upper ocean. For example, with ice cover, the shortwave radiation fluxes acting on the ocean surface (Q_{swoc}) becomes:

$$Q_{swoc} = A\,Q_{str} + (1 - A)(1 - \alpha_w)\,Q_{ds} \tag{2.25a}$$

$$Q_{str} = i_0(1-\alpha)\,Q_{ds}\,e^{-1.5(h_i - 0.1)} \tag{2.25b}$$

where α_w is the open water albedo, and Q_{str} is the shortwave radiation reaching the bottom of an ice slab.

The upper layer of the ocean is a well mixed layer called the mixed layer (ML), within which vertical homogeneous temperature (T_m) and salinity (S_m) are assumed. If ice exists, to keep thermodynamic equilibrium, the temperature of the ML is set to the freezing point (T_{fw}, a function of ML salinity). Thus the net heat gain of the ML must be balanced by the sensible heat flux from the ocean to ice (Q_{oi}):

$$Q_{oi} = (1 - i_w|_{z=-h_m})Q_{str} + \Gamma\left[\frac{(1-A)B_l}{A}\right] + Q_{ent} + Q_{dif} + Q_{ovT}|_{-h_m} + Q_{fus} \tag{2.26}$$

where h_m is the mixed layer depth, i_w is the fraction of net shortwave radiation penetrating the ocean (a function of z), Γ is the Heaviside unit function, the last four terms on the right side are the heat fluxes due to entrainment, diffusion, overturning and changes in salinity, which are handled by the ocean mixed layer model.

The heat flux budget of the leads, B_l, is expressed as:

$$\begin{aligned} B_l \;=\; & (1 \,-\, i_w|_{-h_m})(1 \,-\, \alpha_w) Q_{sw} \\ & + \epsilon_w (Q_{lw} \,-\, \sigma\, T_m^4) \\ & + Q_h \,+\, Q_{le} \,+\, Q_{lsi} \,-\, Q_{lpr} \\ & + Q_{ent} \,+\, Q_{dif} \,+\, Q_{ovT}|_{-h_m} \,+\, Q_{fus} \end{aligned} \tag{2.27}$$

where ϵ_w is the ocean water emissivity, Q_{lsi} and Q_{lpr} are the latent heat released during snow/ice formation and snow falling onto the ocean, respectively.

In addition to heat fluxes, the snow/ice also contributes to the surface salt flux into the mixed layer:

$$\begin{aligned} Q_{salt} \;=\; & \underbrace{S_m \frac{\partial m_s}{\partial t}}_{snow\ melt} + \underbrace{(S_m \,-\, S_i)(\frac{\partial m_i}{\partial t})}_{ice\ melt} \\ & + \underbrace{(S_m \,-\, S_i)(\frac{\partial m_s}{\partial t} \,+\, \frac{\partial m_i}{\partial t})}_{salt\ rejection} + \quad \underbrace{S_i \frac{\partial m_s}{\partial t}}_{artificial\ meteoric\ ice} \\ & + \quad \underbrace{S_m (A\,E \,-\, P_w)}_{evaporation\,\&\,precipitation} \end{aligned} \tag{2.28}$$

where m_s is the snow mass per unit area, m_i and S_i are the mass and salinity of ice, respectively, E is the evaporation rate over the leads, and P_w is the freshwater change due to total precipitation.

2.3 Parameter list

Physical Constants

Symbol	Value	Description
r	$6.731 \times 10^6\, m$	Earth radius
g	$9.8\, m\, s^{-2}$	gravity acceleration
Ω	$7.2921151\, s^{-1}$	earth rotation parameter
ρ_0	$1024\, kg\, m^{-3}$	sea water density
ρ_{w0}	$1000\, kg\, m^{-3}$	pure water density
ρ_a	$1.22\, kg\, m^{-3}$	dry air density
c_p	$1000.5\, J\, kg^{-1}\, K^{-1}$	specific heat of air
c_{pw}	$4000.5\, J\, kg^{-1}\, K^{-1}$	specific heat of ocean water
σ	$5.67 \times 10^{-8}\, kg\, s^{-3}\, K^{-4}$	Stefan-Boltzmann constant
L_e	$2.5 \times 10^6\, J\, kg^{-1}$	latent heat of the vaporization of water
L_s	$2.839 \times 10^6\, J\, kg^{-1}$	latent heat of the sublimation of water
C_w	5×10^{-3}	sea water drag coefficient

Ocean Model		
Symbol	Value	Description
γ	0.1	Asselin time filter parameter
A_h^T	$300.0\, m^2\, s^{-1}$	horizontal tracer eddy viscosity
A_h^m	$-1.5 \times 10^{11}\, m^4\, s^{-1}$	horizontal momentum eddy diffusivity
A_v^m	$1 \times 10^{-4}\, m^2\, s^{-1}$	initial vertical eddy viscosity
A_v^T	$1 \times 10^{-5}\, m^2\, s^{-1}$	initial vertical eddy diffusivity
Sea Ice Model		
ρ_s	$330\, kg\, m^{-3}$	snow density
ρ_i	$900\, kg\, m^{-3}$	ice density
e	2	yield curve eccentricity
T_e	$600\, s$	elastic wave time scale
P^*	$2.3 \times 10^4\, N\, m^{-2}$	ice strength
C_{reh}	20	2st bulk-rheology parameter
C_{ice}	1.63×10^{-3}	transfer coefficient in ice
α	0.95	surface albedo
α_w	0.066	open water albedo
ϵ	0.97	emissivity of snow or ice
S_i	6.0	salinity of sea ice
k_i	$2.034396\, J\, s^{-1}\, m^{-1}\, K^{-1}$	conductivity of sea ice
k_s	$0.22\, J\, s^{-1}\, m^{-1}\, K^{-1}$	conductivity of snow

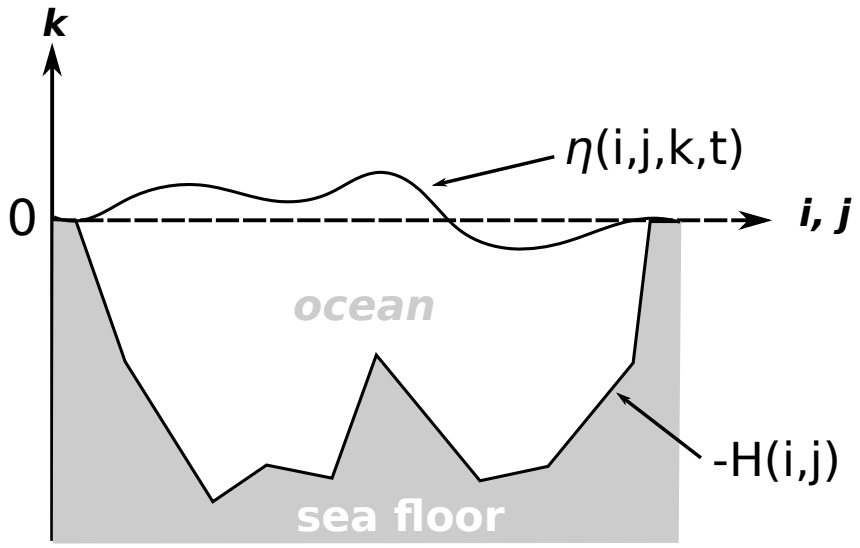

Figure 2.1: Illustration of surface and bottom boundaries

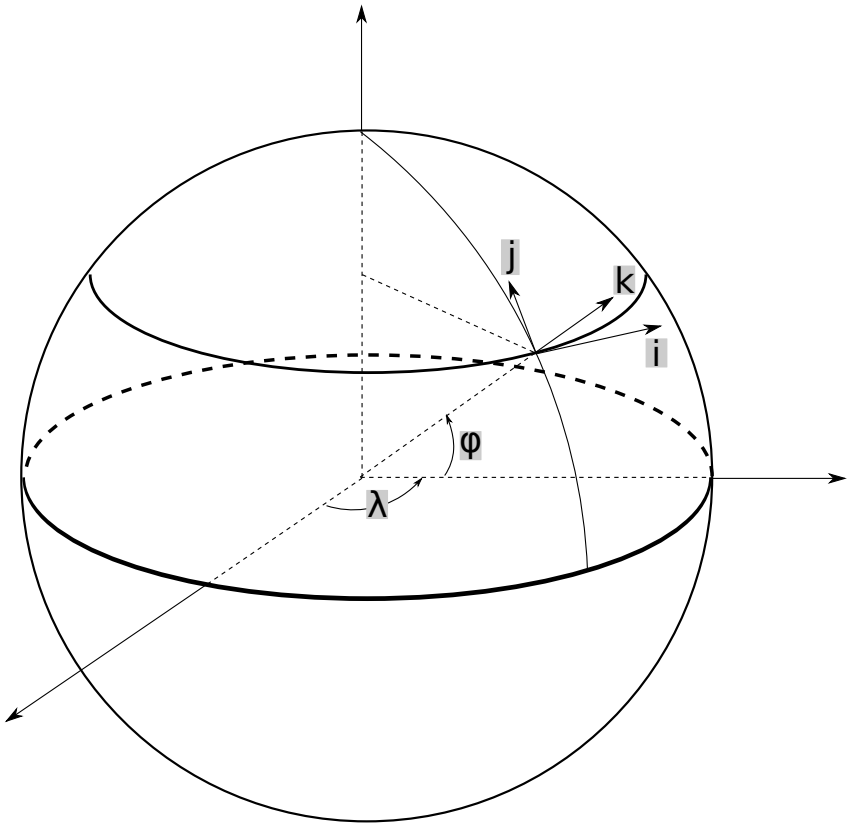

Figure 2.2: Spherical coordinate system

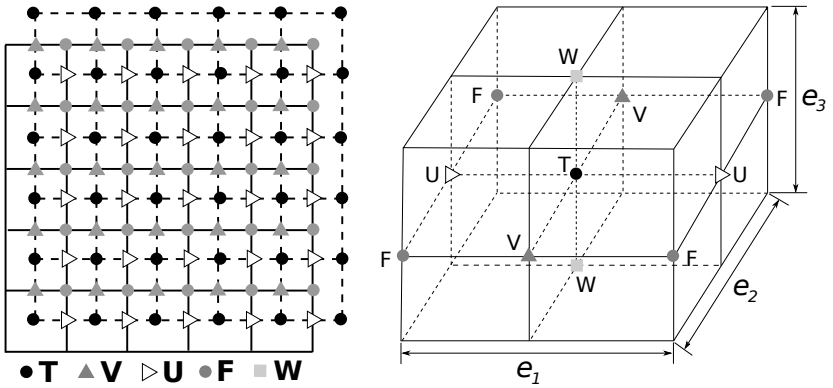

Figure 2.3: Top down (left) and 3D (right) views of the variable arrangement on a C-grid

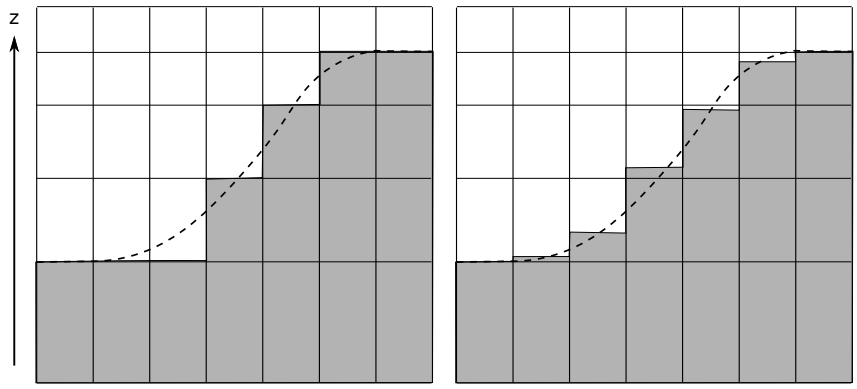

Figure 2.4: Vertical model grid in traditional z-coordinate with full steps (left) and z-coordinate with partial steps (right). Dash lines represent the real sea floor. Shaded cells show the responding sea floor in the model

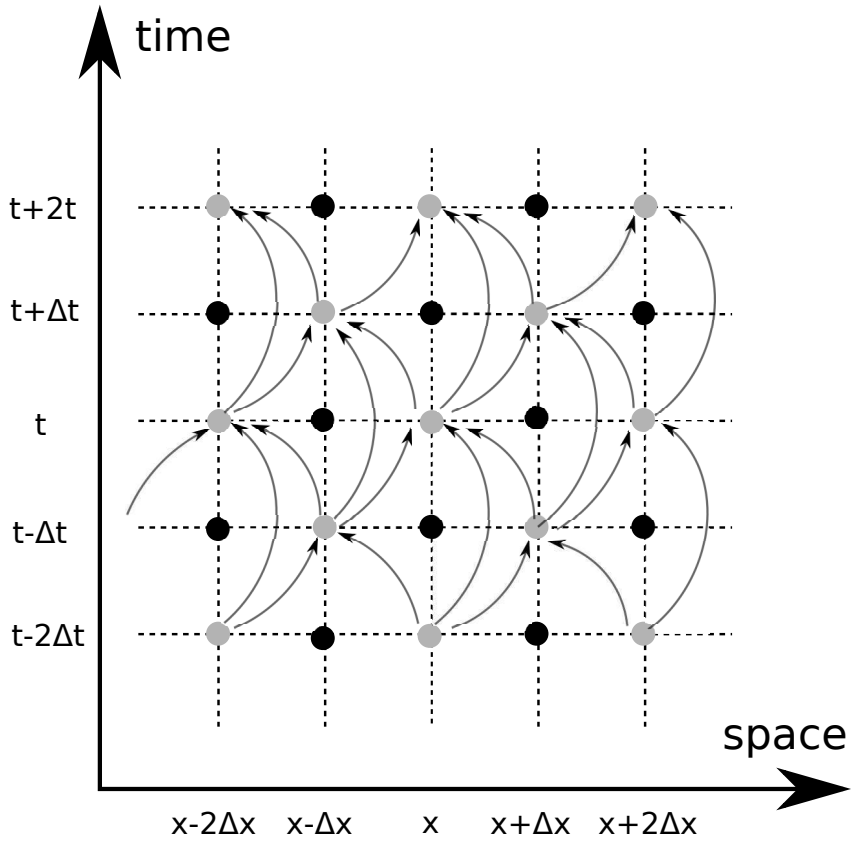

Figure 2.5: Temporal and spatial pattern of the time stepping in the Leapfrog scheme

Bibliography

Asselin, R. (1972), Frequency filter for time integrations, *Monthly Weather Review*, *100*(6), 487–490.

Barnier, B., et al. (2006), Impact of partial steps and momentum advection schemes in a global ocean circulation model at eddy-permitting resolution, *Ocean Dynamics*, *56*(5), 543–567, doi:10.1007/s10236.

Deremble, B., A. M. C. Hogg, P. Berloff, and W. K. Dewar (2011), On the application of no-slip lateral boundary conditions to 'coarsely' resolved ocean models, *Ocean Modelling*, *39*(3), 411–415.

Eby, M., and G. Holloway (1994), Grid transformation for incorporating the Arctic in a global ocean model, *Climate Dynamics*, *10*(4), 241–247.

Fichefet, T., and M. A. M. Maqueda (1997), Sensitivity of a global sea ice model to the treatment of ice thermodynamics and dynamics, *Journal of Geophysical Research*, *102*(C6), 12,609–12,646, doi:10.1029/97JC00480.

Griffies, S. M. (2004), *Fundamentals of ocean climate models*, vol. 518, Princeton University Press Princeton, USA.

Hibler, W. D. (1979), A dynamic thermodynamic sea ice model, *Journal of Physical Oceanography*, *9*, 815–846.

Huang, R. X. (1999), Mixing and energetics of the oceanic thermohaline circulation, *Journal of Physical Oceanography*, *29*(4), 727–746, doi:10.1175/1520.

Hunke, E. C., and J. K. Dukowicz (1997), An elastic-viscous-plastic model for sea ice dynamics, *Journal of Physical Oceanography*, *27*(9), 1849–1867.

Large, W. G., and S. G. Yeager (2004), Diurnal to decadal global forcing for ocean and sea-ice models: the datasets and flux climatologies. NCAR Technical Note TN–460+ STR, *National Center for Atmospheric Research*.

Madec, G., and the NEMO team (2008), *NEMO ocean engine*, Note du Pôle de modélisation, Institut Pierre-Simon Laplace (IPSL), France, No 27, ISSN No 1288-1619.

Madec, G., P. Delecluse, M. Imbard, and C. Lévy (1998), *OPA 8.1 ocean general circulation model reference manual*, Note du Pôle de modélisation, Institut Pierre-Simon Laplace (IPSL), France, No 11, 91pp.

Mesinger, F., and A. Arakawa (1976), Numerical methods used in atmospheric models, *GARP technical report 17, WMO/ICSU. Geneva, Switerzland*, *1*, 17.

Murray, R. J. (1996), Explicit generation of orthogonal grids for ocean models, *Journal of Computational Physics*, *126*(2), 251–273.

Reynolds, O. (1895), On the dynamical theory of incompressible viscous fluids and the determination of the criterion, *Philosophical Transactions of the Royal Society of London. A*, *186*, 123–164, doi:10.2307/90643.

Robert, A. J. (1966), The integration of a low order spectral form of the primitive meteorological equations (Spherical harmonics integration of low order spectral form of primitive meteorological equations), *Meteorological Society of Japan*, *44*, 237–245.

Roberts, J. L., P. Heil, R. J. Murray, D. S. Holloway, and N. L. Bindoff (2006), Pole relocation for an orthogonal grid: An analytic method, *Ocean Modelling*, *12*(1), 16–31.

Roullet, G., and G. Madec (2000), Salt conservation, free surface, and varying levels: A new formulation for ocean general circulation models, *Journal of Geophysical Research*, *105*(C10), 23,927–23,942, doi:10.1029/2000JC900089.

Semtner Jr, A. J. (1976), A model for the thermodynamic growth of sea ice in numerical investigations of climate, *Journal of Physical Oceanography*, *6*(3), 379–389.

Chapter 3

A Lagrangian View of Pacific Water Inflow Pathways in the Arctic Ocean during Model Spin-Up

[1]

[1]A version of this chapter has been accepted for publication. Hu, X. and Myers P.G. 2013, A Lagrangian View of Pacific Water Inflow Pathways in the Arctic Ocean during Model Spin-Up, Ocean Modelling

Abstract

In this study, we identify the routes of Pacific water within the Arctic Ocean using velocity fields, derived from the spin-up of a numerical model, and representing different circulation states within the basin. Lagrangian analysis shows there are two major routes of Pacific inflow water circulating in the Arctic Ocean, a Transpolar route and an Alaskan route. Those two routes transport more than 70% of the Pacific water, $\sim 50\%$ of which flows through the central Canadian Arctic Archipelago (CAA), to the Atlantic. The outer edge (close to the coast) of Pacific inflow water routes, especially within the interior basin, is close to the $7\,m$ isopleth of the upper (above $227\,m$) freshwater content. The proportion of Pacific water flowing along the two routes significantly changes with the spatial distribution of freshwater within the Canadian Basin. When more freshwater occupies the Beaufort Gyre (during the 5th year of spin-up), almost all the Pacific water entering the central CAA is from the Transpolar route. However, with a much weaker (flattened) Beaufort Gyre due to the loss of a significant amount of freshwater, $\sim 65\%$ of the Pacific water entering the central CAA is from the Alaskan route, resulting in younger Pacific water reaching the central CAA. Thus, we propose that not only the amount of freshwater but also its spatial distribution within the Canadian Basin play an important role in the Arctic Ocean circulation system, although the total volume transport ($\sim 0.35\,Sv$, $1\,Sv\,=\,10^6\,m^3\,s^{-1}$) of Pacific water through the central CAA shows little variation with time.

3.1 Introduction

Pacific water inflow through the Bering Strait provides the Arctic Ocean with large amounts of heat, freshwater and nutrients, playing an important role in Arctic oceanographic and ecological processes. Seasonal and inter-annual variability of this inflow may act as a possible trigger to the start of seasonal sea ice melting and explains much of the western arctic sea ice reduction in the past decade (*Woodgate et al.*, 2006, 2010; *Shimada et al.*, 2006). It feeds about one third of the total freshwater input ($8450\,km^3\,year^{-1}$) into the Arctic Ocean, directly affecting the structure of the halocline, especially within the Canadian Basin (*Bauch et al.*, 1995; *Woodgate and Aagaard*, 2005). In the highly productive western Arctic shelf, it is the primary source of nutrients during ice melting and the open-water period (*Coachman et al.*, 1975; *Grebmeier et al.*, 2006).

Pacific water enters the Arctic Ocean through Bering Strait forced by a meridional sea level gradient (*Coachman and Aagaard*, 1966; *Aagaard et al.*, 2006). The mean annual northward volume transport is about $0.8\,Sv$ ($1\,Sv = 10^6\,m^3\,s^{-1}$), with high seasonal and inter-annual variations (*Roach et al.*, 1995; *Woodgate and Aagaard*, 2005; *Woodgate et al.*, 2005a, 2006). The circulation of Pacific water within the Chukchi Sea is dominated by geostrophic balance with three major pathways (Herald Valley in the west, Barrow Canyon in the east and the Central Channel in the middle) (*Weingartner et al.*, 2005; *Woodgate et al.*, 2005b; *Pickart and Stossmeister*, 2008; *Panteleev et al.*, 2010; *Winsor and Chapman*, 2004; *Spall*, 2007). Pacific water will travel for five to nine months undergoing physical and biochemical modifications before reaching the Canadian Basin (*Panteleev et al.*, 2010). Using a regional eddy-resolving coupled sea ice-ocean model as well as satellite data, *Watanabe* (2011) investigated the Beaufort shelf break meso-scale eddies and the shelf-basin exchange of summer Pacific water, and concluded that both meso-scale eddies and wind-driven Ekman transport play roles in conveying Pacific water off the shelf.

The fraction and distribution of Pacific water within the Arctic Ocean have been extensively studied using chemical tracers and nutrients. Silicate (*Jones and Anderson*, 1986; *Bauch et al.*, 1995) and PO_4^* (*Broecker et al.*, 1998; *Ekwurzel et al.*, 2001) concentrations have been used to distinguish Pacific inflow water from other water masses in the Arctic Ocean, however, their concentrations could be significantly affected by biological processes, particular during the ice-free season. Thus, *Jones et al.* (1998) proposed that the ratio of nitrate versus phosphate (N:P) could be used to identify between waters of Pacific and Atlantic origin. Utilizing this N:P relationship, Pacific water was found to be the major source of freshwater in the Canadian Basin, particularly at depths ranging 50–200 m (*Jones et al.*, 2008; *Yamamoto-Kawai et al.*, 2008; *Carmack et al.*, 2008). Also the inter-annual variation of Pacific water influence in the central Arctic was revealed by observations (*Alkire et al.*, 2007, 2010). For the circulation, *Jones et al.* (1998) found the surface Pacific water might split into two branches near the Chukchi Plateau. One branch flows eastward along the northern Alaska coast, the CAA and Greenland, then exits through Fram Strait. The other branch, after mixing with Atlantic source water, enters the deep basin along the Mendeleyev Ridge, recirculating in the Canada and Makarov Basins, then exits these basins across the Lomonosov Ridge north of Greenland, and flows out of the Arctic Ocean through Fram Strait as well. Deeper Pacific water along the second route was also shown in later observations (*Jones et al.*, 2008). *Steele et al.* (2004) studied historic temperature and salinity profile data within the Arctic Ocean, and found similar pathways of summer Pacific water within the Arctic Ocean when the Arctic Oscillation (AO) index is high. But when the AO index is low, the Pacific inflow water might be all entrained into the Beaufort Gyre (*Steele et al.*, 2004). However, observations are still sparse in space and time, and systematically direct measurements of currents under the permanent sea ice are still not available yet. Thus it limits our understanding of the pathways of Pacific inflow.

Using a Lagrangian analysis, *Lique et al.* (2010) calculated the horizon-

tal mass stream function based on the monthly velocity fields from a coupled ocean sea ice global model averaged over 1980 to 2001. They obtained similar patterns to *Steele et al.* (2004), but had almost all the Pacific water exiting the Arctic Ocean through the CAA channels, while observations (*Jones et al.*, 2003) indicate that the Pacific water exported through Fram Strait could reach as far as $66^{\circ}N$. Thus, more work is needed to better understand the pathways of Pacific inflow water in the Arctic Ocean. Identifying the pathway of Pacific water within the Arctic Ocean will be helpful in knowing its fate and the associated impacts on the Arctic and subarctic system. In addition, the build-up and release of freshwater storage within the Arctic Ocean is dominated by large-scale atmospheric circulation variations (e.g., AO) (*Proshutinsky et al.*, 2002; *Häkkinen and Proshutinsky*, 2004; *Condron et al.*, 2009; *Jahn et al.*, 2010a). Whether and how the Pacific water pathways will be impacted are still an open question. Also, do the two main routes transport similar amounts of Pacific water? If not, which one contributes more and what are the mechanisms? How sensitive are the answers obtained from numerical models to technical issues of spin-up and freshwater content drift?

To investigate the pathways of Pacific water, as well as its variability associated with different freshwater distributions within the Arctic Ocean, we use a Lagrangian method to track Pacific water based on velocity fields produced during the spin-up of a numerical simulation. We will first provide the model configuration and forcing data in section 2, and then present the Pacific water inflow pathways based on velocity fields from year 5 in section 3. The variation of Pacific water inflow pathways and distribution of freshwater content within the Canadian Basin is investigated as well in this section. Summary and discussion are given in section 4.

3.2 Methods

3.2.1 Model description and configuration

In this study, we used a pan-Arctic regional configuration of the Nucleus for European Modelling of the Ocean (NEMO) numerical framework version 3.1 (*Madec and the NEMO team*, 2008). This coupled numerical model includes a three-dimensional (3D), linear free surface, hydrostatic, primitive-equation ocean generation circulation model and a dynamic-thermodynamic sea ice model, the Louvain-la-Neuve sea-ice model (LIM2) (*Fichefet and Maqueda*, 1997), with an elastic-viscous-plastic (EVP) ice rheology (*Hunke and Dukowicz*, 1997).

In the ocean module, the momentum equations are expressed in their invariant formulation (vorticity term + gradient of kinetic energy + vertical advection). An energy-entropy conserving scheme (*Arakawa and Hsu*, 1990), which conserves total energy and entropy only for horizontally non-divergent flow, is used to discretize the total vorticity term. The advection of tracer is formulated by the Total Variation Dissipation (TVD) scheme (*Lévy et al.*, 2001). Parameterizations for the subgrid-scale processes include i) a rotated Laplacian isopycnal scheme for lateral tracer diffusion with a maximum eddy diffusivity of $300.0\,m^2\,s^{-1}$ (proportional to the grid size); ii) a horizontal bilaplacian momentum diffusion with an maximum eddy viscosity of $-1.5 \times 10^{11}\,m^4\,s^{-1}$ (proportional to the cube of the grid size); iii) a one and half order turbulent kinetic energy (TKE) closure scheme for vertical mixing combined with an enhanced vertical diffusion. The vertical eddy viscosity and diffusivity are chosen to be $1.0 \times 10^{-4}\,m^2\,s^{-1}$ and $1.0 \times 10^{-5}\,m^2\,s^{-1}$, respectively, and are enhanced to $10\,m^2\,s^{-1}$ if the Brunt-Vaisala frequency (N^2) is less than $-1.0 \times 10^{-12}\,s^{-1}$

To avoid the coordinate singularity (convergence of the meridians) near the North Pole in the standard latitude-longitude spherical grid, an orthogonal transformation method proposed by *Murray* (1996) is adopted to generate the horizontal model grid. The model domain covers the northern Bering Sea, the

Arctic Ocean, the CAA, Nordic Seas and part of the North Atlantic Ocean (see figure 3.1, left) with a variable horizontal resolution of $\sim 11\,km$ in the central CAA and $\sim 15\,km$ in the Arctic Ocean. There are 46 levels in the vertical with layer thickness increasing smoothly from about $6\,m$ at the surface to around $240\,m$ at the bottom. The bathymetry data is derived from the global 1 min resolution relief dataset (ETOPO1, *Amante and Eakins*, 2009) provided by U.S. National Geophysical Data Center (NGDC). Hanning smoothing with a minimum depth of $6.25\,m$ is applied four times after the linear interpolation. Small islands, e.g., Diomede Islands at Bering Strait, are not resolved. Also narrow passages, such as Coronation Gulf and the adjacent waterways, are widened to have at least two tracer points, and Nares Strait is set to have at least three. Two open boundaries (Pacific and Atlantic) are used in our configuration (see figure 3.1, left).

3.2.2 Experiment setup

The atmospheric forcing data (10-m surface wind, 10-m air temperature and humidity, downward longwave and shortwave radiation, total precipitation and snowfall) come from the normal year data of the version 2 Coordinated Ocean-ice Reference Experiments dataset (CORE, *Large and Yeager*, 2004). The ocean starts from rest with initial 3D temperature and salinity fields from the Polar Science Center Hydrographic Climatology (PHC3.0, *Steele et al.*, 2001). Initial ice (concentration: 0.95, thickness: $3.0\,m$) and snow (thickness: $0.5\,m$) are prescribed where sea surface temperature is close to the freezing point. The lateral ocean components (normal and along boundary velocities, temperature and salinity) are interpolated onto our model grids from the monthly averages over the period 1979–2004 of a global ocean simulation, ORCA025-KAB001 (*Barnier et al.*, 2006). The inflows (outflows) at the Pacific and Atlantic open boundaries are adjusted linearly (proportional to the open boundary area) to keep the volume conserved. Temperature and salinity is restored within the buffer zone (shaded rectangles in figure 3.1, left) with a time scale of 40 days

decreasing from the inner edge of the buffers to one day at the boundary. No sea surface temperature or salinity restoring is active in our simulation except within the lateral boundary buffer zone. Zero wind stress is applied within the buffer zones close to the Pacific and Atlantic open boundaries. Monthly river runoff data is obtained from a global model (ORCA05 MGP).

The simulation starts from September 1st, to avoid the sea ice open boundary problem as much as possible, and then is integrated for 18 years. The monthly results from year 5 are used for the initial analysis in section 3, where those from year 10 and 15 are utilized to study the variations of Pacific inflow water pathways and the spatial distribution freshwater content within the Canadian Basin.

3.2.3 Trajectory calculation

To analyze the pathways of Pacific inflow water, we utilized a well-tested offline Lagrangian package ARIANE (*Blanke and Raynaud*, 1997; *Blanke et al.*, 1999). As discussed in *Lique et al.* (2010), many particles are input at geographical sections to represent water masses. The 3D velocities from the numerical model are used to integrate particle trajectories with time, to describe the large scale circulation of the given water mass. As each particle conserves its infinitesimal volume over the course of the integration, the mass transport between the initial section and another one downstream can be determined. The salinity, temperature and density of each particle evolves based on the Eulerian fields simulated by the model. Processes such as diffusion, convective mixing or dilution caused by surface input (i.e., runoff, precipitation and ice melting) are not considered in the Lagrangian tracking. But, as they are parameterized in the ocean model, the mean signature of those processes in ocean tracer and dynamic fields are present in the Eulerian fields (*Lique et al.*, 2010). Still, since they are not directly considered, this may impact the results of the particle tracking, especially for the denser parts of Pacific water formed by winter convection. As in *Lique et al.* (2010), we assume that the velocity

fluctuations within one month are smaller than the monthly mean. That is, the large scale Pacific water pathway can be represented by the month mean velocity fields. In practice, each particle is assigned an infinitesimal fraction of the initial volume flux, using a large enough particle number. Thus the directional transports (i.e., the water flow through certain straits) can be estimated.

The monthly averaged model output is linearly interpolated to a time step of 10 days in the trajectory calculation. To represent the Pacific water passing through the Bering Strait, we release 36679 particles in each month, evenly distributed along the Bering Strait section ($65°N55'$, $170°49'W$ – $65°46'N$,$167°23'W$, location is shown in figure 3.1, right), and the initial volume flux represented by each particle is computed from the simulated normal to section velocities and its cross section area.

3.3 Results

In this section, we will first show the simulated sea ice and ocean fields from year 5. Then given a reasonable comparison with the observations, the Lagrangian particle tracking will be used to describe the Pacific water routes on the basin-wide scale in the Chukchi Sea, the Arctic Ocean Basin, and the possible routes of the Pacific water entering the central CAA. The Pacific water pathways and Arctic Ocean freshwater content obtained from the simulation of year 5, 10 and 15, are compared to study the role of the Beaufort Gyre, as well as issues of model spin-up and freshwater drift.

3.3.1 Simulation in year 5

In our simulation, the atmospheric forcing fields are linearly interpolated onto each ocean model time step. The sea ice module is updated at each time step as well. The sea ice and upper layer of the ocean respond to the incoming surface and lateral forcing on a relatively shorter time scale than the deeper

layers.

3.3.1.1 Sea ice

Figure 3.2 (left) shows the ice concentration and thickness in winter (January, February, March) and summer (July, August, September). In winter, sea ice covers most of Arctic Ocean and adjacent seas with an ice concentration close to 1. In summer, sea ice retreats back to the Arctic Basin from both the Pacific and Atlantic sides, producing an almost ice-free southern Chukchi Sea (south of $70°N$), Baffin Bay and Southern Barents Sea. The total ice area within our model domain (buffer zones are not included) is estimated to be $\sim 12 \times 10^6\, km^2$ in winter and $\sim 7 \times 10^6\, km^2$ in summer. Our winter area estimate is low compared even to recent years as presented in *Comiso et al.* (2008), but given their estimate includes the entire northern hemisphere (including regions such as the Sea of Okhotsk which are not within our model domain), we do not think it is significantly off. Given the lack of ice in southern regions during summer, our summer estimate falls within the estimates for the 1980s and 1990s from *Comiso et al.* (2008).

Another important sea ice property, thickness, is shown in figure 3.2 (right). On average, ice thickness in summer is $\sim 0.55\, m$ thinner than that in winter over the Arctic Ocean. Spatial distribution is similar all the year round. The thickest ($> 4\, m$) sea ice occupies the west side of the CAA islands and the Lincoln Sea to the north of Greenland. The interior basin is generally covered by the sea ice with a thickness of $\sim 3\, m$. Sea ice in coastal seas (Chukchi Sea, Laptev Sea and Barents Sea) is $\sim 2\, m$ thick with significant seasonal variability. Those numbers and patterns are consistent with early submarine and satellite observations (e.g., *Bourke and Garrett*, 1987; *Kwok et al.*, 2009; *Kwok and Rothrock*, 2009).

3.3.1.2 Arctic Ocean basic tracer fields and circulation

The ocean underneath still maintains the essential features from the initial climatology fields. Figure 3.3 shows the freshwater content with a reference salinity of 34.8 over the upper $227\,m$ (if not otherwise specified, liquid freshwater is integrated in this layer) from the PHC salinity dataset (left) and the simulation from year 5 (right). According to *Condron et al.* (2009), the interpolation method can affect the initial freshwater storage. After interpolation, we get an initial liquid freshwater storage of $\sim 67100\,km^3$ ($> 98\%$ of that integrated in the whole water column) for the Arctic (enclosed by Bering Strait, west side of the CAA, Fram Strait and Barents Sea Opening), a similar region to that defined by *Serreze et al.* (2006). Although there is a $\sim 10\%$ loss (mostly occurring in the northwest of the Canadian Basin), the freshwater "dome" still occupies the Beaufort Gyre, with a total regional freshwater storage of $61220\,km^3$ for year 5. The solid freshwater on top was estimated to be $\sim 10000\,km^3$ by *Serreze et al.* (2006), however, a uniform ice thickness of $2\,m$ and a salinity of 4 were used in their calculation. Using our simulated ice area and thickness, the annual mean ice volume in year 5 is $\sim 20739\,km^3$, which is about double the above number but agrees with *Aagaard and Carmack* (1989) and *Condron et al.* (2009). Using an ice salinity of 6 and a density of $900\,kg\,m^{-3}$, the total freshwater storage in year 5 is $\sim 76700\,km^3$.

The annual mean oceanic fields at a section crossing the Arctic Basin from Bering Strait to Fram Strait are shown in figure 3.4. It clearly delineates the water masses in the Arctic Ocean. A well-mixed freezing cold and very fresh surface layer attributed to river runoff and sea ice meltwater lies on the top ($\sim$ 30–40 m). Then following the pronounced cold halocline with close to freezing temperature but salinity increasing rapidly with depth, the warm and salty water of Atlantic origin spreads over a depth range of 200 to $1000\,m$. Last the bottom water has decreasing temperature and increasing salinity with depth. The halocline in the Canada Basin is much thicker than that in the

Eurasian Basin. The double halocline with a "cold halostad" structure in the Canada Basin (*Shimada et al.*, 2005) is well reproduced. *Shimada et al.* (2005) attributed this complex structure to the injection of Pacific Winter Water, which is also partly shown in the subsurface layer circulation (figure 3.3, right) and our later trajectory analysis. The halocline in the Eurasian Basin is relatively simple, roughly a single "cold halocline" without an obviously warmer layer below the surface water. Two major deep waters, Canadian Basin Deep Water and Eurasian Basin Deep Water, are separated by the Lomonosov Ridge. The latter is relatively colder and fresher.

The subsurface circulation (figure 3.3, right) is also reasonably simulated when compared to previous studies (e.g., *Rudels*, 2001; *Aksenov et al.*, 2010). In the Arctic Ocean, the model features an anticyclonic circulation centered in the Beaufort Sea. A west branch flows northward, merged with flows from the Laptev Sea, to form the Transpolar Drift (TPD) that travels across the North Pole towards the north coast of Greenland. While part of the TPD exits through Fram Strait, another important portion of this flow turns west following the west side of the CAA islands producing a shelf current (see figure 4 in *Aksenov et al.* (2010) as well), which delivers Pacific water into the CAA region. The deeper layer circulation is not directly shown here, but, a general idea is seen in the normal to section velocity fields in figure 3.4 (right) and figure 3.5. This circulation is mainly dominated by the cyclonic boundary current, which is strongly topographically constrained, along the continental slope and basin edges. The Atlantic water enters the Arctic Ocean through Fram Strait, circulating anticlockwise along the rim of Eurasian Basin, and bifurcates into two branches in the vicinity of Lomonosov Ridge. One continues to flow cyclonically along the Canadian Basin slope with the other turning toward the pole. These two branches finally join together north of Greenland and exit through Fram Strait as the East Greenland Current.

3.3.1.3 Transports through the main straits

The exchanges between the Arctic Ocean and Pacific/Atlantic Ocean generally agree with the observations. The salinity, temperature and cross-section velocity fields at Bering Strait, Davis Strait, Fram Strait and Barents Sea Opening are presented in figure 3.5. The total oceanic volume and heat transport are summarized in table 3.1.

Bering Strait ($66°9'N$, $169°67'W$–$65°34'N$,$167°54'W$, section location is a little bit different from where the particles are released) is the only gateway through which the Pacific water enters the Arctic Ocean. In the model, a net northward flow of $0.93\,Sv$ is achieved, which is in the range of observations (table 3.1). The annual oceanic heat flux into the Chukchi Sea is $2.96\,TW$ ($1\,TW = 10^{12}\,W \simeq 0.315 \times 10^{20}\,J\,year^{-1}$) using a reference temperature of $0°C$, providing the sensible heat that impacts the melting (formation) of sea ice and thereby the transformation of Pacific water before entering the Arctic Basin. In early studies (e.g. *Coachman et al.*, 1975), it was noticed that there are large cross-sectional gradients of salinity and temperature with a higher temperature and fresher waters at the east side of the strait. However, high resolution mooring array data are still needed to provide the detailed structures. Our simulation does capture the basic temperature, salinity and velocity structure crossing the section from the limited available observations (*Coachman and Aagaard*, 1966; *Weingartner et al.*, 1999), but we note that the spatial resolution of the model is still not sufficient to resolve the relatively narrow Bering Strait, and thus all the components of Pacific inflow (e.g., fresh Alaska Coastal Current) passing through.

Davis Strait is the gateway of modified Arctic waters that pass through the CAA and Baffin Bay. Mooring data from *Cuny et al.* (2005) and *Curry et al.* (2011) show, on the east side, the fresh West Greenland Current flows northward on the shelf with the warm, salty West Greenland Slope Current going in the same direction on the slope. On the west side, cold fresh water

flows southward with a "bimodal" structure extending far offshore from Baffin Island. Four water masses were defined by *Curry et al.* (2011), the Arctic Water ($\theta \leq 1°C$; $S \leq 33.7$) above $300\,m$ in the western strait, West Greenland Irminger Water ($\theta > 2°C$; $S > 34.1$) along the West Greenland slope, West Greenland Slope Water ($\theta < 7°C$; $S < 34.1$), and Transitional water ($\theta \leq 2°C$; $S > 33.7$). The model successfully captures the above dynamic structures and water masses, although the net southward volume transport is smaller than observations (table 3.1). This is possibly caused by the widened Fury and Hecla Strait that branches off $\sim 30\%$ of the total transport through west Lancaster Sound and the lack of high frequency wind forcing in the Nares Strait region. The net freshwater flux is $69\,mSv$ ($1\,mSv = 10^3 m^3 s^{-1}$), which is comparable to the mooring results ($92 \pm 34\,mSv$ from *Cuny et al.* (2005) and $116 \pm 41\,mSv$ from *Curry et al.* (2011)), considering the smaller volume transport.

Fram Strait is one of two pathways for Atlantic inflow to the Arctic Ocean, as well as the major passage of Arctic Ocean outflow. The simulated tracer and velocity fields are consistent with the cross-section observations of *Schauer et al.* (2008) and *Beszczynska-Möller et al.* (2012). The Atlantic inflow is found in the West Spitsbergen Current at the eastern shelf edge spreading westward of the strait above $\sim 800m$ with a warm salty fast core ($\theta > 3°C$; $S > 34.95$; $U > 8\,cm\,s^{-1}$) located in depths of $\sim$ 150–300 m. This strong northward flow extends to the surface as the observations show (*Schauer et al.*, 2004; *Beszczynska-Möller et al.*, 2012) while temperature and salinity fields are cooled and diluted associated with too much sea ice melt in the model. The $0°C$ isotherm below the Atlantic layer is at $\sim 900, m$, close to the observed data (*Schauer et al.*, 2008; *Beszczynska-Möller et al.*, 2012). In central Fram Strait, especially below $50\,m$, the flow is very weak ($< 2\,cm\,s^{-1}$) and almost barotropic. The southward East Greenland Current, with cold and fresh Polar waters, is located just off the slope at the western side of the strait as in the observations (*Schauer et al.*, 2008; *Beszczynska-Möller et al.*, 2012).

Barents Sea Opening (BSO) is another gateway for Atlantic water flowing into the Arctic Ocean. Large amounts of heat are transported to the southern Barents Sea to keep it ice-free (*Smedsrud et al.*, 2010). The eastward flows include the Norwegian Coastal Current on the southern side and the Atlantic inflow in the center of the section. The Atlantic water has a typical temperature range of $4.5°C$–$6.5°C$ and a salinity above 35.0 (*Skagseth et al.*, 2008). The model failed to simulate the fresh ($S < 35.0$) coastal water, which is clearly shown by the observed data in August 1998 (*Skagseth et al.*, 2008). This explains why there is too much freshwater loss through the BSO in the model (table 3.2). The temperature field and the cold fresh Arctic water on the north side are reasonably simulated. Also the banded structure (mostly barotropic) velocity agrees well with the observations (*Skagseth et al.*, 2008).

3.3.2 Large-scale features of Pacific water inflow pathways

Using the method described in section 2.3 and monthly simulated velocity fields from year 5, the locations of particles released at Bering Strait are recorded every 10-days for 10 years following release. Such choices likely mean we significantly underrepresent the role of mixing in our analysis. The velocity fields from year 5 are used repeatedly during the 10 year integration.

To test the sensitivity of our following results to the temporal discontinuity between December 31 and January 1, six extra Lagrangian tracking experiments have been conducted by replacing the January velocity fields (U, V, W) with the December (EXP1) or February (EXP2) fields. With particles released in March, July and September, respectively, the proportion of Pacific water exported from the Arctic Ocean through either Fram Strait or the CAA channels (Lancaster Sound, Nares, and Jones Sound) within the ten years shows only small differences in our sensitivity experiments (table 3.3). Neither are there noticeable differences in the particle pathways (not shown). Thus, we

think the discontinuity between the beginning and end of year 5 velocity fields contributes little to the variation of the large scale circulation shown in our results.

The number of particles passing through Fram Strait or the CAA channels are counted for Pacific water volume calculations. On average, $\sim 75\%$ of Pacific water (in volume) is exported to the Atlantic through either the CAA channels or Fram Strait within 10 years (figure 3.6). Seasonal variability exists with a maximum of $\sim 84\%$ exported for particles released in July and a minimum of $\sim 56\%$ exported for particles released in October and November. Although particles were released in different months, the large-scale pattern of Pacific water pathway obtained from the locations of those particles at different integration times is generally similar (discussed in following paragraphs).

Our Lagrangian tracking shows it takes about one year for the Pacific water circulating in the Chukchi Sea to enter the deep basin (figure 3.7). The one year residence time of Pacific water in the Chukchi Sea is consistent with the model study done by *Nguyen et al.* (2011). The trajectories (figure 3.7) also clearly show the three major branches of Pacific water in the Chukchi Sea (Herald Canyon, Central Channel and Alaskan Coast) that were revealed by observations (*Weingartner et al.*, 2005) and model studies (e.g, *Watanabe and Hasumi*, 2009; *Lique et al.*, 2010; *Nguyen et al.*, 2011). Volume transports through the three pathways are $0.57\,Sv$, $0.12\,Sv$, $0.18\,Sv$, respectively, contributing 66%, 14%, 20% of the total Bering Strait inflow ($0.93\,Sv$). These fractions are close to the observations and high resolution model simulations summarized by *Nguyen et al.* (2011). A fourth pathway through Long Strait detected by *Lique et al.* (2010) and *Nguyen et al.* (2011) is found in our analysis as well but is not present all year round, with a small net transport of $0.06\,Sv$.

When the Pacific water reaches the Hope Sea Valley ($\sim 50\,m$ isobath) after leaving Bering Strait, it first bifurcates into two branches, with the Alaskan branch flowing northeast by Cape Lisburne and the other branch towards

the Siberian side. When the Alaskan branch reaches the northwest coast of Icy Cape, it divides into two small branches, one continuing along the Alaskan coast entering Barrow Canyon and the other branch flowing northward through the Central Channel. The western branch turns northwest first, entering the Hope Sea Valley, and then travels northward through the Herald Channel between Wrangel Island and Herald Shoal. In most months, especially during winter when the ocean circulation is less affected by the wind because of sea ice, part of the western branch of Pacific water can pass through Long Strait (figure 3.7, upper), But during the summer months (e.g., September, figure 3.7, lower), that flow is much decreased, which is possibly explained by more shelf-to-basin transport caused by the enhanced eddy activities when the sea ice margin retreats towards the basin interior (*Watanabe and Hasumi*, 2009). Part of the Herald Canyon outflow circulates clockwise around Herald Shoal, merged with the northward flow through the Central Channel and forming an anticyclonic circulation around Hanna Shoal. The west part of Herald Canyon outflow flows either to the west before reversing back to the east along the shelf or northward to the Chukchi Plateau.

Once the Pacific water enters the interior of the Arctic Ocean, it takes four to eight years within the interior before exiting to the Atlantic Ocean from either side of Greenland (figure 3.8). Figure 3.8 shows the locations of particles released in March (upper) and September (lower) over the ten-year integration. It shows that Pacific water exiting from the Arctic Ocean mainly travels along the Transpolar route, with only a very small portion going along the Alaskan route (figure 3.8, left). The main stream of the Transpolar route is bounded by Lomonosov Ridge, leaving only a small amount of Pacific water in the Amundsen Basin, which agrees with the observations (*Jones et al.*, 2008). Figure 3.8 (right) explains the fate of the $\sim 25\%$ of Pacific water that remains in the Arctic after 10 years. Most Pacific water advected west through Long Strait is trapped near the Siberia coast. Some Pacific water entering the deep basin is still traveling towards the Atlantic side or trapped within the Beaufort

Gyre, with consequently a much longer residence time.

3.3.3 Entry of Pacific water into the central CAA

Jones et al. (2003) revealed that the waters in the CAA channels are mainly of Pacific origin. Here we assume there is no Pacific water accumulated and lost due to ice formation involving Pacific water in the central CAA (thick black box in figure 3.9, right) and M'Clintock Channel. Thus all the particles entering the central CAA will eventually pass through east Lancaster Sound to Baffin Bay or via Fury and Hecla Strait into Foxe Basin. During the ten-year integration, between 30% to 40% of the total Pacific water reaches the central CAA (figure 3.9, top). For example, the largest monthly volume inflow of Pacific water (July), $\sim 1.6\,Sv$, can lead a flow of $\sim 0.54\,Sv$ ($\sim 34\%$) into the central CAA region. In this case (figure 3.9, top), almost all the Pacific water which enters the central CAA, comes from the Transpolar branch and enters the channels between the northern CAA islands. Still a significant portion of the Transpolar-branch Pacific water is able to flow westward along the northern coast of Queen Elizabeth Islands (QEI) until reaching M'Clure Strait, and turning eastward into the Parry Channel, merging with the Pacific water from the Alaskan branch. Pacific water entering the central CAA will pass Barrow Strait or Wellington Channel, exiting through east Lancaster Sound to Baffin Bay or Fury and Hecla Strait in the south to Foxe Basin.

If we take the average over each month, there is $\sim 0.34\,Sv$ of Pacific water entering the central CAA region, which accounts $\sim 44\%$ of the volume transport ($\sim 0.79\,Sv$) passing through the Lancaster Sound in the model. At the same time, $\sim 18\%$ ($\sim 0.17\,Sv$) and $\sim 4\%$ ($\sim 0.04\,Sv$) of the Pacific water passes through Nares Strait and Jones Sound, which thus accounts for $\sim 32\%$ and $\sim 38\%$ of the water volume flux through those two straits, respectively.

3.3.4 Variation of Pacific water pathways and freshwater content

The strong vertical stratification in the Arctic Ocean is determined by the vertical salinity difference (*Aagaard et al.*, 1981; *Sigman et al.*, 2004). Thus freshwater plays an important role in the Arctic Ocean dynamic and thermodynamic system. The inflow of Pacific water contributes about two thirds of the halocline (in thickness) within the Canadian Basin (*Steele et al.*, 2004). Here we examine the variation of Pacific water pathways and the spatial distribution of freshwater content in the Canadian Basin during model spin-up.

Table 3.2 shows the annual Arctic (defined in section 3.1.2) freshwater budget in the model from years 5, 10 and 15. There is a net freshwater loss from the Arctic Ocean in the model, resulting in an increase of salinity and a decrease in freshwater content. The isopleths of freshwater content are superimposed on figure 3.8 ($7\,m$) and figure 3.9 (right, $7\,m$, $9\,m$ and $12\,m$). Compared to the freshwater content in year 5 (figure 3.3, right), there is a marked change in spatial structure with time, particularly in the west Canadian Basin (figure 3.9, right). The thickness in the Beaufort Gyre is significantly reduced with time (figure 3.9, right). In year 5, there is a large amount of freshwater occupying the Beaufort Gyre region (figure 3.3 and figure 3.9, top). The center of simulated freshwater content is so close to the North American coast that it produces a strong freshwater-induced density gradient, preventing eastward flow along the coast and resulting in only little Pacific inflow traveling east near Alaska (figure 3.9, top, see details in next section). For the Pacific water exiting through the CAA or Fram Strait, the outer edge of its Transpolar route follows the $7\,m$ isopleth of upper layer freshwater content (figure 3.8). For those particles entering the central CAA, the Transpolar route can be roughly defined by the $9\,m$ isopleth of upper freshwater content (figure 3.9, top). In years 10 and 15, the freshwater pool has shrunk into the basin interior after a release of freshwater from the Canadian Basin. The location of Transpolar

route changes at the same time but still follows the given freshwater isopleths mentioned above. More significant change occurs along the Alaskan route, with much more Pacific water flowing along the Alaskan route in these later years (figure 3.9, center and bottom).

During the model spin-up, the location of the entry of the Pacific water into the central CAA also varies. In year 5, when the freshwater storage is high within the Canadian Basin, the Pacific water entering the Parry Channel is dominated by flows following the Transpolar route. However, in year 10 and 15, more of the Pacific water entering the Parry channel comes from the Alaskan route. For examine, in year 15, $\sim$ 25% ($0.22\,Sv$) of Pacific water, which accounts $\sim$ 65% of the total Pacific water entering this region, can travel along the Alaskan route and continue to the east along the northern coast of Prince Patrick Island while only $\sim$ 14% ($0.12\,Sv$) of the inflow is from the Transpolar route (and this component is confined to the channels of the QEI). Although the pathways change with time and the contributions of Pacific water to the central CAA water show large variations in some months (e.g., July), on average, the total amount of the Pacific water entering the central CAA does not significantly vary (year 5: 36% of $0.95\,Sv$; year 10: 37% of $0.94\,Sv$; year 15: 39% of $0.89\,Sv$) (figure 3.9, left).

In addition, as the Alaskan route is shorter, Pacific water using this route and passing through the central CAA will be much younger (figure 3.9, left). It takes six to eight years for Pacific water traveling along the Transpolar route to reach the central CAA while it takes only two to five years for those waters using the Alaskan route.

3.3.5 Dynamics behind the shift of Pacific water pathways

We can determine the geostrophic currents in the upper ocean (25–75 m) using the following equations,

$$fv = \frac{1}{\rho}\frac{\partial}{\partial x}\int_{z=D}^{z=0}\rho g dz + g\frac{\partial \zeta}{\partial x} \tag{3.1a}$$

$$fu = -\frac{1}{\rho}\frac{\partial}{\partial y}\int_{z=D}^{z=0}\rho g dz - g\frac{\partial \zeta}{\partial y} \tag{3.1b}$$

where u and v are the horizontal velocity component in x and y direction, respectively, f is the Coriolis parameter, g is the gravitational acceleration of the Earth, ρ is the density of seawater, ζ is the sea surface height (SSH), and D is the depth of the base of the layer over which the geostrophic currents are calculated. From this we see that the upper (25–75 m) ocean circulation in the Arctic Ocean, especially within the regions covered by permanent sea ice, is mainly geostrophic (figure 3.10). As given in equation 3.1, the calculation of geostrophic currents includes both the baroclinic component (due to the density anomalies) and "barotropic" component (due to SSH). The latter component is the dominant term in our calculation. Note that, the variability of SSH reflects not only the pure barotropic change (water mass), but also includes the baroclinic steric changes.

To examine the hydrographic changes within the Pacific water flows region with time, we consider two fixed sections (figure 3.11). The two sections are referred as Transpolar and Alaskan route in later text respectively. Note that we consider and examine several different approaches to determine these sections, including typical particle pathways in a given year, as well as given isopleths of freshwater content. In all cases, the main aspects of the results do not change. Therefore we use the representative fixed sections presented here to allow for a cleaner and more easily followed discussion. Given that these currents are mainly geostrophic, we look at the pressure gradient force (PGF, right hand side of equation 3.1) normal to each pathway, again over the same

25–75 m layer. Along the Transpolar route (figure 3.12, upper), the PGF is generally always positive, which, given our sign convention, is consistent with the Transpolar drift being a quasi-permanent geostrophic feature. Note that the reversal in sign of the PGF around year 10 and node 20 is related to the local circulation of other waters responding to a temporal shift in the Pacific water Transpolar route to the east at that time (i.e., is a function of our use of a representative section to simplify this analysis). The exact strength of the current and its location varies with time, consistent with the changes in the PGF over the 18 years of integration. A stronger PGF in the early part of the run compared to the later part is also consistent with more floats and thus Pacific water following the Transpolar pathway in the early part of the run compared to the later. The behavior is very different for the Alaskan route (figure 3.13, upper). Here, the PGF is negative and thus acts to oppose eastward flow through the first $\sim$ 10 years of integration. Afterwards, the PGF changes sign and thus acts to drive a strong eastward geostrophic flow in this region. These changes are consistent with very little Pacific water taking this route in the early part of the integration compared to a significant presence of Pacific water in year 15.

What causes these significant changes in the PGF along the Alaskan route and thus the geostrophic circulation? Since we have previously shown that the Pacific water routes are linked to given contours of freshwater water content, and given that except for the specific situation of a volume input of zero salinity (e.g., precipitation or the melt of multi-year ice), freshwater content is determined by salinity, we now examine how salinity changes impact the PGF. This is because there are clear indications that wind influences the circulation which in turn leads, with the right wind stress, to convergence and Ekman pumping, and thus an increase in freshwater content (e.g., *Proshutinsky et al.*, 2009; *McPhee et al.*, 2009; *Rabe et al.*, 2011; *Jahn et al.*, 2010b). We thus consider the different ways we compute the PGF. We compare using our "full" calculation of the PGF (the right-hand side of equation 3.1) to estimate the

changes between years 5 and 15 to a calculation based on the PGF computed from the dynamic height (DH) using the annual mean 3D temperature and salinity fields in year 5 as the reference fields. Thus the calculated DH in year 15 can be used to quantity the accumulated baroclinic effect on SSH from year 5 to year 15. Furthermore, as given in *Steele and Ermold* (2007), DH above a depth of D can be separated into two components, thermosteric dynamic height (DH_T) and halosteric dynamic height (DH_S):

$$DH = \int_{z=D}^{z=0} \left(\frac{\rho_{ref} - \rho_{T,S,P}}{\rho_{ref}} \right) dz \tag{3.2a}$$

$$DH_T = \int_{z=D}^{z=0} \left(\frac{\rho_{ref} - \rho_{T,S_{ref},P}}{\rho_{ref}} \right) dz \tag{3.2b}$$

$$DH_S = \int_{z=D}^{z=0} \left(\frac{\rho_{ref} - \rho_{T_{ref},S,P}}{\rho_{ref}} \right) dz \tag{3.2c}$$

where ρ is density, which is a function of temperature (T), salinity (S), and pressure (P), subscript ref stands for the reference field.

If we then integrate over the Pacific water layer (i.e., between the surface and the interface between the Atlantic and Pacific waters, $\sim 200m$ for the Transpolar route and $\sim 250m$ for the Alaskan route), the PGF derived from the DH_S can thus explain most of observed change in the PGF (figure 3.12, lower and figure 3.13, lower). Thus, the evolving salinity in the model both changes the freshwater content distribution and drives changes in the model's PGF and geostrophic circulation, impacting the routes of Pacific water in the Arctic Ocean.

3.4 Summary and discussion

In this paper, the pathways of Pacific water in the Arctic Ocean are studied using a Lagrangian approach. Velocity fields are produced using a coupled ocean-sea ice pan-Arctic regional model. Similar to previous studies (e.g. *Steele et al.*, 2004; *Lique et al.*, 2010; *Nguyen et al.*, 2011), our analysis clearly shows

that Pacific water transits the Arctic Ocean following two routes, a Transpolar route and an Alaskan route. Using the velocity fields from year 5, associated with a strong and deep Beaufort Gyre, we find that, within 10 years, more than 70% of Pacific water exits through Fram Strait or the central CAA region. Prior to exiting, the Pacific water spends about one year in Chukchi Sea, and then $\sim$ 4–8 years in the deep basin. It mainly follows the Transpolar route, whose outer edge is close to the $7\,m$-contour of freshwater content. The Alaskan route is more notable from simulations in year 10 and especially year 15. Along this shorter route, it only takes $\sim$ 2–5 years for the Pacific water to reach the central CAA. We find that the upper ocean currents associated with the main pathways of Pacific water are geostrophic. In our simulations, the PGF acts to drive a vigorous and strong Transpolar drift, although there are temporal variations, impacting the transport of Pacific water along this route. The sign of the PGF changes with time along the Alaskan route, from directed to the coast around year 5 (consistent with the presence of little Pacific water) and to the basin interior later in the integration, helping to transport Pacific water along this route around year 15. These changes in the PGF are driven by changes in the halosteric component of the dynamic height, and are thus set by the evolution of freshwater content in the Beaufort gyre (*McPhee et al.*, 2009).

The volume transport through Bering Strait (0.89 to $0.93\,Sv$) and the central CAA (Lancaster Sound, 0.74 to $0.78\,Sv$) is roughly equivalent, but our results show no more than 40% of the Pacific water can enter the central CAA within 10 years. We also did backward integration of particles released at Lancaster Sound (not shown), and obtained similar results. Thus, there must be some other sources of water to feed the central CAA. Possible sources are the Arctic Ocean surface waters, formed by summer melting sea ice, runoff from Russian coastal water (Kara, Laptev, Barents Sea) and the McKenzie River. The backward integration analysis also indicates that the Pacific water passing through Long Strait towards the Siberian coast will not reach the CAA

within 10 years. Additionally, we note that the Lagrangian tracking we use here does not consider mixing and entrainment.

Rabe et al. (2011) calculated the liquid freshwater content within the Arctic Ocean using observed summer salinity profile data and found a significant variation in the Beaufort Sea and southern Canadian Basin between the periods 2006–2008 and 1992–1999. We note our change in freshwater content between years 5 and 15 is of the opposite sign compared to *Rabe et al.* (2011). However, in terms of distribution and the difference in magnitude between the two periods, the freshwater content in the model is similar to the observations. Thus even if the cause of our freshwater content change is produced by a model drift due to the lack of sea surface salinity (SSS) restoring, the similarity of our structures with the observations suggests that the Pacific inflow water pathways may undergo a significant shift during this process. So to better understand the real physical processes in the Arctic Ocean using numerical models, even in the spin-up stage, not only the amount but also the spatial distribution of freshwater is essential.

3.5 Acknowledgements

This work has been supported by NSERC and Government of Canada International Polar Year awards to PGM. We are grateful to Westgrid and Compute Canada for computational resources. We thank C. Boening and A. Biastoch for providing us model output that was used for open boundary forcing. We thank B. Blanke and N. Grima for freely sharing the Lagrangian analysis package ARIANE (available from http://stockage.univ-brest.fr/ grima/Ariane/). We thank all four anonymous reviewers for their valuable and insightful comments and suggestions that helped to considerably improve the quality of this paper.

Table 3.1: Simulated and observational oceanic volume and heat transport through the Arctic Ocean lateral straits in year 5

	volume transport (Sv)		heat transport (TW)*	
	model	obs.	model	obs.
Bering Strait	0.93	0.6–1.0 [a]	2.96**	∼6-18[b]
Davis Strait	1.18	2.6 ± 1.0[c], 2.3 ± 0.7[d]	17.7	18 ± 17[c], 20 ± 9[d]
Fram Strait	1.8	2.0 ± 5.9[e]	29.7	26–50[e]
Barents Sea Opening	2.18	2.0[f]	50.7	73[f]

* volumetric heat capacity is $4 \times 10^6\, J\, K^{-1}\, m^{-3}$, relative to $0\,^{\circ}C$; $1\,TW = 10^{12}\,W$

** $\sim 10\,TW$ if a reference temperature of $-1.9\,^{\circ}C$ is used

a: *Woodgate et al.* (2005b); b: *Woodgate et al.* (2010) using a reference temperature of $-1.9\,^{\circ}C$; c: *Cuny et al.* (2005); d: *Curry et al.* (2011); e: *Schauer et al.* (2008); f: *Smedsrud et al.* (2010)

Table 3.2: Freshwater budget of the Arctic Ocean

	Fram Strait		Barents Sea Opening		Bering Strait		CAA		P-E	Runoff	NET
	Liquid	Ice	Liquid	Ice	Liquid	Ice	Liquid	Ice			
Y0005	1354	2689	818	564	-2115	-31	2898	285	-1693[a]	-2576	2193
Y0010	888	2367	798	564	-2074	-39	2397	241	-1649[a]	-2576	917
Y0015	936	2290	634	564	-1966	-25	2362	238	-1582[a]	-2576	875
Observation[b]	2660	2300	340[c]	0	-2500	0	3200	160	-2000	-3200	960

unit: $km^3\,year^{-1}$; reference salinity is 34.8.

a: salt flux at ocean surface without runoff.

b: averaged over the period of ∼1980-2000 from *Serreze et al.* (2006).

c: only $90\,km^3\,year^{-1}$ if freshwater from Norwegian Coastal Current is considered.

Table 3.3: Sensitivity of the percentage of Pacific water leaving the Arctic Ocean within 10-year integrations due to the presence of a temporal discontinuity in the year 5 velocity fields

Initial Time	Normal[a]	EXP1[b]	EXP2[c]
March	76.91%	76.38%	76.38%
July	83.74%	83.94%	83.27%
September	75.07%	78.45%	77.84%

a: the January velocity fields are taken directly from the simulated January fields; b: the January velocity fields are replaced with the December fields; c: the January velocity fields are replaced with the February fields

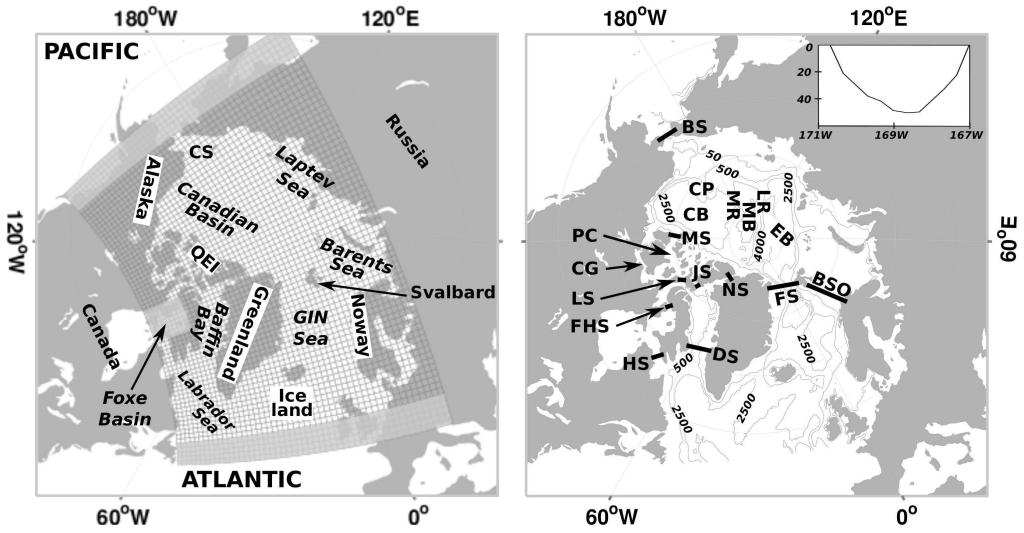

Figure 3.1: Model horizontal mesh (left, every eighth grid line plotted in each direction; shaded area: buffer zones) and isodepth contours (right, thin gray lines; subfigure at upper right corner shows the depth of Bering Strait). (CS: Chukchi Sea; QEI: Queen Elizabeth Islands; BS: Bering Strait; CP: Chukchi Plateau; CB: Canadian Basin; MR: Mendeleyev Ridge; MB: Markarov Basin; LR: Lomonosov Ridge; EB: Eurasian Basin; BSO: Barents Sea Opening; FS: Fram Strait; NS: Nares Strait; JS: Jones Sound; MS: M'Clure Strait; PC: Parry Channel; CG: Coronation Gulf; LS: Lancaster Sound; FHS: Fury and Hecla Strait; HS: Hudson Strait; DS: Davis Strait)

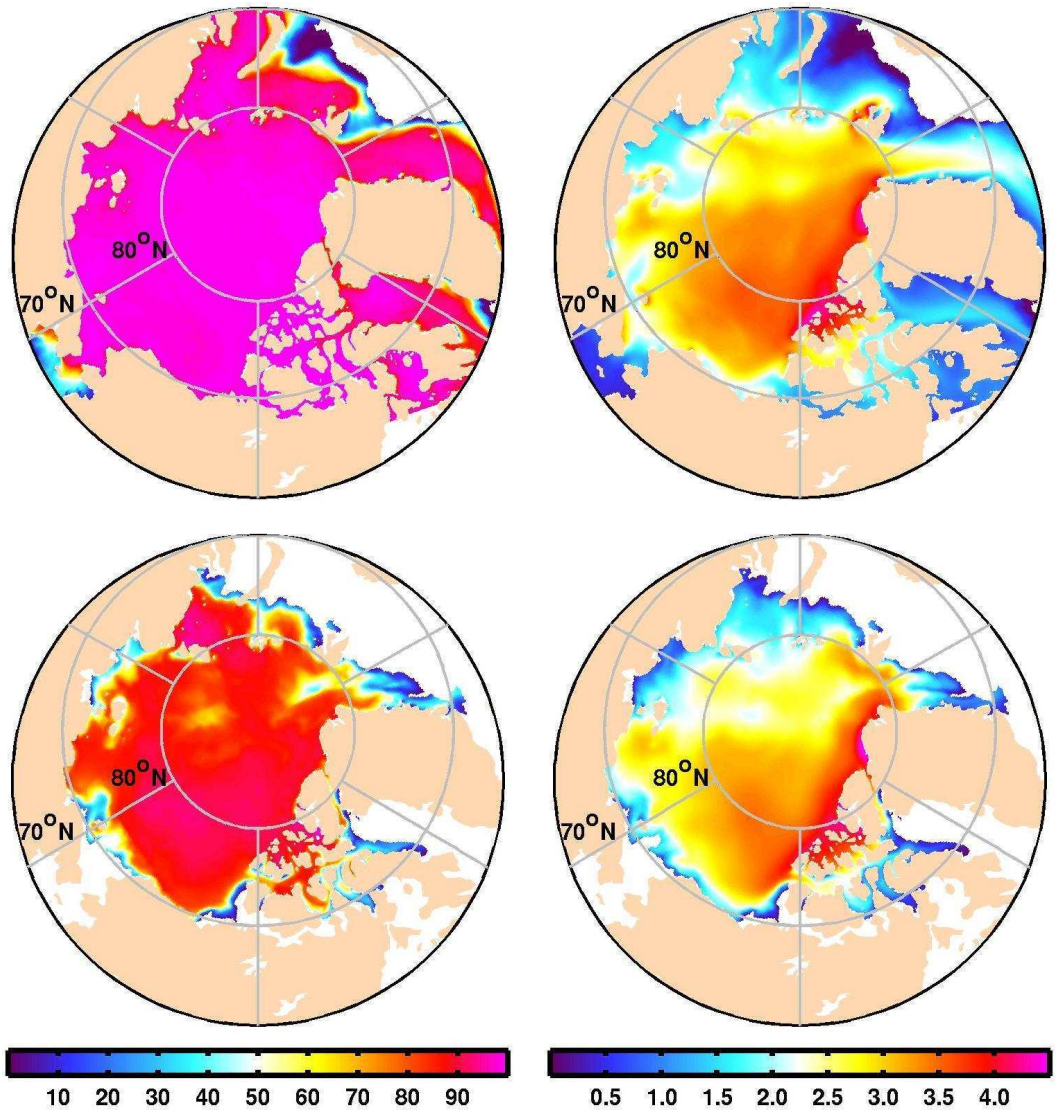

Figure 3.2: Winter (upper) and summer (lower) sea ice concentration (left, unit: percentage) and thickness (right, unit: meter) in year 5

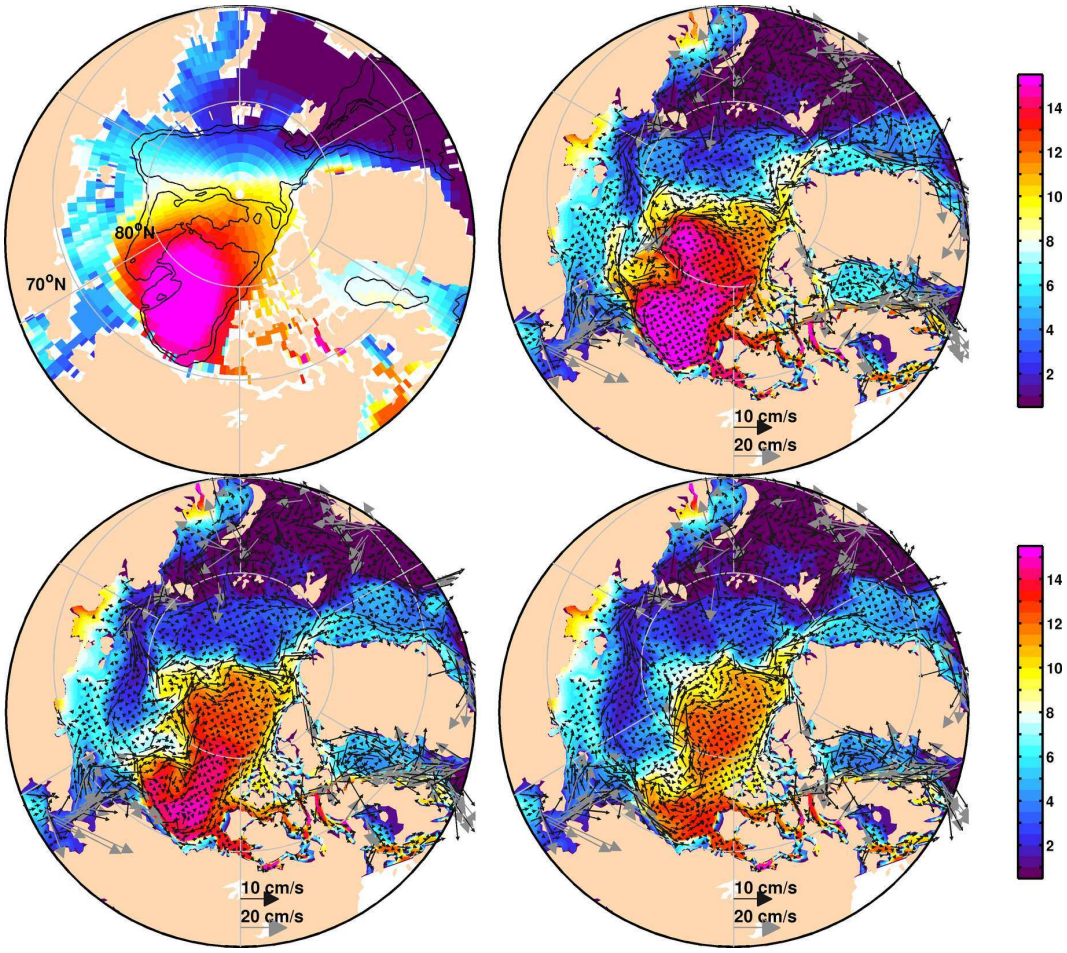

Figure 3.3: Upper freshwater content ($Sref = 34.8$, unit: meter) from PHC climatology (upper left , black lines: $1000\,m$ and $2500\,m$ isodepth contours) and simulation in year 5 (upper right), year 10 (lower left) and year 15 (lower right) with 25–$75\,m$ averaged velocity overlayed. Vectors are shown with $\leq 10\,cm\,s^{-1}$ (black arrows) and $> 10\,cm\,s^{-1}$ (gray arrows), and note the different length scales

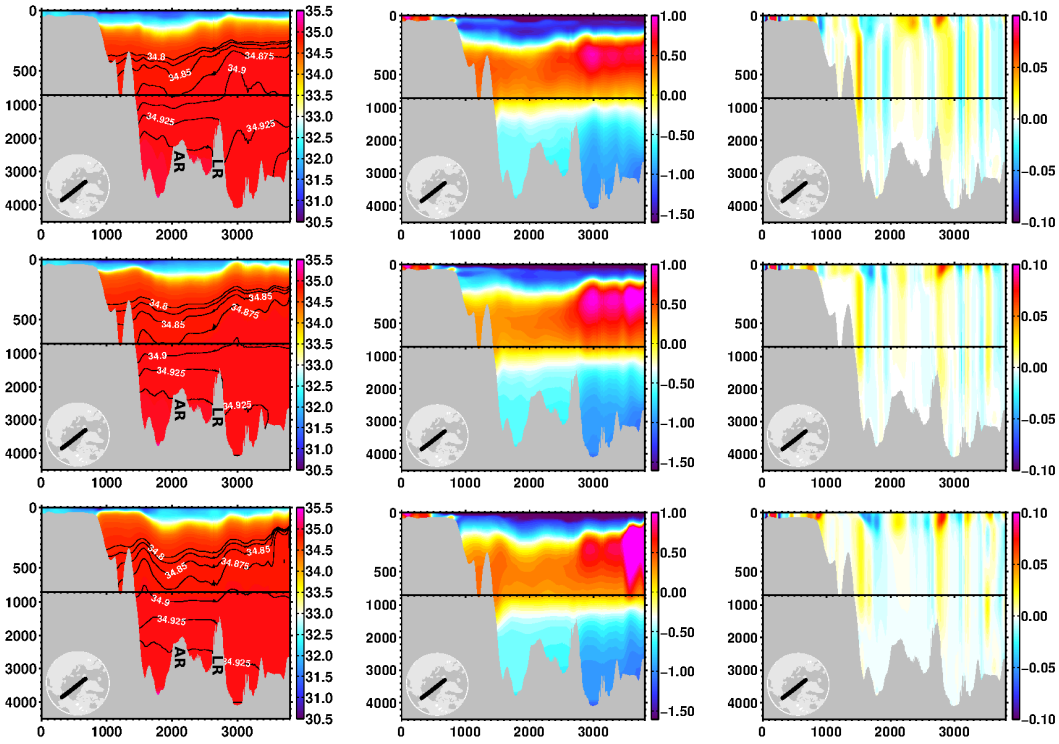

Figure 3.4: Simulated salinity (left, unit: PSU), temperature (middle, unit: $^{\circ}C$) and normal to section velocity (right, velocity is positive towards the CAA, unit: $m\,s^{-1}$) in year 5 (top), year 10 (center) and year 15 (bottom) for the section Bering-Fram (black line in the small map shows the section location; y-axis shows the water depth in meter; x-axis is the distance in km)

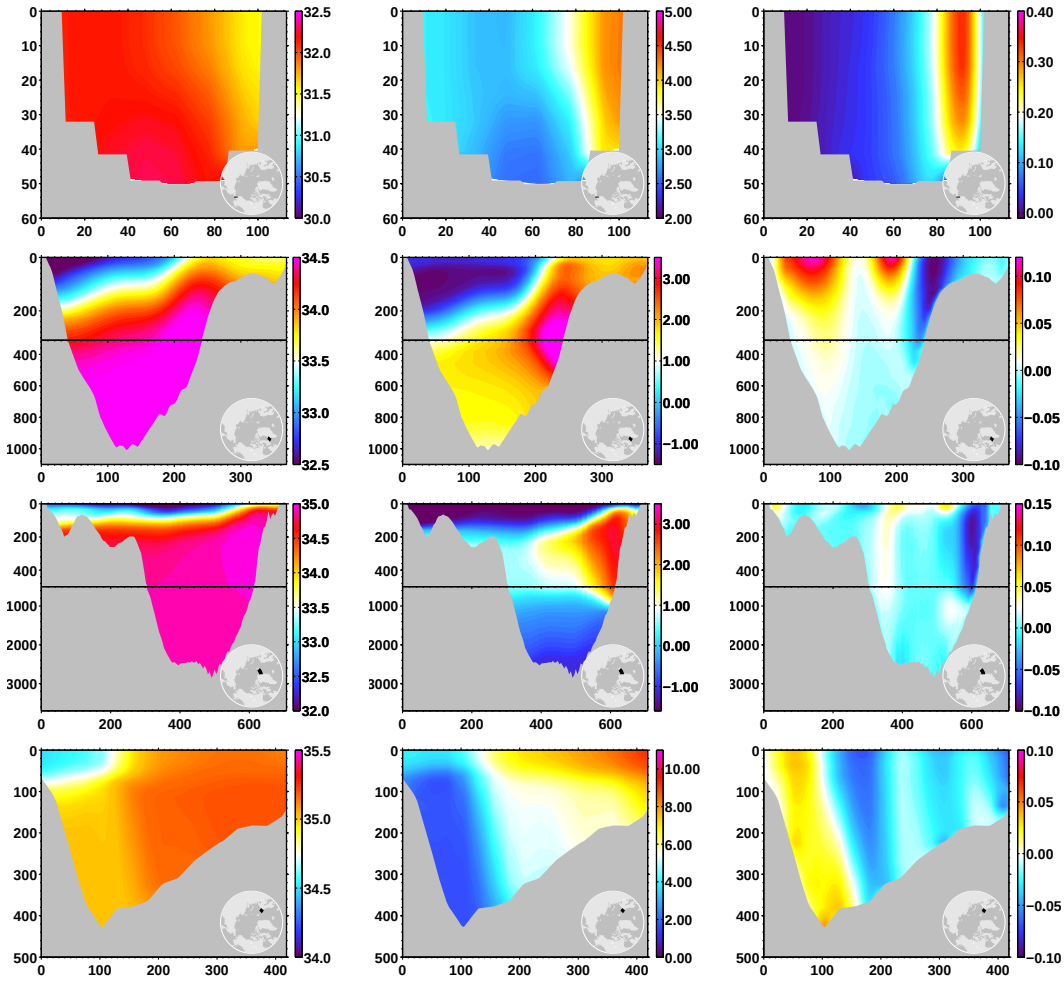

Figure 3.5: Similar to figure 3.4 but for Bering Strait, Davis Strait, Fram Strait and Barents Sea Opening (velocity is positive northward for Bering Strait and opposite for the rest). To be consistent with the observations in time, fields from October are plotted for Bering Strait, August for Barents Sea Opening and annual mean for the rest. Note that the range of the colorbar is different for each panel.

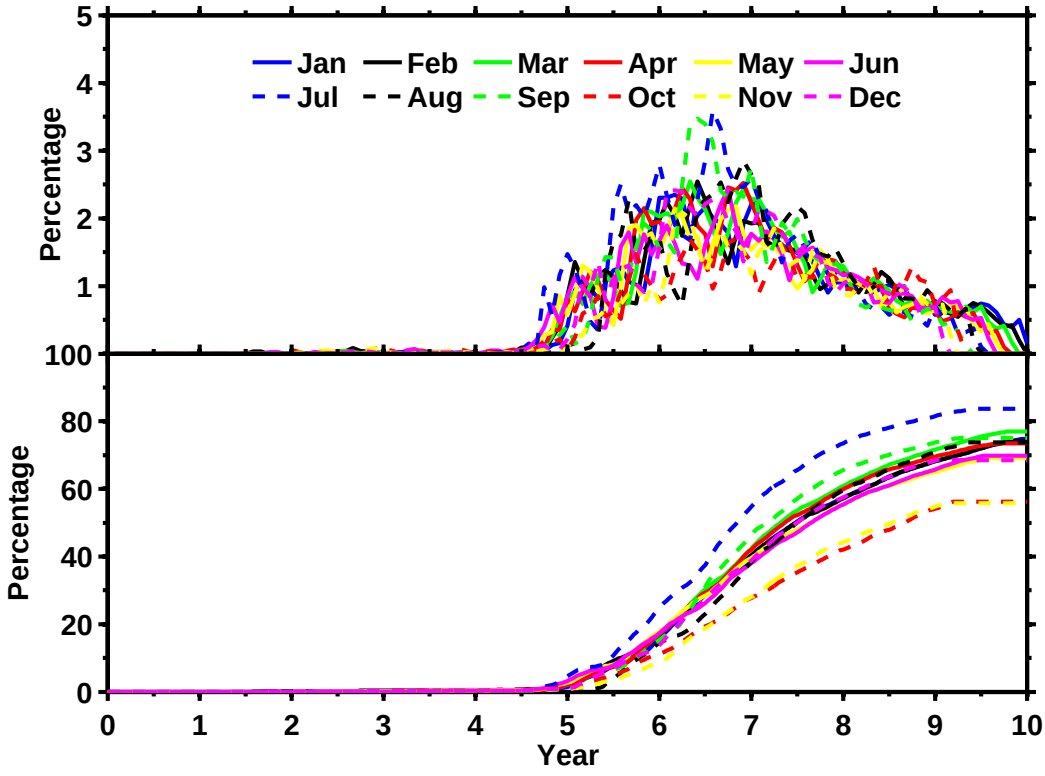

Figure 3.6: Percentage (upper) and accumulated percentage (lower) of Pacific water parcels exiting from either Fram Strait or the CAA channels at different integral time (colors and line styles represent the initial months)

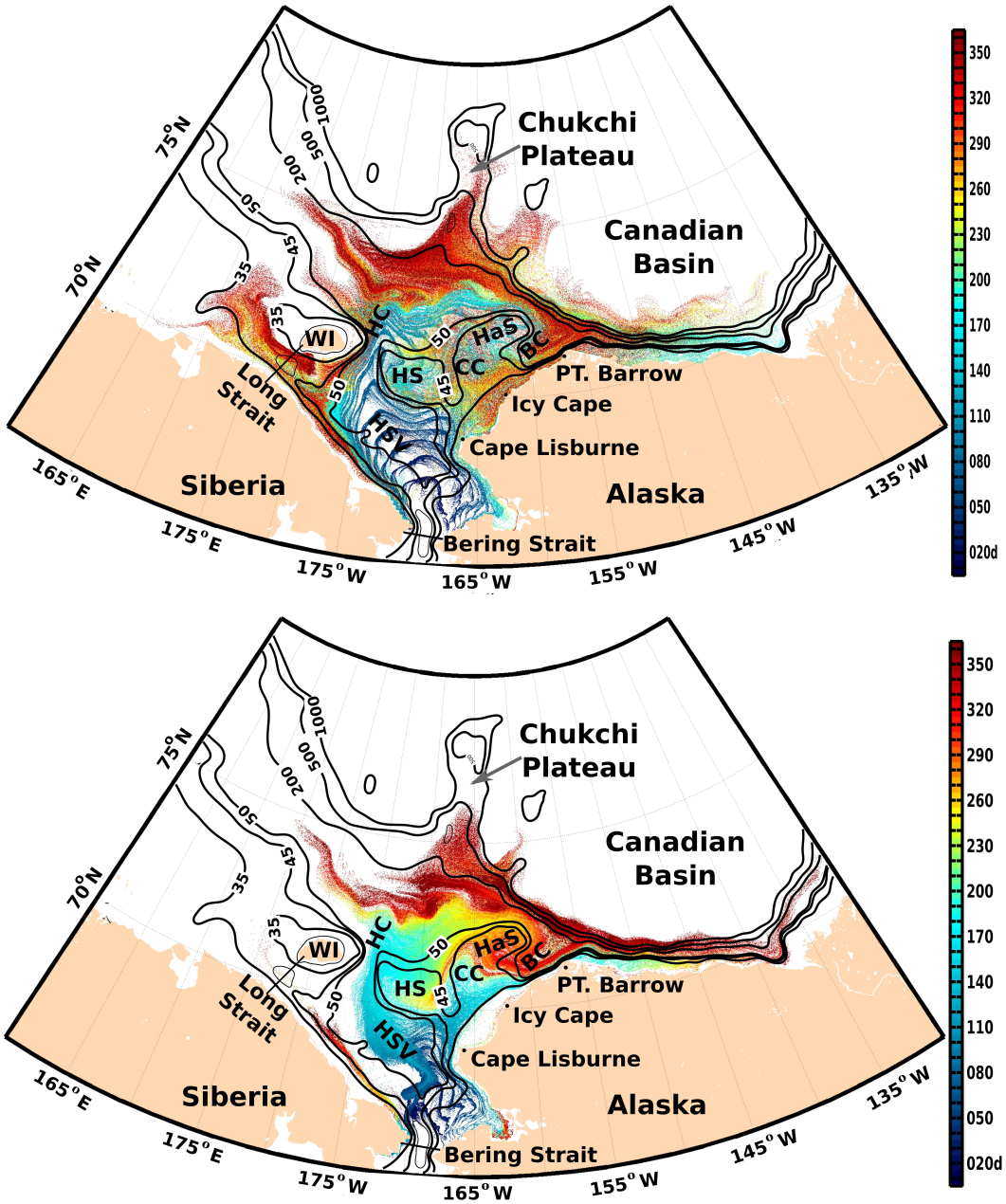

Figure 3.7: Pathways of Pacific water parcels released in March (upper) and September (lower) of year 5 in the Chukchi Sea (colors represent the integration time in days, contour lines represent water depths). (WI: Wrangel Island; HC: Herald Canyon; HS: Herald Shoal; CC: Central Channel; HaS: Hanna Shoal; BC: Barrow Canyon; HSV: Hope Sea Valley)

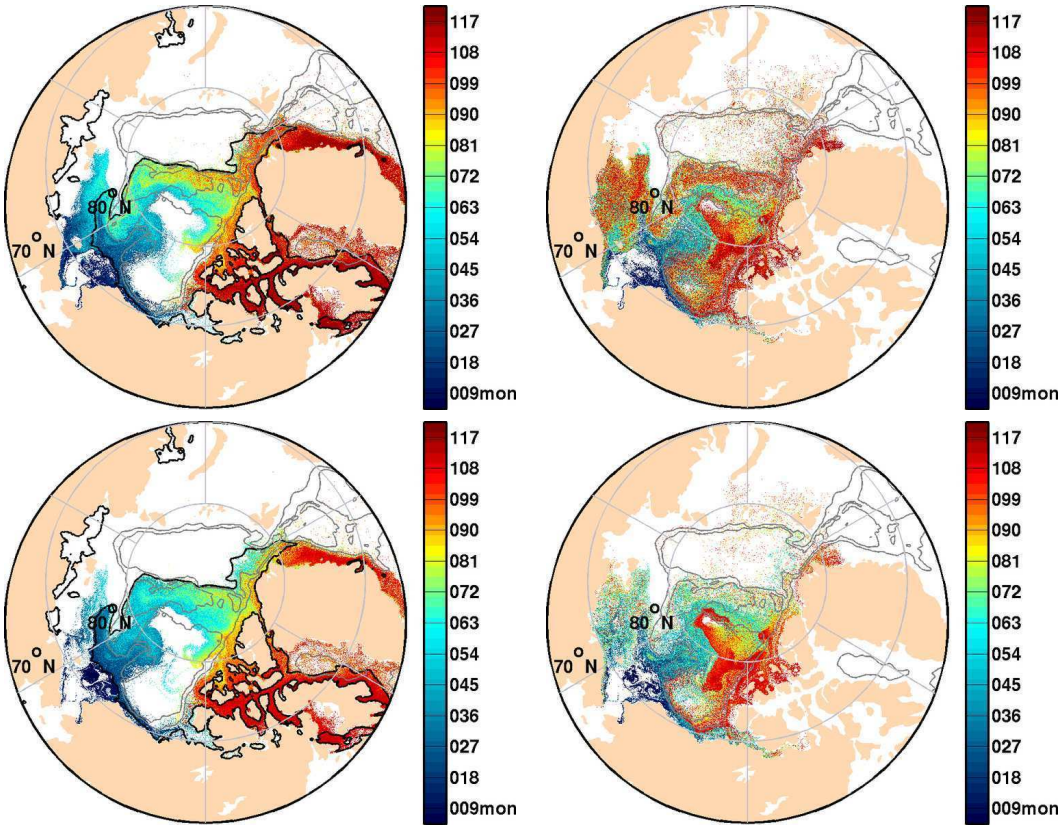

Figure 3.8: Pathways of Pacific water in the Arctic Ocean (left: those exiting either from Fram Strait or the CAA channels; right: trapped in the Arctic Ocean) within a 10-year integration starting from March (upper) and September (lower) of year 5 (colors: integration time in months, gray lines: $1000m$ and $2500m$ isodepth contours; black lines: $7m$-contour of annual freshwater content (upper $227m$))

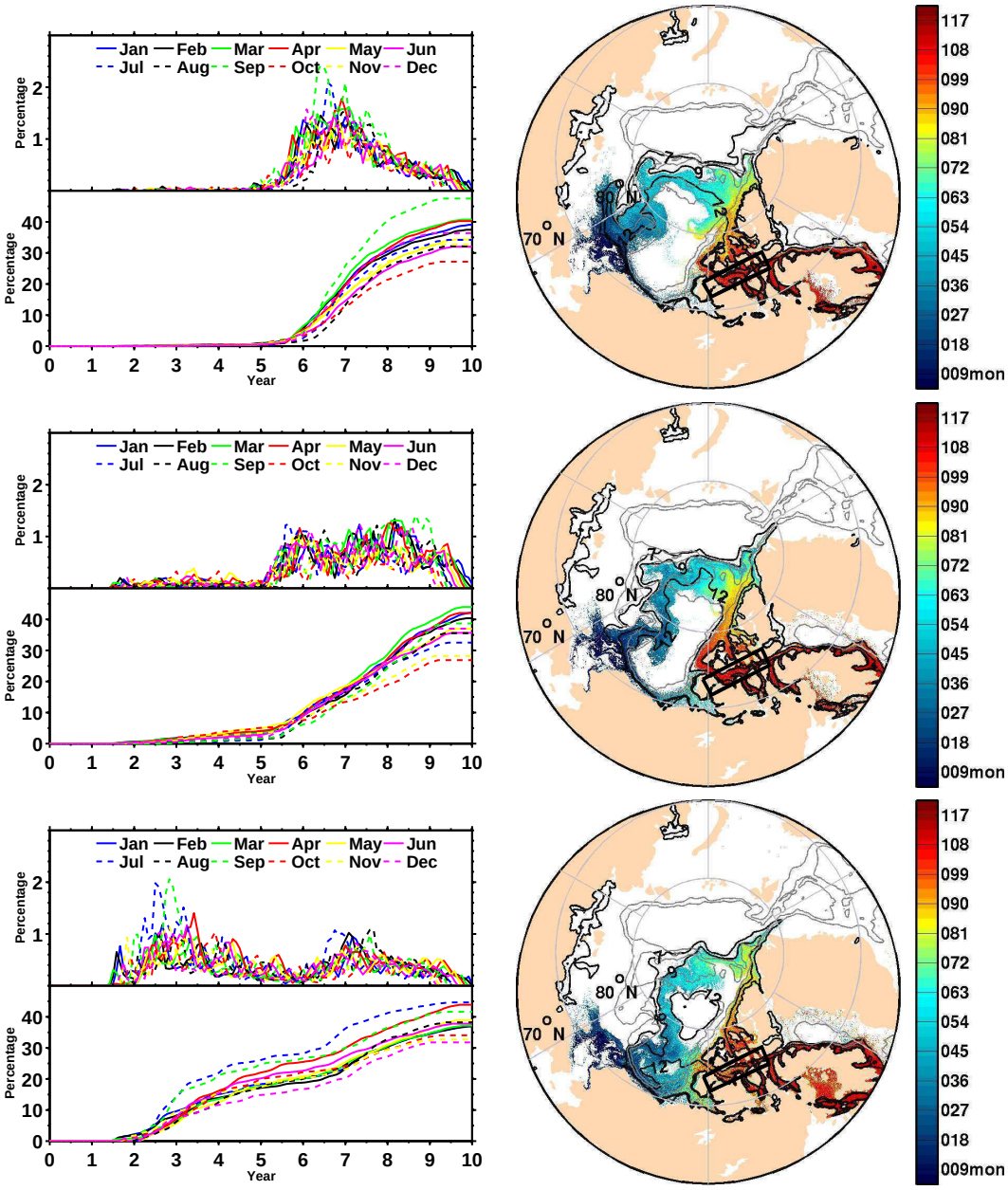

Figure 3.9: Travel time (left, similar to fig.3.6) and pathway of Pacific inflow water entering the central CAA (right, similar to fig.3.8 but released in July of the corresponding year; 7 m, 9 m and 12 m-contours of annual freshwater content are shown in black lines) in year of 5 (top), 10 (center) and 15 (bottom)

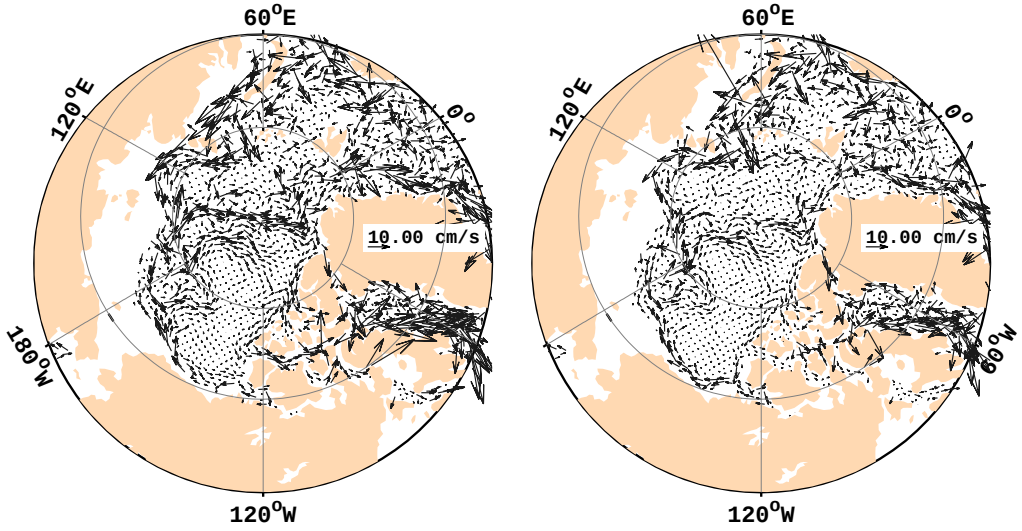

Figure 3.10: Annual mean upper $25 - 75\,m$ circulation in year 5 (only regions with a water depth $< 75\,m$ shown, left: geostrophic currents; right: simulated total currents)

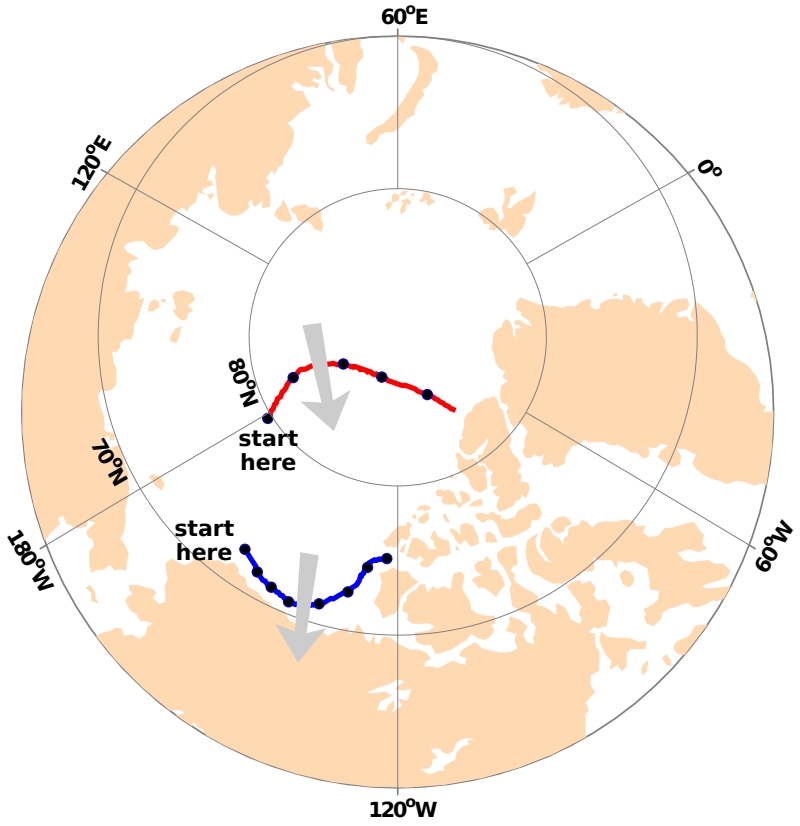

Figure 3.11: Selected sections along the Pacific water pathways (red: Transpolar route; blue: Alaskan route; black dots represent the locations of x-axis ticks in figures 3.12 and 3.13; gray arrows denote the normal-to-section direction)

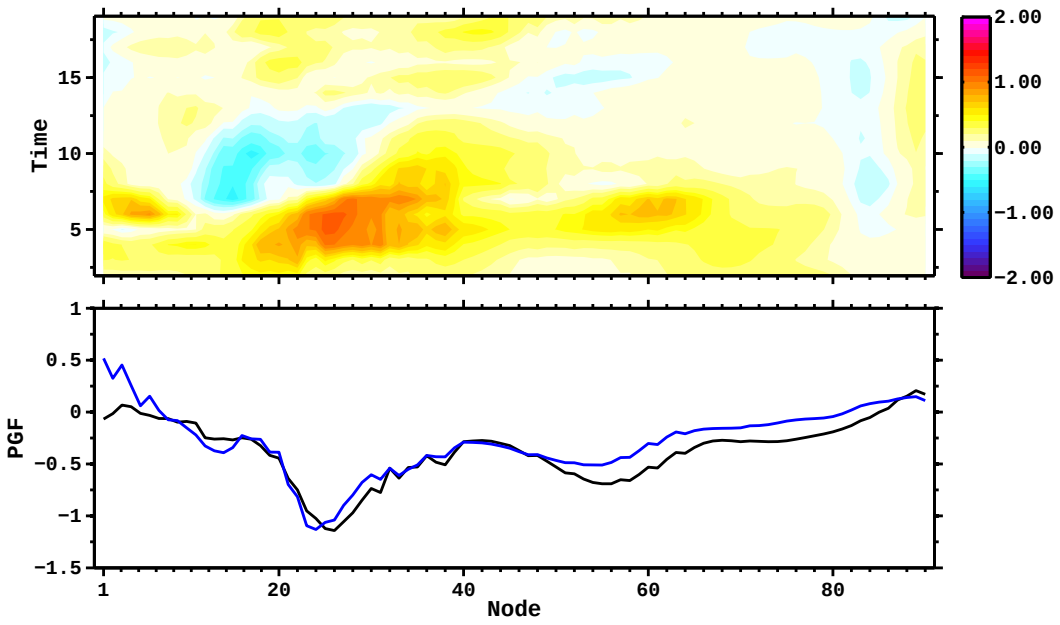

Figure 3.12: Evolution of annual mean normal-to-section pressure gradient force (PGF) along the Transpolar section (upper, time on y–axis is given in years) and the total (lower: black line) and salinity induced (lower: blue line) PGF difference (year 15 minus year 5). Unit: $10^{-5}\, m\, s^{-2}$

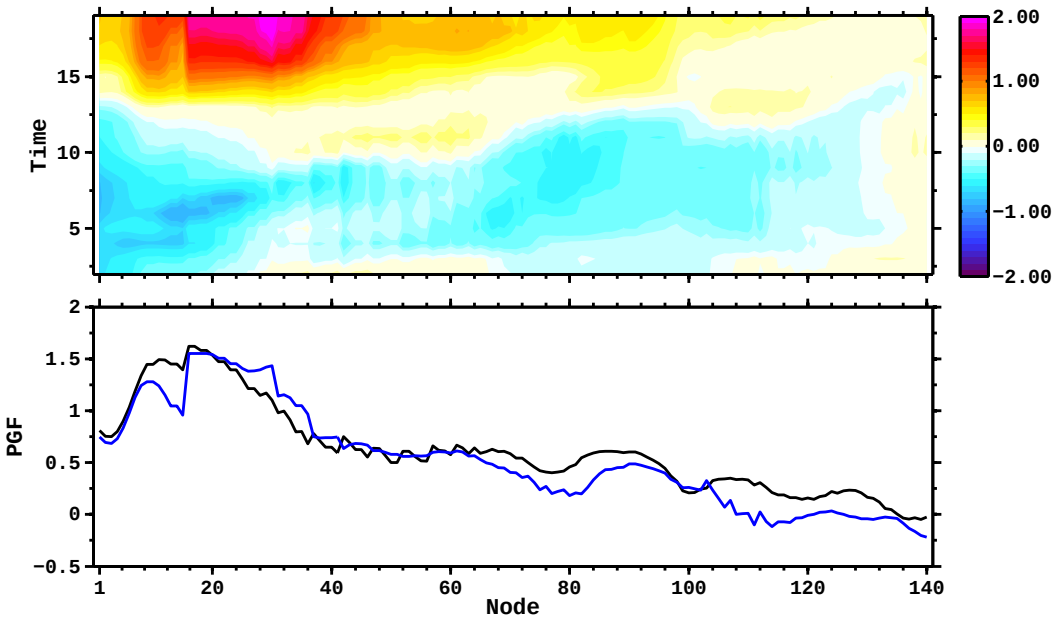

Figure 3.13: Same as figure 3.12 but along the Alaskan route

Bibliography

Aagaard, K., and E. C. Carmack (1989), The role of sea ice and other fresh water in the Arctic circulation, *Journal of Geophysical Research*, *94*(C10), 14,485–14,498.

Aagaard, K., L. K. Coachman, and E. C. Carmack (1981), On the halocline of the Arctic Ocean, *Deep Sea Research Part A. Oceanographic Research Papers*, *28*(6), 529–545.

Aagaard, K., T. J. Weingartner, S. L. Danielson, R. A. Woodgate, G. C. Johnson, and T. E. Whitledge (2006), Some controls on flow and salinity in Bering Strait, *Geophysical Research Letters*, *33*(19), L19,602.

Aksenov, Y., S. Bacon, A. C. Coward, and N. P. Holliday (2010), Polar outflow from the Arctic Ocean: A high resolution model study, *Journal of Marine Systems*, *83*, 14–37.

Alkire, M. B., K. K. Falkner, I. Rigor, M. Steele, and J. Morison (2007), The return of Pacific waters to the upper layers of the central Arctic Ocean, *Deep Sea Research Part I: Oceanographic Research Papers*, *54*(9), 1509–1529.

Alkire, M. B., K. K. Falkner, J. Morison, R. W. Collier, C. K. Guay, R. A. Desiderio, I. G. Rigor, and M. McPhee (2010), Sensor-based profiles of the NO parameter in the central Arctic and southern Canada Basin: New insights regarding the cold halocline, *Deep Sea Research Part I: Oceanographic Research Papers*, *57*(11), 1432–1443, doi:10.1016/j.dsr.2010.07.011.

Amante, C., and B. W. Eakins (2009), ETOPO1 1 Arc-minute global relief model: procedures, data sources and analysis, *NOAA Technical Memorandum NESDIS NGDC-24*, *19*.

Arakawa, A. K., and Y. J. G. Hsu (1990), Energy conserving and potential-enstrophy dissipating schemes for the shallow water equations, *Monthly Weather Review*, *118*(10), 1960–1969.

Barnier, B., et al. (2006), Impact of partial steps and momentum advection schemes in a global ocean circulation model at eddy-permitting resolution, *Ocean Dynamics*, *56*(5), 543–567, doi:10.1007/s10236.

Bauch, D., P. Schlosser, and R. G. Fairbanks (1995), Freshwater balance and the sources of deep and bottom waters in the Arctic Ocean inferred from the distribution of $H_2^{18}O$, *Progress in Oceanography*, *35*(1), 53–80.

Beszczynska-Möller, A., E. Fahrbach, U. Schauer, and E. Hansen (2012), Variability in Atlantic water temperature and transport at the entrance to the Arctic Ocean, 1997–2010, *ICES Journal of Marine Science*, *69*(5), 852–863, doi:10.1093/icesjms/fss056.

Blanke, B., and S. Raynaud (1997), Kinematics of the Pacific Equatorial Undercurrent: An Eulerian and Lagrangian approach from GCM results, *Journal of Physical Oceanography*, *27*(6), 1038–1053.

Blanke, B., M. Arhan, G. Madec, and S. Roche (1999), Warm water paths in the equatorial Atlantic as diagnosed with a general circulation model, *Journal of Physical Oceanography*, *29*(11), 2753–2768.

Bourke, R. H., and R. P. Garrett (1987), Sea ice thickness distribution in the Arctic Ocean, *Cold Regions Science and Technology*, *13*(3), 259–280.

Broecker, W. S., et al. (1998), How much deep water is formed in the Southern Ocean?, *Journal of Geophysical Research*, *103*(C8), 15,833–15,843, doi:10.1029/98JC00248.

Carmack, E. C., F. A. McLaughlin, M. Yamamoto-Kawai, M. Itoh, K. Shimada, R. Krishfield, and A. Y. Proshutinsky (2008), Freshwater storage in the Northern Ocean and the special role of the Beaufort Gyre, *Arctic-Subarctic Ocean Fluxes: Defining the Role of the Northern Seas in Climate*, pp. 145–169.

Coachman, L. K., and K. Aagaard (1966), On the water exchange through Bering Strait, *Limnology and Oceanography*, *11*(1), 44–59.

Coachman, L. K., K. Aagaard, and R. B. Tripp (1975), *Bering Strait: The regional physical oceanography*, 172 pp., University of Washington Press, Seattle, WA.

Comiso, J. C., C. L. Parkinson, R. Gersten, and L. Stock (2008), Accelerated decline in the Arctic sea ice cover, *Geophysical Research Letters*, *35*(1), L01,703.

Condron, A., P. Winsor, C. Hill, and D. Menemenlis (2009), Simulated response of the Arctic freshwater budget to extreme NAO wind forcing, *Journal of Climate*, *22*(9), 2422–2437.

Cuny, J., P. B. Rhines, and R. Kwok (2005), Davis Strait volume, freshwater and heat fluxes, *Deep Sea Research Part I: Oceanographic Research Papers*, *52*(3), 519–542, doi:10.1016/j.dsr.2004.10.006.

Curry, B., C. M. Lee, and B. Petrie (2011), Volume, freshwater, and heat fluxes through Davis Strait, 2004–05, *Journal of Physical Oceanography*, *41*(3), 429–436, doi:10.1175/2010JPO4536.1.

Ekwurzel, B., P. Schlosser, R. A. Mortlock, R. G. Fairbanks, and J. H. Swift (2001), River runoff, sea ice meltwater, and Pacific water distribution and mean residence times in the Arctic Ocean, *Journal of Geophysical Research*, *106*(C5), 9075–9092.

Fichefet, T., and M. A. M. Maqueda (1997), Sensitivity of a global sea ice model to the treatment of ice thermodynamics and dynamics, *Journal of Geophysical Research*, *102*(C6), 12,609–12,646, doi:10.1029/97JC00480.

Grebmeier, J. M., L. W. Cooper, H. M. Feder, and B. I. Sirenko (2006), Ecosystem dynamics of the Pacific-influenced northern Bering and Chukchi seas in the Amerasian Arctic, *Progress in Oceanography*, *71*(2-4), 331–361.

Häkkinen, S., and A. Y. Proshutinsky (2004), Freshwater content variability in the Arctic Ocean, *Journal of Geophysical Research*, *109*(C3), C03,051.

Hunke, E. C., and J. K. Dukowicz (1997), An elastic-viscous-plastic model for sea ice dynamics, *Journal of Physical Oceanography*, *27*(9), 1849–1867.

Jahn, A., L. B. Tremblay, R. Newton, M. M. Holland, L. A. Mysak, and I. A. Dmitrenko (2010a), A tracer study of the Arctic Ocean's liquid freshwater export variability, *Journal of Geophysical Research*, *115*(C7), C07,015.

Jahn, A., B. Tremblay, L. A. Mysak, and R. Newton (2010b), Effect of the large-scale atmospheric circulation on the variability of the Arctic Ocean freshwater export, *Climate Dynamics*, *34*(2), 201–222.

Jones, E. P., and L. G. Anderson (1986), On the origin of the chemical properties of the Arctic Ocean halocline, *Journal of Geophysical Research*, *91*(C9), 10,759–10.

Jones, E. P., L. G. Anderson, and J. H. Swift (1998), Distribution of Atlantic and Pacific waters in the upper Arctic Ocean: Implications for circulation, *Geophysical Research Letters*, *25*(6), 765–768.

Jones, E. P., J. H. Swift, L. G. Anderson, M. Lipizer, G. Civitarese, K. K. Falkner, G. Kattner, and F. A. McLaughlin (2003), Tracing Pacific water in the North Atlantic Ocean, *Journal of Geophysical Research*, *108*(C4), 3116.

Jones, E. P., L. G. Anderson, S. Jutterström, L. Mintrop, and J. H. Swift (2008), Pacific freshwater, river water and sea ice meltwater across Arctic Ocean basins: Results from the 2005 Beringia Expedition, *Journal of Geophysical Research*, *113*(C8), C08,012.

Kwok, R., and D. A. Rothrock (2009), Decline in Arctic sea ice thickness from submarine and ICESat records: 1958–2008, *Geophysical Research Letters*, *36*(15), L15,501.

Kwok, R., G. F. Cunningham, M. Wensnahan, I. Rigor, H. J. Zwally, and D. Yi (2009), Thinning and volume loss of the Arctic Ocean sea ice cover: 2003–2008, *Journal of Geophysical Research*, *114*(C7), C07,005.

Large, W. G., and S. G. Yeager (2004), Diurnal to decadal global forcing for ocean and sea-ice models: the datasets and flux climatologies. NCAR Technical Note TN–460+ STR, *National Center for Atmospheric Research*.

Lévy, M., A. Estublier, and G. Madec (2001), Choice of an advection scheme for biogeochemical models, *Geophysical Research Letters*, *28*(19), 3725–3728.

Lique, C., A. M. Treguier, B. Blanke, and N. Grima (2010), On the origins of water masses exported along both sides of Greenland: A Lagrangian model analysis, *Journal of Geophysical Research*, *115*(C5), C05,019.

Madec, G., and the NEMO team (2008), *NEMO ocean engine*, Note du Pôle de modélisation, Institut Pierre-Simon Laplace (IPSL), France, No 27, ISSN No 1288-1619.

McPhee, M. G., A. Y. Proshutinsky, J. H. Morison, M. Steele, and M. B. Alkire (2009), Rapid change in freshwater content of the Arctic Ocean, *Geophysical Research Letters*, *36*(10), L10,602, doi:10.1029/2009GL037525.

Murray, R. J. (1996), Explicit generation of orthogonal grids for ocean models, *Journal of Computational Physics*, *126*(2), 251–273.

Nguyen, A. T., D. Menemenlis, and R. Kwok (2011), Arctic ice-ocean simulation with optimized model parameters: Approach and assessment, *Journal of Geophysical Research*, *116*(C4), C04,025, doi:10.1029/2010JC006573.

Panteleev, G., D. A. Nechaev, A. Y. Proshutinsky, R. A. Woodgate, and J. Zhang (2010), Reconstruction and analysis of the Chukchi Sea circulation in 1990–1991, *Journal of Geophysical Research*, *115*(C8), C08,023.

Pickart, R. S., and G. Stossmeister (2008), Outflow of Pacific water from the Chukchi Sea to the Arctic Ocean, *Chinese Journal of Polar Science*, *19*(2), 135–148.

Proshutinsky, A. Y., R. H. Bourke, and F. A. McLaughlin (2002), The role of the Beaufort Gyre in Arctic climate variability: Seasonal to decadal climate scales, *Geophysical Research Letters*, *29*(23), 2100.

Proshutinsky, A. Y., et al. (2009), Beaufort Gyre freshwater reservoir: State and variability from observations, *Journal of Geophysical Research*, *114*(C1), C00A10.

Rabe, B., M. Karcher, U. Schauer, J. M. Toole, R. A. Krishfield, S. Pisarev, F. Kauker, R. Gerdes, and T. Kikuchi (2011), An assessment of Arctic Ocean freshwater content changes from the 1990s to the 2006–2008 period, *Deep Sea Research Part I: Oceanographic Research*, *58*, 173–185.

Roach, A. T., K. Aagaard, C. H. Pease, S. A. Salo, T. Weingartner, V. Pavlov, and M. Kulakov (1995), Direct measurements of transport and water properties through the Bering Strait, *Journal of Geophysical Research*, *100*(18), 443–18.

Rudels, B. (2001), Arctic Basin Circulation, in *Encyclopedia of Ocean Sciences*, edited by E. in Chief:John H. Steele, pp. 177–187, Academic Press, Oxford, doi:10.1006/rwos.2001.0372.

Schauer, U., E. Fahrbach, S. Osterhus, and G. Rohardt (2004), Arctic warming through the Fram Strait: Oceanic heat transport from 3 years of measurements, *Journal of Geophysical Research*, *109*(C6), C06,026.

Schauer, U., A. Beszczynska-Möller, W. Walczowski, E. Fahrbach, J. Piechura, and E. Hansen (2008), Variation of measured heat flow through the Fram Strait between 1997 and 2006, *Arctic-Subarctic Ocean Fluxes: Defining the Role of the Northern Seas in Climate*, pp. 65–85.

Serreze, M. C., et al. (2006), The large-scale freshwater cycle of the Arctic, *Journal of Geophysical Research*, *111*(C11), C11,010, doi:10.1029/2005JC003424.

Shimada, K., M. Itoh, S. Nishino, F. A. McLaughlin, E. C. Carmack, and A. Y. Proshutinsky (2005), Halocline structure in the Canada Basin of the Arctic Ocean, *Geophysical Research Letters*, *32*, L03,605.

Shimada, K., T. Kamoshida, M. Itoh, S. Nishino, E. C. Carmack, F. A. McLaughlin, S. Zimmermann, and A. Y. Proshutinsky (2006), Pacific Ocean inflow: Influence on catastrophic reduction of sea ice cover in the Arctic Ocean, *Geophysical Research Letters*, *33*(8), L08,605.

Sigman, D. M., S. L. Jaccard, and G. H. Haug (2004), Polar ocean stratification in a cold climate, *Nature*, *428*(6978), 59–63.

Skagseth, Ø., T. Furevik, R. Ingvaldsen, H. Loeng, K. A. Mork, K. A. Orvik, and V. Ozhigin (2008), Volume and heat transports to the Arctic Ocean via the Norwegian and Barents Seas, *Arctic-Subarctic Ocean Fluxes: Defining the Role of the Northern Seas in Climate*, pp. 45–64.

Smedsrud, L. H., R. Ingvaldsen, J. E. Nilsen, and Ø. Skagseth (2010), Heat in the Barents Sea: Transport, storage, and surface fluxes, *Ocean Science*, *6*(1), 219–234.

Spall, M. A. (2007), Circulation and water mass transformation in a model of the Chukchi Sea, *Journal of Geophysical Research*, *112*(C5), C05,025.

Steele, M., and W. Ermold (2007), Steric sea level change in the Northern Seas, *Journal of Climate*, *20*(3), 403–417, doi:10.1175/JCLI4022.1.

Steele, M., R. Morley, and W. Ermold (2001), PHC: A global ocean hydrography with a high-quality Arctic Ocean, *Journal of Climate*, *14*(9), 2079–2087.

Steele, M., J. Morison, W. Ermold, I. Rigor, M. Ortmeyer, and K. Shimada (2004), Circulation of summer Pacific halocline water in the Arctic Ocean, *Journal of Geophysical Research*, *109*(C2), C02,027.

Watanabe, E. (2011), Beaufort shelf break eddies and shelf-basin exchange of Pacific summer water in the western Arctic Ocean detected by satellite and modeling analyses, *Journal of Geophysical Research*, *116*(C8), C08,034.

Watanabe, E., and H. Hasumi (2009), Pacific water transport in the western Arctic Ocean simulated by an eddy-resolving coupled sea ice-ocean model, *Journal of Physical Oceanography*, *39*(9), 2194–2211.

Weingartner, T., K. Aagaard, R. A. Woodgate, S. Danielson, Y. Sasaki, and D. Cavalieri (2005), Circulation on the north central Chukchi Sea shelf, *Deep Sea Research Part II: Topical Studies in Oceanography*, *52*(24-26), 3150–3174.

Weingartner, T. J., S. Danielson, Y. Sasaki, V. Pavlov, and M. Kulakov (1999), The Siberian Coastal Current: A wind-and buoyancy-forced arctic coastal current, *Journal of Geophysical Research*, *104*(C12), 29,697–29.

Winsor, P., and D. C. Chapman (2004), Pathways of Pacific water across the Chukchi Sea: A numerical model study, *Journal of Geophysical Research*, *109*(C3), C03,002.

Woodgate, R. A., and K. Aagaard (2005), Revising the Bering Strait freshwater flux into the Arctic Ocean, *Geophysical Research Letters*, *32*(2), L02,602.

Woodgate, R. A., K. Aagaard, and T. J. Weingartner (2005a), Monthly temperature, salinity, and transport variability of the Bering Strait through flow, *Geophysical Research Letters*, *32*(4), L04,601.

Woodgate, R. A., K. Aagaard, and T. J. Weingartner (2005b), A year in the physical oceanography of the Chukchi Sea: Moored measurements from autumn 1990-1991, *Deep Sea Research Part II: Topical Studies in Oceanography*, *52*(24-26), 3116–3149.

Woodgate, R. A., K. Aagaard, and T. J. Weingartner (2006), Interannual changes in the Bering Strait fluxes of volume, heat and freshwater between 1991 and 2004, *Geophysical Research Letters*, *33*(15), L15,609.

Woodgate, R. A., T. J. Weingartner, and R. Lindsay (2010), The 2007 Bering Strait oceanic heat flux and anomalous Arctic sea-ice retreat, *Geophysical Research Letters*, *37*(1), L01,602.

Yamamoto-Kawai, M., F. A. McLaughlin, E. C. Carmack, S. Nishino, and K. Shimada (2008), Freshwater budget of the Canada Basin, Arctic Ocean, from salinity, δ^{18}O, and nutrients, *Journal of Geophysical Research*, *113*(C1), C01,007.

Chapter 4

Impact of Enhanced Melt from West Greenland on the Canadian Arctic Archipelago Throughflow

[1]

[1]A version of this chapter has been submitted for publication. Hu, X. and Myers P.G. 2013, Impact of Enhanced Melt from West Greenland on the Canadian Arctic Archipelago Throughflow, Geophysical Research Letters

Abstract

Here we investigate the impact of enhanced runoff from west Greenland on Baffin Bay, the transport of the CAA and freshwater fluxes south through Davis Strait into the Labrador Sea. Modelling experiments show a significant storage of the added freshwater in Baffin Bay on inter-annual timescales, with reductions of salinity in the upper water column and increases in freshwater content. The changes in freshwater content raise the dynamic height in Baffin Bay, reducing the height difference across the CAA. This leads to a reduction in volume and freshwater transports through the CAA and leads to enhanced transport at Fram Strait to compensate. The net result of the enhanced freshwater storage in Baffin Bay, combined with the reductions in CAA transport, is that little or no signal of the added runoff from west Greenland is seen flowing south at Davis Strait, at least on inter-annual timescales.

4.1 Introduction

The Greenland ice sheet is a massive reservoir of freshwater in the form of ice. Greenland loses ice through both runoff and ice dynamics/calving (*van den Broeke et al.*, 2009). *Box et al.* (2006), using a regional climate model calibrated with observations, suggest an annual mean runoff between 1988 and 2004 of $373\,km^3\,yr^{-1}$. *van den Broeke et al.* (2009) found, using satellite gravity observations, an equal partitioning of the mass loss between surface processes and ice dynamics. Based on a literature review, *Dickson et al.* (2007) suggested $18\,mSv$ (roughly $550\,km^3\,yr^{-1}$) of total discharge from Greenland. Studies have shown recent acceleration in the discharge rate, potentially associated with a warming high latitude climate, such as *Box et al.* (2006) who found a linear change of $112\,km^3\,yr^{-1}$ over 1998 to 2004.

This discharge is not partitioned evenly around Greenland. *van den Broeke et al.* (2009) find about half of the mass loss from the ice sheet is found in the southeast. They (*van den Broeke et al.*, 2009) also find areas of significant mass loss along the west and northern coasts of Greenland as well. *Khan et al.* (2010) found that significant increases in ice loss were spreading up the northwest coast of Greenland post 2005. These regional changes in west Greenland may be related to glacier acceleration observed in this region related to the provision of warm Irminger Water to the coastal fjords (*Holland et al.*, 2008).

Besides sea level rise, there is also interest in freshwater discharge from Greenland due to its impact on ocean stratification and possibly deep water formation, several sites of which are located close to Greenland. Increase melt from southeast (and southwest) Greenland would be expected to end up in the Labrador Sea, and there may be some evidence of this signal in the West Greenland Current (*Myers et al.*, 2009). Enhanced discharge from northwest Greenland will enter Baffin Bay before being exported south through Davis Strait into the Labrador Sea.

Greenland is not the only significant source of low salinity water to Baffin Bay. Freshwater, mainly in the liquid form, is exported from the Arctic Ocean through the Canadian Arctic Archipelago (CAA) into Baffin Bay. Relative to a salinity of 34.8, *Cuny et al.* (2005) estimated the southward transport of freshwater at Davis Strait as $92 \pm 34\,mSv$ over 3 year mooring deployment between 1987 and 1990. While analyzing all studies, including unpublished recent measurements, *Dickson et al.* (2007) suggested a range of 72-130 mSv to bracket all estimates.

Within the CAA, *Prinsenberg and Hamilton* (2005) showed at Barrow Strait that the variability of freshwater transport closely followed the variability of the volume transport. *Cuny et al.* (2005) estimated the southward volume transport at Davis Strait as $-2.6 \pm 1.0\,Sv$. *Kliem and Greenberg* (2003) showed that the magnitude of the transport through the CAA as well as the partitioning between different straits depended on the elevation difference across the archipelago.

This last point leads to the question that if Greenland freshwater discharge is enhanced, will Baffin Bay act just as a conduit for exporting this additional freshwater or will it store part of the signal, impacting its sea level and dynamic height. And if the dynamic height rises in Baffin Bay, will that reduce the volume and freshwater transports through the CAA? And if the CAA freshwater transport is reduced, will this reduction partially offset the increased Greenland discharge, thus leading to only small changes in the export of freshwater through Davis Strait, at least over inter-annual timescales. This question we will examine with a modelling sensitivity study applying varying amounts of additional freshwater discharge as runoff from west Greenland.

4.2 Model and Experiments

Simulations are carried using a coupled ocean/sea ice model, NEMO (*Madec and the NEMO team*, 2008), run using a regional configuration covering the

northern Bering Sea, Arctic Ocean, CAA, Nordic Seas and part of the North Atlantic Ocean (inset of Fig. 4.1a) with a variable horizontal resolution of 11 km in the central CAA and 15 km in the Arctic Ocean, and 46 vertical levels. The model is initialized with the PHC3.0 climatology and forced with CORE normal year forcing. There is no surface relaxation for either temperature or salinity, which is important for ensuring that freshwater signals are not damped. Open boundary information is taken from a global $\frac{1}{4}^o$ hindcast using the NEMO model (experiment ORCA025-KAB001, *Barnier et al.* (2006)).

A control experiment (RUNOFF0), with little ($<$ 1 mSv) runoff from Greenland, was run for 5 years using perpetual year forcing. Four additional sensitivity experiments were carried out, each for 5 years, applying additional runoff along the coast of west Greenland (see inset of Fig. 4.1a), with the runoff evenly distributed over May to October of each year. The added runoffs of 5 mSv (RUNOFF10), 12.5 mSv (RUNOFF25), 25 mSv (RUNOFF50) and 50 mSv (RUNOFF100) were chosen to bracket observed changes in Greenland freshwater discharge as well as to investigate the response to larger signals.

4.3 Results

Although 5 year integrations are not long enough for the model to reach a final steady state, it is long enough for the initial transient behavior to start to level off and clear impacts of the enhanced Greenland melt to be observed. The majority of the added runoff enters Baffin Bay, reducing the salinity averaged over that basin (see inset of Fig. 4.1a). The salinity decreases over the summer input period, reaching a minimum in late fall, before increasing in a linear fashion by amounts ranging from 0.01 in RUNOFF10 to 0.1 in RUNOFF100. The rapid increase in freshwater content each summer can clearly be seen, referenced to a salinity of 34.8 (Fig. 4.1a), as a quasi-linear increase with the size of the added runoff.

One impact of this salinity decrease in Baffin Bay is to increase the dynamic

height. We follow *Steele and Ermold* (2007) and calculate dynamic height as the vertically integrated departure of density ρ at temperature T, salinity S and pressure P from a standard reference value ρ_{ref}, $DH = \int_{3000m}^{0m} \left(\frac{\rho_{ref} - \rho_{T,S,P}}{\rho_{ref}} \right) dz$. The spatial pattern in dynamic height change is consistent in all experiments (Fig. 4.1c-f), with largest increases along the west Greenland coast, in northern Baffin Bay as well as near Davis Strait. That said, increases are seen over almost all of Baffin Bay as well as north of the CAA and Greenland through to Fram Strait and in the East Greenland Current. Since the increases in dynamic height are not uniform, they generate anomalous currents that act to enhance the West Greenland Current (and East Greenland Current) while weakening the flows through the archipelago. The integrated effect is to raise the dynamic heights in Baffin Bay between $0.01\,m$ in RUNOFF10 to $0.075\,m$ in RUNOFF100 (Fig. 4.1b). The increase in dynamic height is close to linear for smaller freshwater inputs, falling off to less than linear for higher inputs.

Although there is a small increase in dynamic heights north of the CAA, this is a consequence of the increases in Baffin Bay impacting the fluxes from the Arctic Ocean. In other words, in all experiments, the cross-archipelago dynamic height gradient has decreased. As seen with the velocity anomalies (Fig. 4.1c-f), the flows from the Arctic Ocean to Baffin Bay have been weakened, which will impact the volume transports (Fig. 4.2). All 3 of the main pathways through the CAA (Lancaster Sound, Jones Sound, Nares Strait) show similar behavior, with the volume transport decreasing as the runoff from Greenland is increased (Tab. 4.1). For Jones Sound (which is impacted most by the additional freshwater) and Nares Strait, there is even a transport reversal for part of the year in the experiments with the most added runoff, as the dynamic height in northern Baffin Bay exceeds that north of the archipelago. The result is a net reduction of CAA throughflow with enhanced west Greenland runoff. This reduction is compensated by enhanced export from the Arctic Ocean through Fram Strait.

These changes in the volume fluxes impact the freshwater fluxes through

the CAA (Fig. 4.3). Again, for all 3 straits, the freshwater flux from the Arctic Ocean decreases with the volume transport and the enhanced freshwater from west Greenland. The size of the reduction varies from 51 % for RUNOFF10 to 31 % for RUNOFF100. As the total freshwater flux through the CAA decreases, it is compensated for by enhanced freshwater export from the Arctic through Fram Strait. This compensation is almost complete in RUNOFF10 and RUNOFF25, while it is only $75-80$ % in the two larger runoff experiments, implying more storage of freshwater in the Arctic Ocean.

4.4 Summary and Discussion

Here we investigate the impact of enhanced runoff from west Greenland on Baffin Bay, the transport of the CAA and freshwater fluxes south through Davis Strait into the Labrador Sea. All experiments show a significant storage of the added freshwater in Baffin Bay on inter-annual timescales, with reductions of salinity in the upper water column and increases in freshwater content. This change in freshwater content raise the dynamic height in Baffin Bay, reducing the height difference across the CAA. This leads to a reduction in volume and freshwater transports through the CAA and leads to enhanced transport at Fram Strait to compensate.

There is little change in the net freshwater export from the Arctic, so the overall freshwater budget of that basin and the sub-polar North Atlantic will not be impacted (although we note we only consider discharge from west Greenland here). But the spatial distribution of this freshwater may be impacted. With greater transports through Fram Strait, more of the Arctic freshwater may end up in the Nordic Seas.

However, these results also suggest that added melt from west Greenland glaciers (at least those in Baffin Bay) may not be rapidly seen in the Labrador Current and farther south. Much of the added freshwater is being stored in the upper layers of Baffin Bay. Additionally, the freshwater storage leads to

a significant reduction in the freshwater transport through the CAA. Looking at transports south through Davis Strait in the sensitivity experiments (Fig. 4.2d, Tab. 4.1), one sees basically no change in the southward freshwater transport in any of the sensitivity experiments except RUNOFF100, and even that increase is small (approx. $1\,mSv$). Thus storage and reduced CAA transports are compensating for the added discharge from west Greenland, with no signal of this enhancement at Davis Strait. Although one would expect this added freshwater to eventually be released from Baffin Bay, on short timescales, to observe the oceanic impact of west Greenland runoff, one needs to look salinity/freshwater changes in Baffin Bay and/or CAA transports.

4.5 Acknowledgments

This work was funded by an Natural Sciences and Engineering Research Council of Canada (NSERC) grant. We are grateful to Westgrid and Compute Canada for computational resources. We thank C. Boening and A. Biastoch for providing us model output that was used for model spin-up open boundary forcing.

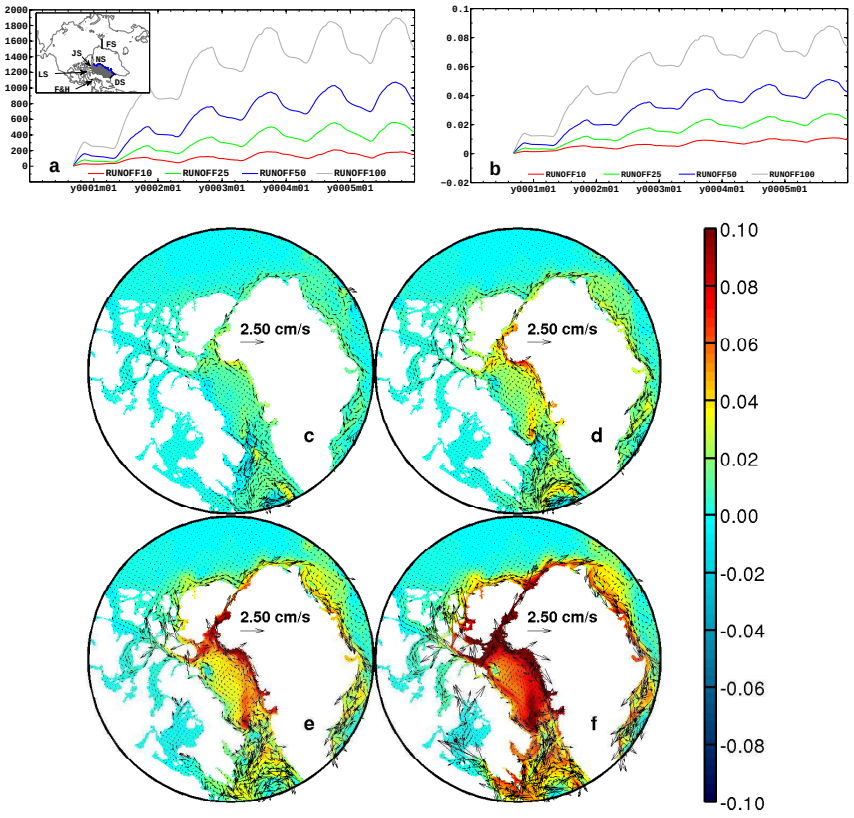

Figure 4.1: a) Freshwater content anomalies for the 4 sensitivity experiments, compared to CONTROL, averaged over Baffin Bay, in km^3 relative to 34.8. The inset panel shows the model domain, Baffin Bay (shaded region), the region where the additional freshwater was added (blue line along the west coast of Greenland) and the locations of sections used to estimate transports. b) Dynamic height anomalies for the 4 sensitivity experiments, compared to CONTROL, averaged over Baffin Bay. c) Spatial pattern of the dynamic height anomaly for RUNOFF10 compared to CONTROL (colour contours) with annual averaged velocity anomalies overlaid. Dynamic height is calculated as defined in equation 1. d) as for c) but for RUNOFF25. e) as for c) but for RUNOFF50. f) as for c) but for RUNOFF100.

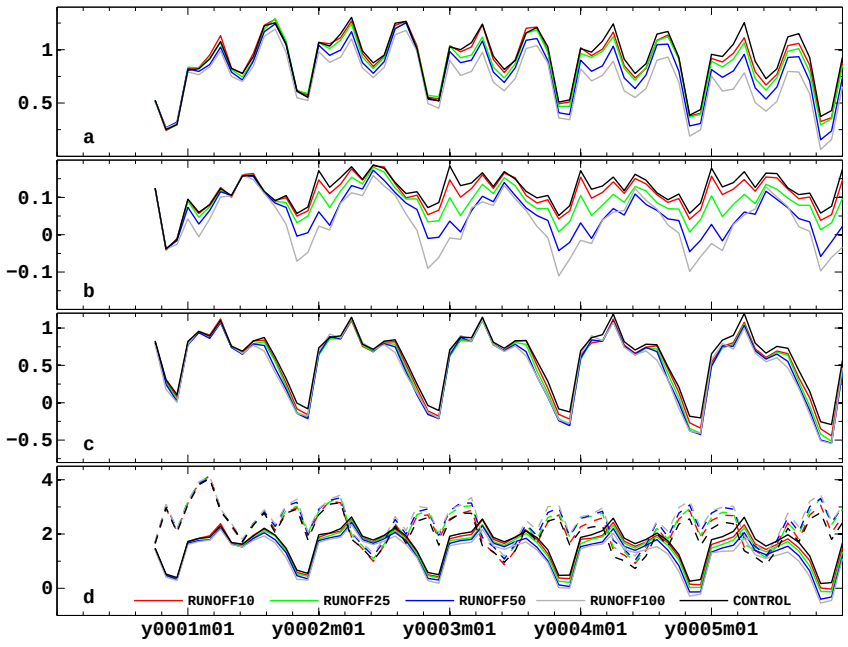

Figure 4.2: Timeseries of volume transports for CONTROL and the 4 sensitivity experiments for a) Lancaster Sound, b) Jones Sound, c) Nares Strait and d) a sum of the entire CAA (solid lines) plus Fram Strait (dashed lines). The section locations are shown on the inset in figure 4.1.

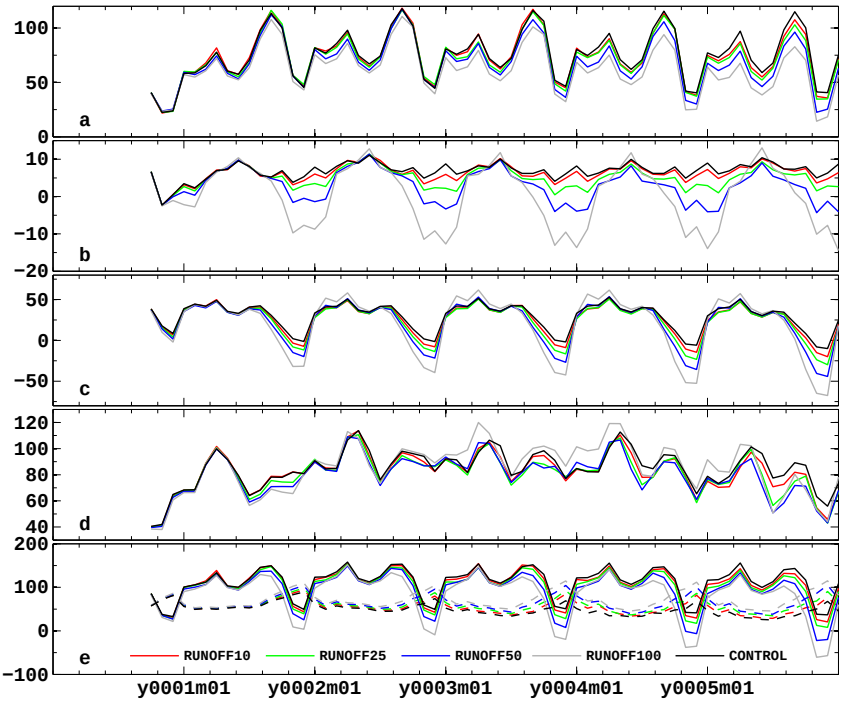

Figure 4.3: Timeseries of freshwater transports, relative to 34.8, for CONTROL and the 4 sensitivity experiments for a) Lancaster Sound, b) Jones Sound, c) Nares Strait, d) Davis Strait and e) a sum of the entire CAA (solid lines) plus Fram Strait (dashed lines). The section locations are shown on the inset in figure 4.1.

Table 4.1: Table of transports (volume in Sv and freshwater, relative to 34.8, in mSv) for our control and the 4 sensitivity experiments with additional west Greenland runoff

Experiment		Lancaster Sound	Nares Strait	Jones Sound	Fury and Hecla Strait	sum CAA	Fram Strait	Davis Strait
CONTROL	Volume	0.93	0.60	0.13	0.27	1.66	2.08	1.39
	Freshwater	77.8	29.2	7.2	27.2	114.2	48.6	86.8
RUNOFF10	Volume	0.91	0.55	0.11	0.28	1.57	2.20	1.30
	Freshwater	76.4	26.2	6.6	27.4	109.2	53.9	84.2
RUNOFF25	Volume	0.88	0.51	0.09	0.27	1.48	2.30	1.23
	Freshwater	74.7	23.8	5.2	27.3	103.7	58.7	82.4
RUNOFF50	Volume	0.82	0.50	0.06	0.26	1.37	2.40	1.14
	Freshwater	70.1	21.7	2.9	26.5	94.8	64.5	81.3
RUNOFF100	Volume	0.74	0.49	0.04	0.24	1.26	2.49	1.07
	Freshwater	64.0	19.2	0.2	24.8	83.4	71.4	87.3

Bibliography

Barnier, B., et al. (2006), Impact of partial steps and momentum advection schemes in a global ocean circulation model at eddy-permitting resolution, *Ocean Dynamics*, *56*(5), 543–567, doi:10.1007/s10236.

Box, J. E., D. H. Bromwich, B. A. Veenhuis, L.-S. Bai, J. C. Stroeve, J. C. Rogers, K. Steffen, T. Haran, and S.-H. Wang (2006), Greenland ice sheet surface mass balance variability (1988-2004) from calibrated Polar MM5 output, *Journal of Climate*, *19*(12), 2783–2800.

Cuny, J., P. B. Rhines, and R. Kwok (2005), Davis Strait volume, freshwater and heat fluxes, *Deep Sea Research Part I: Oceanographic Research Papers*, *52*(3), 519–542, doi:10.1016/j.dsr.2004.10.006.

Dickson, R., B. Rudels, S. Dye, M. Karcher, J. Meincke, and I. Yashayaev (2007), Current estimates of freshwater flux through Arctic and subarctic seas, *Progress in Oceanography*, *73*(3-4), 210–230.

Holland, D. M., R. H. Thomas, B. De Young, M. H. Ribergaard, and B. Lyberth (2008), Acceleration of Jakobshavn Isbrae triggered by warm subsurface ocean waters, *Nature Geoscience*, *1*(10), 659–664.

Khan, S. A., J. Wahr, M. Bevis, I. Velicogna, and E. Kendrick (2010), Spread of ice mass loss into northwest Greenland observed by GRACE and GPS, *Geophysical Research Letters*, *37*(6).

Kliem, N., and D. A. Greenberg (2003), Diagnostic simulations of the summer

circulation in the Canadian Arctic Archipelago, *Atmosphere-Ocean*, *41*(4), 273–289.

Madec, G., and the NEMO team (2008), *NEMO ocean engine*, Note du Pôle de modélisation, Institut Pierre-Simon Laplace (IPSL), France, No 27, ISSN No 1288-1619.

Myers, P. G., C. Donnelly, and M. H. Ribergaard (2009), Structure and variability of the West Greenland Current in summer derived from 6 repeat standard sections, *Progress in Oceanography*, *80*(1), 93–112.

Prinsenberg, S. J., and J. Hamilton (2005), Monitoring the volume, freshwater and heat fluxes passing through Lancaster Sound in the Canadian Arctic Archipelago, *Atmosphere-Ocean*, *43*(1), 1–22.

Steele, M., and W. Ermold (2007), Steric sea level change in the Northern Seas, *Journal of Climate*, *20*(3), 403–417, doi:10.1175/JCLI4022.1.

van den Broeke, M., J. Bamber, J. Ettema, E. Rignot, E. Schrama, W. J. van de Berg, E. van Meijgaard, I. Velicogna, and B. Wouters (2009), Partitioning recent Greenland mass loss, *Science*, *326*(5955), 984–986, doi: 10.1126/science.1178176.

Chapter 5

Projected Changes to the Canadian Arctic Archipelago Sea Ice in the 21st Century

Abstract

A coupled ocean and sea-ice pan-Arctic model forced by the projected IPCC A1B climate forcing scenario is used to study the evolution of ice and ocean surface condition within the Canadian Arctic Archipelago (CAA) in the 21st century. Sea ice experiences significant changes from the mid 2020s to the mid 2060s in both concentration and thickness. The simulation shows a shrinking of 65% and thinning of 75% in summer over the 40 years, resulting in the opening of Northwest Passage (NWP) by the 2050s. A summer ice-free CAA is likely by the end of our simulation. With a lower albedo, a warmer ocean is simulated, particularly in summer. The sea surface salinity within the CAA demonstrates a strong decadal oscillation without a clear trend over the whole simulation. A north-south pattern, separated by the Parry Channel, is also found in the changes of ocean temperature and salinity fields due to different ice conditions.

5.1 Introduction

Sea ice is an important factor in the high latitude climate system, affecting the exchanges of momentum, heat, and freshwater (mass) fluxes between the atmosphere and ocean. Beside the local processes, via the meridional transport, it also plays a key role in global climate changes. Since satellite observation became available in the late 1970s, numerous studies have presented the significant decrease in ice area in the Arctic Ocean, particularly in recent years (e.g., *Parkinson et al.*, 1999; *Serreze et al.*, 2007; *Parkinson and Cavalieri*, 2008; *Stroeve et al.*, 2008; *Comiso et al.*, 2008; *Parkinson and Comiso*, 2013). The thinning of ice thickness also has been revealed by submarine and recent remote sensing data (*Rothrock et al.*, 1999, 2008; *Haas et al.*, 2008; *Kwok et al.*, 2009; *Kwok and Rothrock*, 2009). A series of low Arctic sea ice records (*Serreze et al.*, 2003; *Stroeve et al.*, 2008; *Comiso et al.*, 2008; *Kauker et al.*, 2009; *Parkinson and Comiso*, 2013) have raised more concerns about the fate of Arctic sea ice and possible consequences. Numerical simulations suggest a seasonal ice-free Arctic Ocean is very likely to happen in the near future (e.g., *Boé et al.*, 2009; *Wang and Overland*, 2009, 2012).

The Canadian Arctic Archipelago (CAA) is a large and complex Arctic Ocean shelf in the north of Canada (figure 3.1). It is an important connection between the Arctic and Atlantic Oceans. On one hand, it delivers the cold fresh polar water (liquid freshwater) and a small amount of sea ice (solid freshwater) to the downstream Labrador Sea (*Peterson et al.*, 2012), which is an important site for open ocean deep convection (e.g., *Marshall and Schott*, 1999). Numerical experiments have shown that such an outflow of freshwater could significantly affect the formation of dense water and the overturning circulation (e.g., *Goosse et al.*, 1997; *Komuro and Hasumi*, 2005). On the other hand, with so many narrow straits, it also works as a buffer zone for sea ice, preventing faster outflow of multi-year sea ice from the Arctic Ocean to Baffin Bay (*Sou and Flato*, 2009). About $\sim$ 10% of the total Northern

Hemisphere sea ice is stored within the CAA (*Lietaer et al.*, 2008). Due to the harsh climate and complicated network of narrow channels, the in-situ or remote sensing data available in this region has lots of limitations. Still, ice retreat has already been noticed in the CAA region in recent years (*Howell et al.*, 2009).

Besides the local oceanic and long-term climate impacts, the decline of sea ice within the CAA is also meaningful for local ecosystems. A thinner ice cover in this region possibly extends the habitat of some large marine mammals (*Moore and Huntington*, 2008; *Wang et al.*, 2012). Also as consequences of ice melting, the ocean physical properties, e.g., sea surface temperature (SST) and salinity (SSS), could be changed significantly. Although marine species do have certain abilities to adapt to the changing environment, whether they can catch up with such a fast pace of climate change in the future is still a question.

In addition, the disappearance of sea ice is of importance to commercial shipping. Starting with Lancaster Sound from the east, the Northwest Passage (NWP) has three possible paths in the west (M'Clure Strait, Prince of Wales Strait and Peel Sound, figure 3.1). The NWP provides a shorter route between Europe and Asia by 9000 km than the current route through the Panama Canal (e.g., *Howell et al.*, 2008). Based on the historical observations, *Howell et al.* (2008) found there are still considerable amounts of multi-year ice forming in the western Parry Channel and M'Clintock Channel which means the whole NWP will still be not fully accessible in the near future, even for the least difficult route (through Peel Sound). But the low ice events in recent years (*Stroeve et al.*, 2008) have led to consideration that it will soon be time to expect the NWP to become a viable shipping route.

Currently, to study the ice condition within the CAA, particularly future climate scenarios, numerical model simulations are still a necessary and effective approach. Due to the complex topography, high resolution models are in need. However, the CAA was not well resolved by most climate models in

the IPCC's Fourth Assessment Report (*Solomon et al.*, 2007). Thus *Sou and Flato* (2009) utilized a regional ice-ocean model with a resolution of 22 km to simulate the sea ice within the CAA during 2041–2060, and found summer concentration and thickness decreased by 45% and 36% respectively, compared to their hindcasting run from 1950 to 2004. But there is still a lack of knowledge of the evolution of sea ice in different time periods in the 21st century.

The aim of this study is to simulate the possible variability of sea ice and ocean surface fields in the CAA in the context of a warmer climate with a relatively high resolution ocean/sea ice model. First we begin with a simple description of the numerical model and data used in this study. Then the model configuration validation and ice conditions (concentration and thickness) over different time periods (1986–2005, 2006–2025, 2026–2045, 2046–2065, 2066–2085) will be presented. After that, the changes of surface ocean fields (SST and SSS) will also be examined for a better view of the changes in the sea ice. Ten sites are also selected to study the trends in sea ice and ocean surface fields. A summary and discussion will be given in the end.

5.2 Method and Data

A pan-Arctic configuration numerical model based on the Nucleus for European Modelling of the Ocean (NEMO) numerical framework version 3.1 (*Madec and the NEMO team*, 2008) is used in this study. This coupled ocean and sea-ice model includes a three-dimensional, free surface, hydrostatic, primitive-equation ocean component and a dynamic-thermodynamic sea ice component. The sea ice module is from the Louvain-la-Neuve sea-ice model (LIM2) (*Fichefet and Maqueda*, 1997) with a modified elastic-viscous-plastic (EVP) ice rheology (*Hunke and Dukowicz*, 1997).

Our model domain covers the northern Bering Sea, the Arctic seas, and part of the North Atlantic Ocean (to 45 N°, see the inset of figure 3.1) with a variable horizontal resolution, from $\sim 11\,km$ within the central CAA region

to $\sim 15\,km$ in the Arctic Ocean. When generating the horizontal mesh grids, an orthogonal transformation method (*Murray*, 1996) is used to overcome the coordinate singularity at the North Pole in standard spherical grids and provide high enough resolution in the CAA region with limited grid points. In the vertical, 46 z-levels are used with layer thickness smoothly varying from $\sim 6m$ at the surface to $\sim 240m$ at the bottom. The bathymetry data is derived from the global 1 arc-minute resolution relief dataset (ETOPO1) (*Amante and Eakins*, 2009) provided by the US National Geophysical Data Center (NGDC).

We first spin up the model for 18 years with initial ocean temperature and salinity from Polar Science Center Hydrostatic Climatology (PHC3.0) (*Steele et al.*, 2001), normal year atmospheric forcing (10-m surface wind, 10-m air temperature and specific humidity, downward longwave and shortwave radiation, total precipitation and snowfall) from the Coordinated Ocean-ice Reference Experiments (CORE2) (*Large and Yeager*, 2009), monthly runoff data from a global model (ORCA05 MGP), and eastern and western open boundary data (normal and meridional velocity, temperature and salinity) from a global simulation (ORCA025-KAB001) (*Barnier et al.*, 2006). No temperature and salinity restoring is active except for the buffer zones close to the open boundaries and in Foxe Basin. More details can be found in *Hu and Myers* (2013). Starting from the spin-up state, we performed two subsequent simulations: a) an inter-annual (1970–1999) simulation forced by the monthly atmospheric output (including runoff) from the 20th century climate experiment (20c3m) of the UK Met Office Hadley Centre Coupled Ocean-Atmosphere GCM (HadCM3) (*Gordon et al.*, 2000) with a horizontal resolution of $3.75° \times 2.5°$, and b) a "future scenario" (2000–2100) simulation forced by the monthly atmospheric output (including runoff) from HadCM3 run under the Special Report on Emission Scenario (SRES) A1B scenario (*IPCC*, 2000). Monthly ocean open boundary conditions were taken from the corresponding runs of the Canadian Centre for Climate Modelling and Analysis (CCCma) CGCM3.1 ($\sim 1.4° \times 0.94°$) (*Flato and Boer*, 2001).

Due to the low resolution of atmospheric model fields, we were concerned that local biases could affect the high resolution ocean simulations. Thus, here we employ a similar approach to *Dumas et al.* (2006), adding the difference between the monthly output from HadCM3 and the average over 1970–1999 to the climatology (CORE2 normal year data). For "large" value variables (surface air temperature and downward radiation), we added the mathematical difference from the mean to climatology

$$X_{new}(t) = X_{ori}(t) + (\bar{C}_{core} - \bar{C}_{1970-1999}) \tag{5.1}$$

where X_{new} is the new value, X_{ori} is the output from HadCM3, $\bar{C}_{core}$ is the CORE2 normal year value, $\bar{C}_{1970-1999}$ is the average of the output from HadCM3 over 1970–1999, and t is time. For "small" value variables (precipitation,snowfall and specific humidity), we multiplied the climatology with a ratio between the original output and the mean

$$X_{new}(t) = \bar{C}_{core} \times (X_{ori}(t)/\bar{C}_{1970-1999}) \tag{5.2}$$

We applied the the runoff and vector fields (u- and vr- wind) without any modification. The basic idea of this pre-processing is to simulate the responses of the sea ice and ocean to the variations in HadCM3 atmospheric output.

Another parallel inter-annual simulation using the CORE2 inter-annual reanalysis forcing data is conducted to validate the model configuration by comparing the output with the observations. Observed ice concentration from the Canadian Ice Service Digital Archive (CISDA) is used to evaluate the simulated seasonal and inter-annual variabilities.

5.3 Results

In this section, first we demonstrate how well the model can reproduce the ice fields responding to the atmospheric forcing. We then examine the differences in ice concentration and thickness between the simulations using CORE2 and

HadCM3 forcing, respectively. Then we will focus on the sea ice condition variations in future time slices (2006–2025, 2026–2045, 2046–2065, 2066–2085) compared to 1986–2005. The changes in ocean surface properties will also be presented.

5.3.1 Model configuration validation

Due to the biases in forcing data, it is not proper to validate the model configuration by directly comparing the observations and model output using the HadCM3 forcing even with the "patch" mentioned in previous section. It is also known that there are issues in producing observation-like ice fields (concentration, thickness and circulation) in global climate models (*Kwok*, 2011). Thus the outputs from a parallel inter-annual simulation using the CORE2 forcing are used first in this section.

Generally, reasonable ice fields are simulated by the model in the CAA region. The simulated seasonal cycle of ice concentration agrees the CISDA data, with an ice concentration close to 1 during the cold-season (December, January–April) and a minimum ice concentration of ~ 0.4 in September (figure 5.2, upper), although the model concentrations are lower in the warm-season by ~ 0.17 on average. Largest differences occur in July and October, indicating fast melting and slow freeze-up respectively. Ice thickness responds to the atmospheric forcing with a time lag of one to two months, resulting in a seasonal cycle with a maximum of $\sim 2.28\,m$ in May and a minimum of $\sim 1.27\,m$ in October (figure 5.2, lower).

In space, during the cold-season, ice covers all the northern CAA, the CAA channels (including Nares Strait) and Baffin Bay almost completely southward to Davis Strait except near the west coast of Greenland (figure 5.3, upper left). The spatial pattern is in agreement with the observations (*CIS*, 2002), although the land-fast ice, e.g., along the northeastern Baffin Bay, is not captured. Thicker sea ice of $3 - 4\,m$ is located along the northern coast of the CAA and Greenland, which is consistent with previous studies (e.g., *Bourke*

and Garrett, 1987) although thinner. Within the QEI, simulated ice thickness is close to the late winter average value, $3.4\,m$, estimated by *Melling* (2002) using drill hole measurements in the 1970s. The decline of ice thickness from the northwestern to southeastern Sverdrup Basin (QEI) noticed by *Melling* (2002) is also produced by the model, indicating a reasonable transition of sea ice from the Arctic coast to the central CAA. Within the Parry Channel, a positive eastward gradient is found in ice thickness, with thicker ice on the Arctic Ocean side and thinner ice on the Baffin Bay side with some thick ice adjacent to the M'Clintock Channel (figure 5.3, upper right). Within Baffin Bay, ice is generally thicker on the west side.

During the warm-season, a north-south pattern separated by the Parry Channel is clearly shown both in the concentration and thickness, with high concentration and thick sea ice in the north (including the QEI) and low concentration and thin sea ice in the south (figure 5.4, upper left), with M'Clintock Channel as an exception. Ice thickness within the QEI becomes thicker along the path towards the central CAA, which is due to the influx of multi-year sea ice from the north. In the central CAA, sea ice with high concentration is found in the western half of Parry Channel, especially to the south, and M'Clintock Channel (figure 5.4, upper right), which is in agreement with the observations (*CIS*, 2002). Such an along-channel spatial pattern is not obvious in the thickness field (figure 5.4, upper right). Sea ice in Jones Sound does not melt as much as observations (*CIS*, 2002). The eastern half of Baffin Bay is nearly ice free while some ice with a concentration of < 0.5 and thickness $< 1\,m$ is confined to the west coast (figure 5.4, upper).

As the CAA is covered by sea ice during most of each year, the inter-annual variation of the ice fields during the warm-season (July–October) is most interesting. With the CORE2 forcing, the inter-annual variation of the warm-season ice concentration within the CAA is also reasonably reproduced compared to the CISDA data (figure 5.5). Again, the simulated concentrations are generally lower, which is caused by faster melting in the model from May

to July (figure 5.2, upper), which was also noticed by *Sou and Flato* (2009). Overall, the model successfully captures the high (e.g., in 1986 and 2004) and low (e.g., in 1998 and 2007) ice events in the past (figure 5.5) with a correlation coefficient of 0.68.

Compared to the simulation using CORE2 forcing, the simulation with HadCM3 forcing produces a similar seasonal cycle of concentration (figure 5.2, upper) and thickness (figure 5.2, lower) but with much lower ice concentration in summer and $\sim 0.2\,m$ thinner on average throughout the year. Both the ice concentration and thickness reach the minimum at nearly the same time, August to September, without the time lag noticed with the CORE2 forcing. The large scale spatial pattern of the sea ice fields in this simulation are similar to those using CORE2 forcing (figure 5.3 and 5.4). But the thick ice in HadCM3 covers a much larger area to the north of the CAA, extending into the central Arctic Ocean, all the year round. The ice is much thinner in the southern parts, with an almost ice-free Baffin Bay in the warm-season. There is no regional thick or high concentration sea ice found in the M'Clintock Channel. Therefore the results in the following sections need to be considered with caution as an earlier ice-free CAA could be simulated when using HadCM3 forcing fields.

5.3.2 Sea ice conditions in future periods

5.3.2.1 Trends of sea ice in the CAA

As expected, in the context of a warmer climate, ice in the CAA declines in all seasons (winter: January–March; spring: April–June; summer: July–September; autumn: October–December) both in concentration (figure 5.6, upper) and thickness (figure 5.6, lower). Ice concentration reduces least in winter, with only negligible reductions close to the end of our simulation. In summer and autumn, a rapid decrease is found from the beginning of the 2030s to the end of the 2040s. During 2026–2065, the ice concentration decreases by

~ 0.29 in summer (65%) and autumn (38%). With this simulation, it shows that even in summer, the CAA could be completely ice free only by the end of the 21st century.

Compared to ice concentration, thinning of ice is notable in all four seasons (figure 5.6, lower). During 2026–2065, on average, there is a reduction of $\sim 0.22\,m$ per decade in the annual mean from $1.68\,m$. The net reductions are similar in all four seasons, but weight differently from the initial values, e.g., in summer, $0.25\,m$ per decade from $1.33\,m$ leads to a thinning of $\sim 75\%$ while only 49% in spring from $2.05\,m$. By the end of this simulation, the seasonal sea ice still reaches a thickness of $\sim 1\,m$ in winter and spring.

5.3.2.2 Changes in sea ice spatial pattern

In winter, visible ice concentration change is only found in Amundsen Gulf and Baffin Bay (figure 5.7). Ice thickness reduces more significantly in the Arctic Ocean where the multi-year ice is located, especially during 2046–2065 and 2066–2085 (figure 5.8). Reduction of ice thickness in the central CAA and Baffin Baffin is very small during 2006–2025 and 2026–2045. At the same time ice thickness increased by $\sim 0.5\,m$ regionally within the QEI (figure 5.8, upper), which may be caused by the motion of multi-year sea ice inflowing from the north. This gain is lost later during 2046–2065 (figure 5.8, lower left). Most ice within Parry Channel and M'Clintock Channel starts thinning in 2046–2066.

In summer, the changes are more dramatic compared to the winter case (figure 5.9 and figure 5.10). The west part of the NWP, from Amundsen Gulf to Queen Maud Gulf, is open in all four time periods. That the route through Peel Sound will be the earliest accessible route, *Howell et al.* (2008) mentioned, is also supported by our simulation. The east part of the NWP, from Victoria Strait to Peel Sound and Lancaster Sound, opens in the last two time periods, 2046–2065 and 2066–2085. In 2006–2025 and 2026–2045, the Parry Channel is still covered by sea ice with a concentration of ~ 0.5, especially in the Viscount

Melville Sound region prior to 2026. Compared to the sea ice in 1986–2005, ice in the center region close to Barrow Strait actually increases in thickness by $\sim 1.0\,m$ (see section 5.3.2.3 for details), which delays the opening of the whole Parry Channel in 2046–2066 (figure 5.9 and 5.10, lower left). Pronounced retreat and thinning of sea ice is found in the northern part of the CAA (QEI and northern coast) and interior of the Arctic Ocean in 2046–2065 and 2066–2085. The thick multi-year ice pack, located to the north of the CAA, has a thickness of $\sim 2\,m$ and concentration of ~ 0.8 in 2046–2065, $\sim 1.5\,m$ and ~ 0.7 in 2066–2085. Because Baffin Bay is ice free during summer, no change is observed in those figures.

5.3.2.3 Changes in sea ice at select sites

In this section, ten sites (see figure 3.1) are selected to represent the NWP (Amundsen Gulf, Cambridge Bay, Victoria Strait, M'Clure Strait, Barrow Strait), and its upstream (Beaufort Sea) and downstream ends (Baffin Bay, Davis Strait, northern Labrador Shelf and central Labrador Sea). The location of each site is given in table 5.1. The annual mean ice concentration and thickness at each site are summarized in table 5.2 and 5.3. And their inter-annual variations in different seasons are presented in figure 5.11 and 5.12.

The Beaufort Sea is the region where the Arctic Ocean experiences great changes in sea ice. While the annual mean ice concentration is relatively stable, with a value of > 0.95 (table 5.2), ice thickness shows a decreasing trend (table 5.3) with large inter-annual variations before the 2030s. Ice concentration in summer and autumn drops abruptly at the end of 2070s (figure 5.11d), e.g., for the summer case, from > 0.8 to ~ 0.2 within 10 years. Ice thickness evolves similarly in all four seasons (figure 5.12d), and significant thinning is found after the 2030s, which is much earlier than the case for concentration. By the 2050s, a thickness of $\sim 2m$, which is only half of the value at the beginning of the 21 century, is simulated.

In Amundsen Gulf and Cambridge Bay, basically, there is only seasonal ice

during the model integration (figure 5.11a), with an annual mean concentration of ~ 0.5 and thickness of $\sim 0.5\,m$ since the beginning of this century (table 5.2 and 5.3). The NWP though Peel Sound is blocked by relatively thicker sea ice in Victoria Strait, with a mean concentration of > 0.5 and thickness of $> 0.8\,m$ before 2050 (table 5.2 and 5.3). In summer, it may be ice free from 2050 but this is not likely to happen in other seasons (figure 5.11).

M'Clure Strait, the gate of another NWP route, is covered by even higher concentration (> 0.6) and thicker ($> 0.9m$) ice compared to that in Victoria Strait before 2050. With a value of > 0.8 in all four seasons at the beginning of integration, the ice concentration decreases much faster in summer, reaching as low as 0.1 around 2020 while there are decreases of only 25% and 50% in spring and fall respectively by 2050. However, the summer ice concentration rebounds back (although still less than 0.5) with large inter-annual variability over the next 20 years, and then is almost ice-free for the rest of the model integration. Summer and autumn ice thickness decreases by $\sim 50\%$ by the beginning of the 2020s. It then takes about another 30 years for the winter and spring ice to decay.

In Barrow Strait, the change in sea ice is quite different (figure 5.11 and 5.12, f). Instead of a decreasing trend, there is an abrupt increase in both ice concentration and thickness from 2008 to 2046. However, there is no cooling signal in the atmospheric forcing, which indicates these changes are caused by accumulation due to ice advection.

Downstream of the CAA, seasonal ice forms in Baffin Bay, Davis Strait and on the Labrador Shelf (figure 5.11 and 5.12, g–i). There is no ice in the central Labrador Sea all the year round (figure 5.11 and 5.12, j). In central Baffin Bay, both the concentration and thickness show little variation in their annual means. A decrease of ~ 0.1 in spring and autumn concentration and 0.2–$0.3\,m$ in fall, winter and spring thickness occur around the end of the 2040s. In Davis Strait, even in the autumn, there is very low concentration (< 0.2) of thin ($< 0.2\,m$) ice before 2046. The northern Labrador Shelf is similar, almost

being ice-free both in the autumn and summer, particularly after the 2040s. A reduction of $\sim 50\%$ in winter and spring concentration and thickness occurs in the 2040s. Large inter-annual variations are found in winter and spring sea ice in Davis Strait and on the northern Labrador Shelf.

5.3.3 Ocean surface conditions in the future periods

5.3.3.1 Trends of SST and SSS within the CAA

Within the CAA, SST shows a pronounced increase in summer and autumn in the 2040s and onward (figure 5.13, upper). During the 2040s, the surface ocean warms from $\sim 0^\circ$ to $\sim 2^\circ C$, which corresponds to both the increase of surface air temperature and the decrease of ice coverage at the same time. During the same time, although not as noticeable, SST increases by $0.6^\circ C$ in autumn. As most areas of the CAA is covered by sea ice in winter and spring, there is only a slight increase (less than $0.4^\circ C$ in total) in SST, which is otherwise close to the sea water freezing point, in the later half of integration.

However, the simulated SSS does not indicate any trend over the whole integration in all seasons within the CAA (figure 5.13, lower). The SSS field demonstrates a Strong seasonal cycle with a range of 1 salinity unit, with lower salinity in summer due to ice melting and higher salinity in winter and spring caused by ice formation. A decadal oscillation with a period of $\sim$ 40-year exists in the SSS field, with high SSS at the beginning of the 2000s, 2050s and 2090s. The fluctuations reflect the combination of the change in upstream (inflow of fresher polar water), downstream (intrusion of saltier water from Baffin Bay), and the other local freshwater fluxes (e.g., precipitation, runoff, net ice formation and melting).

5.3.3.2 Changes in SST and SSS spatial patterns

In winter, local melting of sea ice (figure 5.7) leads to a lower SST along the west Greenland coast up to the southern end of Nares Strait, especially the

region close to the eastern part of Davis Strait (figure 5.14). The central Arctic Ocean and most the CAA waters still are close to the seawater freezing point because of the existence of ice cover during 2005–2025 and 2026–2045. In winter, the Beaufort Sea and Amundsen Gulf have the most significant warming in our simulation, locally as high as $\sim 0.1°C$ during 2046–2065 and $\sim 0.2°C$ during 2066–2068, compared to 1986–2005. At the same time, surface freshening by > 0.75 is first seen in Baffin Bay coastal and adjacent regions (west Greenland coast, Nares Strait, Jones Sound and eastern part of QEI) during 2006–2025. This freshening extends to the northern coast of the CAA during 2026–2045. Later freshening is also found in the central Arctic Ocean, particularly the Beaufort Gyre during 2066–2085 (figure 5.16). The freshening demonstrates a north-south pattern in space. In Baffin Bay, there is no freshening signal along the eastern coast of Baffin Island where the southward flow carries a mix of cold fresh water southward. Within the CAA, freshening mainly occurs in the waters north to Parry Channel.

In summer, without the heat loss due to ice melting, the warming of the sea surface is much more significant (figure 5.15). The warming is first seen in the southern Beaufort Sea and Amundsen Gulf during 2006–2025, and then extends to the central Beaufort Sea reaching the mouth of M'Clure Strait during 2026–2045. The amplitude increases at the same time. Later the western parts of Parry Channel, M'Clintock Channel, Baffin inlets (Prince Regent Inlet and Gulf of Boothia) as well as the eastern coast of Baffin Island warm during 2045–2065 and 2066–2085. The freshening in summer has a similar north-south pattern to that in winter but is slightly larger in amplitude, particularly in the the central Arctic Ocean (figure 5.17). Another difference is that in ice-free regions, e.g., southern Beaufort Sea and Amundsen Gulf and M'Clintock Channel, the SSS increases because of the lack of ice melt. This spatial variation in the trend of SSS also explains why there is no monotonic decrease in SSS over the whole CAA region. In addition, cooling in the central and eastern Parry Channel during 2006–2025 and 2026–2045 indicates more

ice melting occurring there.

5.3.3.3 Changes in SST and SSS at select sites

As mentioned in the previous section, the trends of ocean surface variables, especially SSS, vary in space. In terms of annual mean, the ocean surface warms up at all the ten selected sites by 2066–2085 (table 5.4), increasing by as much as $2.38^\circ C$ in the central Labrador Sea and as little as $0.15^\circ C$ in the Beaufort Sea. The trends of SSS at the ten sites are quite different (table 5.5). Without considering other freshwater sources, the changes of sea ice can partly explain the evolution of SSS at most locations. In winter, less ice forms locally, indicating less brine ejected into the ocean and lower SSS. In summer, more ice melts locally, signaling more freshwater flux into the ocean and again lower SSS. Table 5.4 and 5.5 present the annual mean SST and SSS at each site. And figure 5.18 and 5.19 show their inter-annual variations during the different seasons.

In the Beaufort Sea, as the ocean is covered by sea ice most of the year, heat absorbed by the ocean is used to melt the ice on top. Thus, the SST does not change much in any season until the sea ice disappears in summer and autumn around 2080 (figure 5.18, d). For the annual mean, there is an increase of $0.15\,^\circ C$ by 2066–2085 (table 5.4). Over the integration, there is a decrease in SSS in all four seasons, with strong freshening of ~ 1 (comparable to the range of its seasonal cycle) during 2014–2026 and a weaker drop of ~ 0.5 at the end of the 2060s (figure 5.19).

Due to an earlier melting of the seasonal ice cover in spring, the summer SST increases significantly in Amundsen Gulf (figure 5.18, a), reaching a value as high as $\sim 6^\circ C$ at the end of the 2040s from $\sim 3^\circ C$ at the beginning of the 2000s. SST also increases in spring and autumn but at a much slower rate. Similarly, in Cambridge Bay, there is also an increase in SST ($\sim 2^\circ C$) in summer caused by earlier melting. This occurs over a much shorter time period, from the middle of the 2030s to the end of the 2050s (figure 5.18, b). In

Victoria Strait, the increased summer SST is explained by the disappearance of summer ice cover there in the 2040s. Less ice formation and melting in the local areas can explain the smaller range of SSS seasonal cycle and large scale freshening events (e.g., figure 5.19c). However, other sources of freshwater input or changing of circulation need be considered to explain complex SSS trends, e.g., SSS increasing in Amundsen Gulf from the end of 1980s to the 2050s (figure 5.19, a).

Evolution of the SST and SSS in M'Clure Strait are similar to Victoria Strait (figure 5.18 and 5.19, e). The shift of multi-year ice to seasonal ice leads to a jump of $> 2°C$ in SST in the 2040s. A temperature drop around 2080s corresponds to a sudden increase of sea ice in spring at that time. The ocean freshens by ~ 0.5 from the beginning of the 2000s to the end of the 2010s in all four seasons, then is a relative stable state until the middle of the 2040s, except in summer. After 2050, SSS experiences a strong decadal "oscillation" from $\sim$ 29 to $\sim$ 31.5, with a low around 2080, highs around 2050 and the middle of the 2090s.

In Barrow Strait, because of the existence of sea ice all the year round from the end of the 2010s to the middle of the 2040s, SST is close to the freezing point in all seasons (figure 5.18, f). After that the SST increases quickly in the 2050s, reaching $\sim 2°C$ in summer. Another warming trend is seen at the end of the model integration. A rapid freshening at the end of the 2010s, especially in winter and summer, supports the explanation that the increased sea ice is not locally formed (figure 5.19, f). SSS reaches high values again in the 2050s, 2070s and 2090s, resulting in no significant long-term freshening.

Downstream of the CAA, there is a clear warming signal in central Baffin Bay, Davis Strait and the northern Labrador Shelf (figure 5.18, g-i). This increased SST is mainly limited to warming from the middle of the 2020s to the middle of the 2040s, in summer. In Davis Strait and on the Labrador Shelf, there is also warming in autumn and spring at the same time. In central Baffin Bay, the ocean surface basically freshens by ~ 0.8 after the 1990s through to

the 2040s. In Davis Strait, the range of the SSS seasonal cycle is much smaller after 2000, suggesting very little local ice formation or melting occurring there although seasonal ice does exist (figure 5.19, h). The freshening after the 2000s is possibly associated with the switch in atmospheric forcing data. On the northern Labrador Shelf, there is no noticeable long-term trend in SSS, in any seasons, although the region freshens by ~ 0.5 in the 2020s (figure 5.19, i).

In the central Labrador Sea, since there is no ice even today, the ocean surface experiences similar SST evolutions in all seasons with a small range SSS seasonal cycle (figure 5.18). The ocean warms slowly but nearly steadily over the model integration, with an average increase of $> 2°C$ by 2100. The SSS reaches its highest values around the middle of the 2010s, and then shows large inter-annual variations around 33.8 through to the end of the simulation.

5.4 Summary and discussion

In this paper, the ice and sea surface conditions in the CAA and adjacent waters are simulated under the projected climate from the IPCC A1B scenario. Under a warmer climate, decreases in both ice concentration and thickness occur as expected. The rates vary in different time periods and with geographic locations. Although an ice-free CAA is not likely to happen until the end of the 21st century, our simulation indicates that the CAA region will experience fundamental changes in its sea ice regime during 2026–2065, concentration shrinking by ~ 0.29 and thinning by $\sim 0.25\,m$ per decade in summer. Compared to *Sou and Flato* (2009), our simulation shows a faster decline in both concentration (65% vs 46%) and thickness (75% vs 36%).

In addition, our simulation also produces much less ice in the Beaufort Sea and western Parry Channel compared to *Sou and Flato* (2009) after 2040 in summer, which suggests an earlier opening of the NWP through M'Clure Strait. Due to the ice occupying the waters between the Viscount Melville

Sound and Barrow Strait, also shown in results from *Sou and Flato* (2009), the earliest accessible route of NWP will be the eastern one, through Peel Sound, Victoria Strait, and Amundsen Gulf.

Lower albedo, due to lower concentration and thinner sea ice, leads to more heat absorption, and thus warms the ocean, especially in summer. Changes in SSS are complex. Within the CAA, we see an oscillation with a period of $\sim$ 40 years, with high SSS at the beginning of the 2000s, 2050s, 2090s. Although we can link some of the SSS changes to sea ice processes (formation and melting), other processes, such as direct warming due to the increased surface air temperature and freshening caused by more precipitation/runoff, are also important. In fact, these processes may be the main drivers at some locations with little or no sea ice cover.

Using recent satellite ice motion and concentration data, *Kwok* (2006) found a small net outflow of sea ice from the CAA to the Canada Basin through the western and northern gates (Amundsen Gulf, M'Clure Strait and QEI). This finding is dependent on the ice conditions at those gates. In the present day, the QEI is covered by fast ice most of the year and M'Clure Strait is covered by thick first year ice mixed with multi-year ice, which hinders the exchanges of sea ice between the CAA and the Arctic Ocean. However, in the future, once the ice gets more mobile, i.e in the QEI as well as Parry Channel, will the sign of the ice exchange change — an inflow of ice flux into the CAA? How long will it stay within the CAA and what potential impacts are there on the opening of NWP? These are interesting questions for future analysis.

Our simulation does show a reasonable mean state of ice and surface ocean conditions under a warmer climate, however, more simulations, with forcing data from different climate models, are required to estimate the range of variation and reach a robust conclusion. By comparing the outputs from global climate models, *Kwok* (2011) also found there are large differences between the simulated and observed ice motion, extent, thickness and export. In our study, the atmospheric forcing fields are rescaled based on the CORE2 cli-

matology, which helps to set up a seasonal cycle consistent with today, but how the biases in the forcings, e.g., downward longwave radiation incident at the surface (*Eisenman et al.*, 2007), are changed is still unclear. With these uncertainties, caution is needed in applying and using the current results.

5.5 Acknowledgements

This work has been supported by NSERC and Government of Canada International Polar Year awards to Paul G. Myers. We are grateful to Westgrid and Compute Canada for computational resources. We thank C. Boening and A. Biastoch for providing us model output that was used for model spin-up open boundary forcing. We thank the Canadian Centre for Climate Modelling and Analysis (CCCma) for the inter-annual open boundary forcing in our simulation. We also thank the Met Office Hadley Centre for making the HadCM3 output available.

site	longitude	latitude
Amundsen Gulf	$122.30°W$	$70.40°N$
Cambridge Bay	$106°W$	$69°N$
Victoria Strait	$99°W$	$70.5°N$
Beaufort Sea	$136°W$	$78°N$
M'Clure Strait	$123°W$	$75.2°N$
Barrow Strait	$95°W$	$74.35°N$
Baffin Bay	$65°W$	$72°N$
Davis Strait	$58°W$	$67°N$
north Labrador Shelf	$62°W$	$59°N$
central Labrador Sea	$51°W$	$57°N$

Table 5.1: Locations of select sites (average done over a neighbouring region of 5×5 model grid cells)

site	1986–2005	2006–2025	2026–2045	2046–2065	2066–2085
Amundsen Gulf	0.63	0.54	0.48	0.44	0.38
Cambridge Bay	0.55	0.52	0.50	0.45	0.44
Victoria Strait	0.76	0.77	0.67	0.53	0.52
Beaufort Sea	0.97	0.96	0.95	0.92	0.86
M'Clure Strait	0.86	0.76	0.63	0.50	0.49
Barrow Strait	0.55	0.75	0.78	0.61	0.56
Baffin Bay	0.56	0.56	0.53	0.48	0.48
Davis Strait	0.38	0.41	0.37	0.32	0.29
north Labrador Shelf	0.36	0.35	0.31	0.23	0.19
central Labrador Sea	0.00	0.00	0.00	0.00	0.00

Table 5.2: Annual mean ice concentration at the select sites (see figure 5.1 and table 5.1 for the locations) during different time periods

site	1986–2005	2006–2025	2026–2045	2046–2065	2066–2085
Amundsen Gulf	0.73	0.54	0.44	0.39	0.33
Cambridge Bay	0.59	0.55	0.52	0.43	0.43
Victoria Strait	1.03	0.99	0.82	0.52	0.51
Beaufort Sea	4.09	3.84	3.28	2.11	1.79
M'Clure Strait	1.49	1.22	0.92	0.56	0.63
Barrow Strait	0.91	1.20	1.16	0.69	0.57
Baffin Bay	0.52	0.52	0.50	0.38	0.40
Davis Strait	0.41	0.40	0.35	0.25	0.23
north Labrador Shelf	0.38	0.35	0.30	0.19	0.17
central Labrador Sea	0.00	0.00	0.00	0.00	0.00

Table 5.3: Same as table 5.2 but for ice thickness (unit: m)

site	1986–2005	2006–2025	2026–2045	2046–2065	2066–2085
Amundsen Gulf	-0.59	0.10	0.68	1.06	1.64
Cambridge Bay	0.21	0.46	0.53	1.16	1.34
Victoria Strait	-1.48	-1.44	-1.10	-0.09	-0.00
Beaufort Sea	-1.72	-1.71	-1.67	-1.66	-1.57
M'Clure Strait	-1.64	-1.53	-1.22	-0.41	-0.52
Barrow Strait	-1.02	-1.58	-1.59	-0.90	-0.62
Baffin Bay	-0.31	-0.41	-0.13	0.37	0.27
Davis Strait	0.68	1.23	1.62	2.18	2.41
north Labrador Shelf	1.14	1.29	1.70	2.65	2.81
central Labrador Sea	5.25	6.13	6.42	7.50	7.63

Table 5.4: Same as table 5.2 but for sea surface temperature (unit: $°C$)

site	1986–2005	2006–2025	2026–2045	2046–2065	2066–2085
Amundsen Gulf	30.45	30.46	30.68	30.84	30.74
Cambridge Bay	30.23	30.22	29.94	29.93	29.85
Victoria Strait	30.37	30.13	30.03	30.48	30.36
Beaufort Sea	31.63	31.39	30.55	30.46	29.90
M'Clure Strait	30.76	30.51	30.61	30.89	30.14
Barrow Strait	31.02	30.63	30.66	30.92	30.70
Baffin Bay	33.05	32.63	32.24	32.18	32.31
Davis Strait	32.82	32.19	31.77	31.77	32.07
north Labrador Shelf	31.91	31.77	31.71	31.75	31.90
central Labrador Sea	33.30	33.89	33.75	33.83	33.83

Table 5.5: Same as table 5.2 but for sea surface salinity

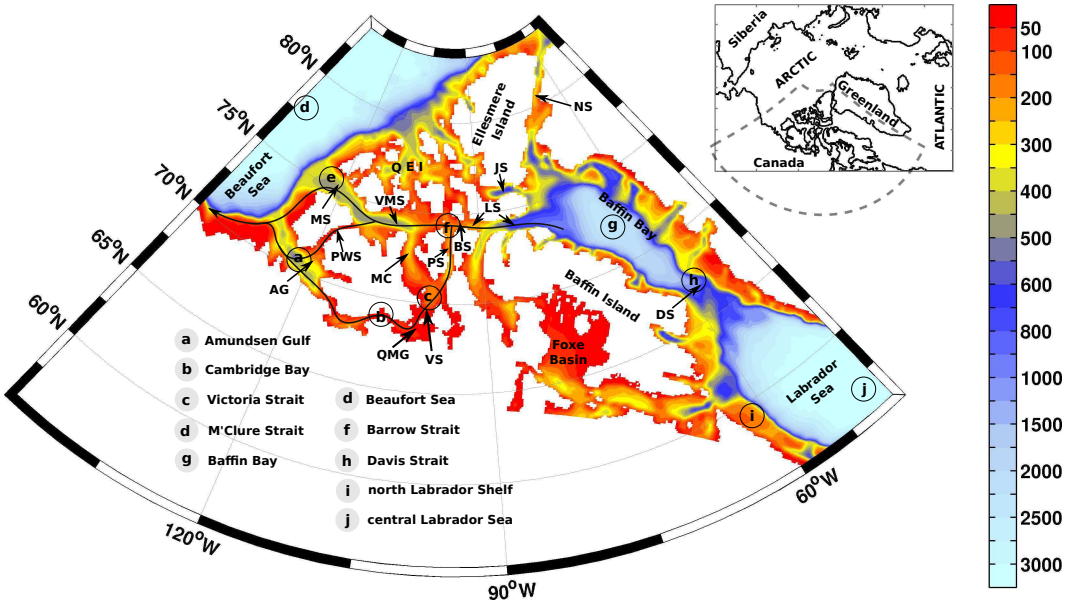

Figure 5.1: Map of the Canadian Arctic Archipelago (CAA) region. The dashed line in the box inset shows the CAA location (colors: water depth in meters; solid black curve: Northwest Passage; AG: Amundsen Gulf; QMG: Queen Maud Gulf; VS: Victoria Strait; MS: M'Clure Strait; PWS: Prince of Wales Strait; VMS: Viscount Melville Sound; MC: M'Clintock Channel; PS: Peel Sound; BS: Barrow Strait; LS: Lancaster Sound; DS: Davis Strait; QEI: Queen Elizabeth Islands; JS: Jones Sound; NS: Nares Strait)

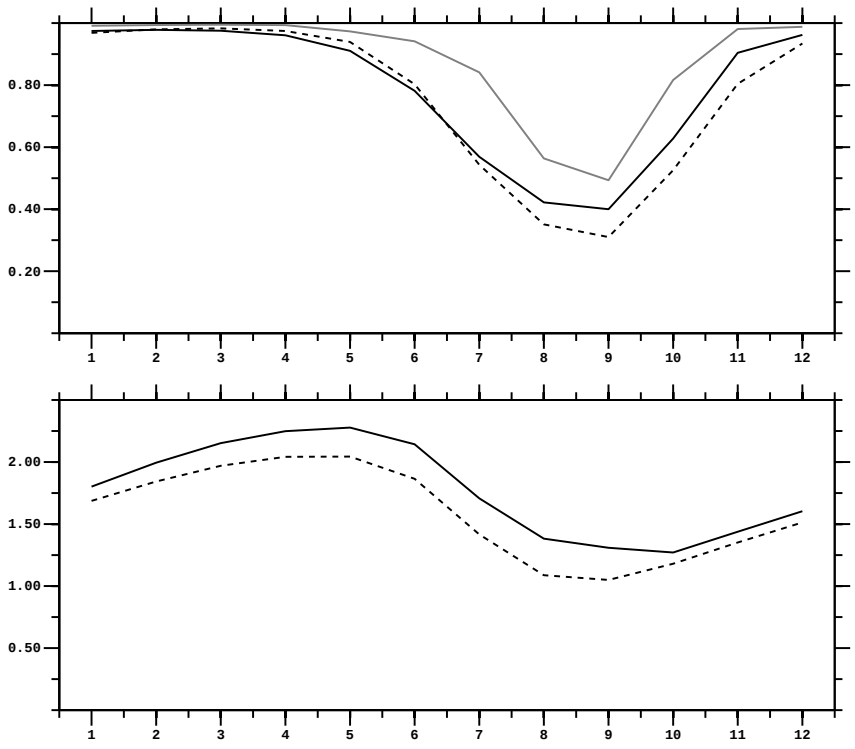

Figure 5.2: Seasonal cycle of the ice concentration (upper) and thickness (lower, unit: m) within the CAA (Nares Strait, Baffin Bay and Foxe Basin excluded) averaged over 1986–1999 (gray solid line: Canadian Ice Service Digit Archive data; black solid line: model simulation using CORE2 forcing; black dash line: model simulation using HadCM3 forcing). X–axis shows the time in month.

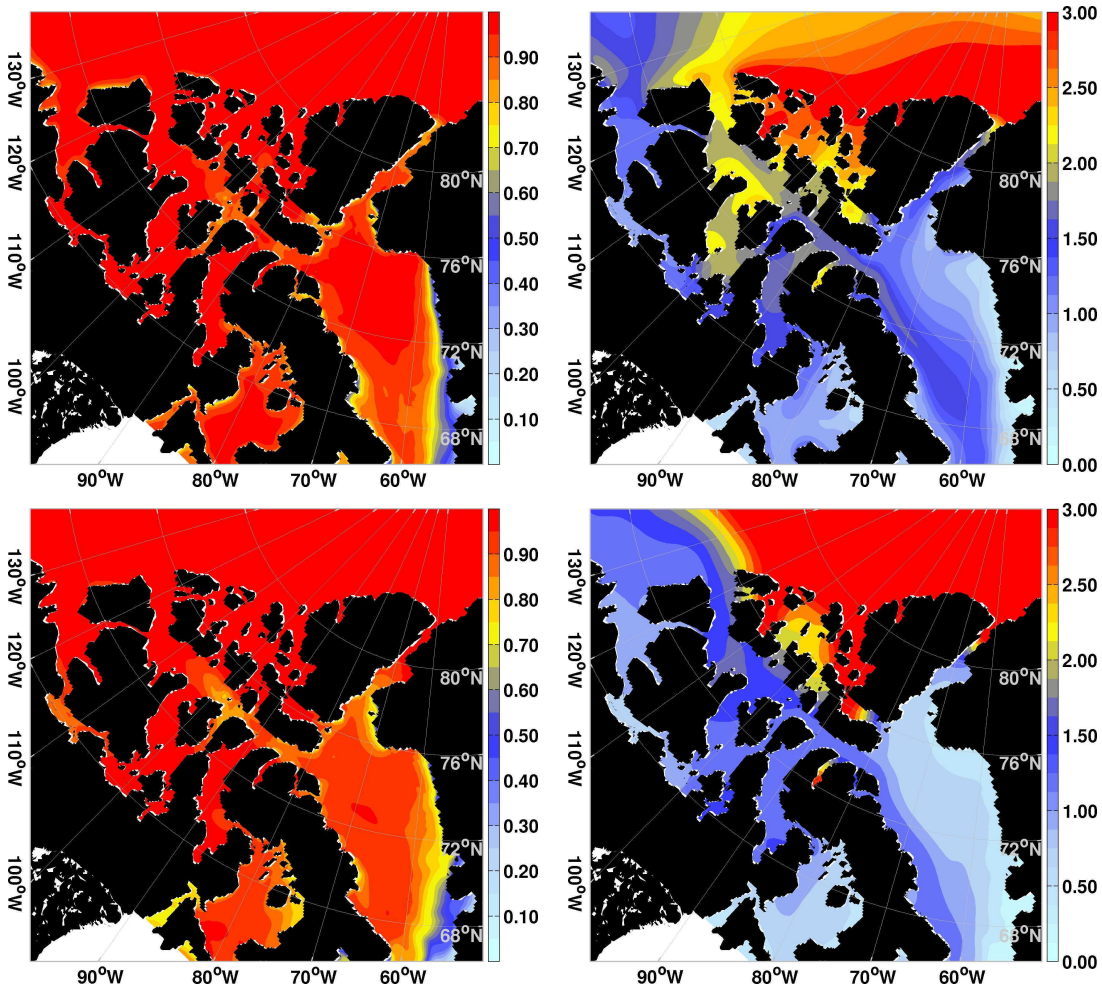

Figure 5.3: Simulated 1986–1999 cold–season (December, January–April) ice concentration (left) and thickness (right, unit: m) using CORE2 forcing (upper) and HadCM3 forcing (lower)

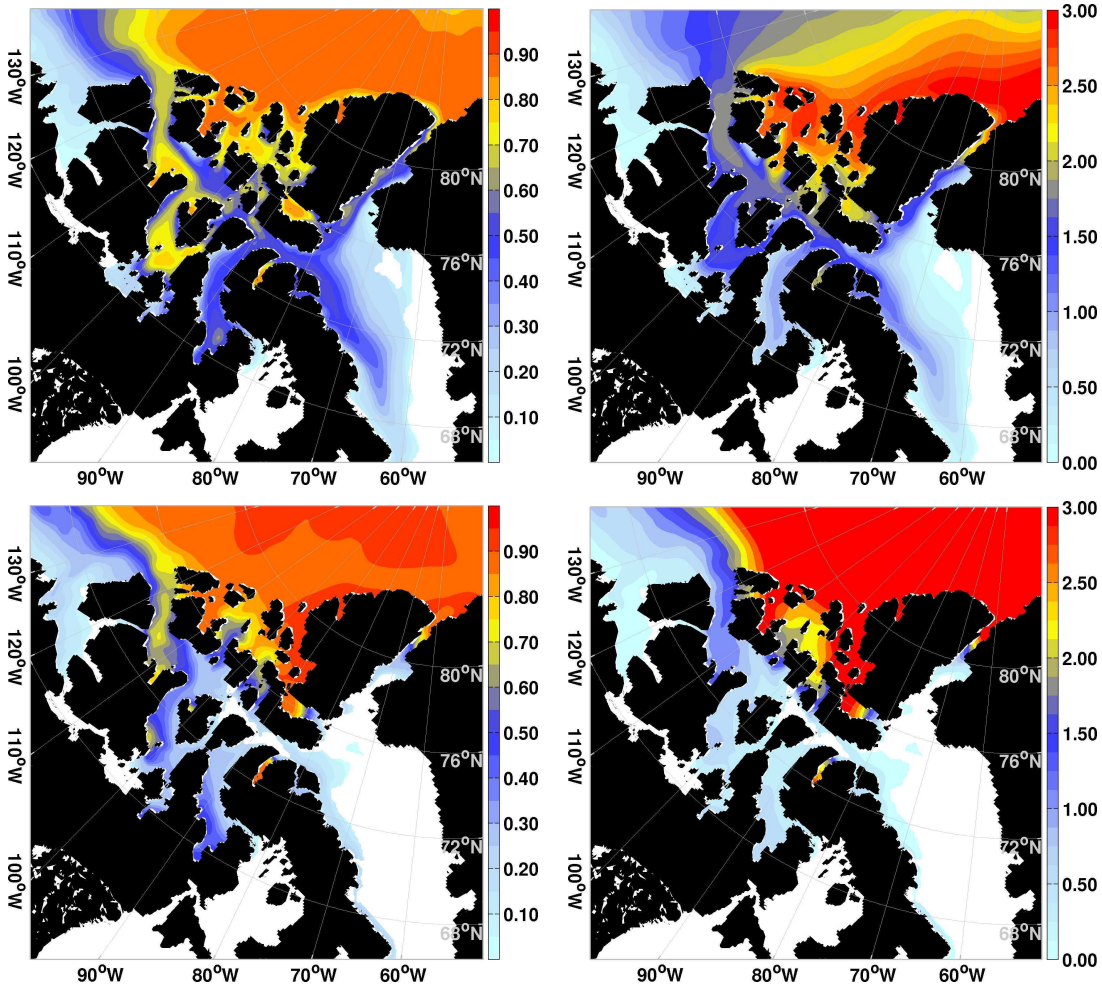

Figure 5.4: Same as figure 5.3 but for the warm–season (July to October)

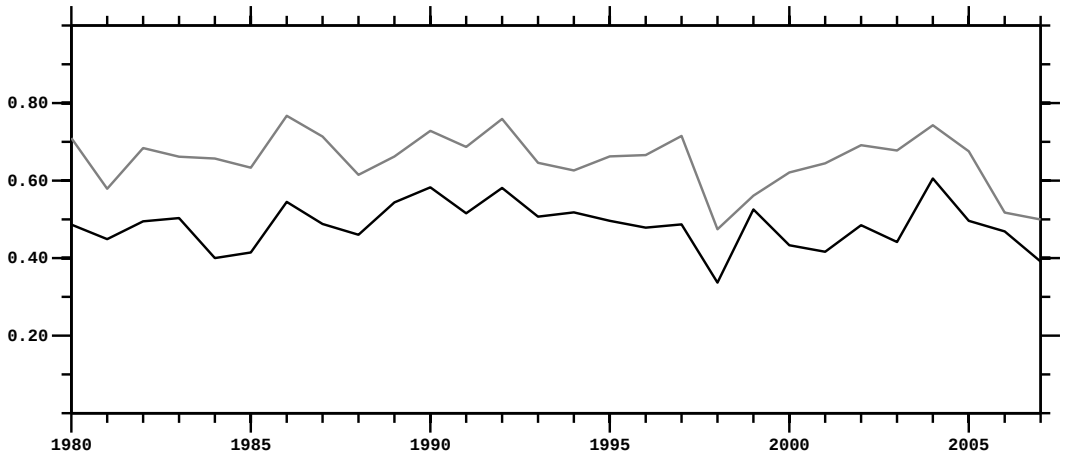

Figure 5.5: Inter-annual variability of the CAA (same as figure 5.2) warm–season ice concentration over 1980–2007 (gray solid line: Canadian Ice Service Digit Archive data; black solid line: model simulation using CORE2 forcing. X–axis shows the time in month.

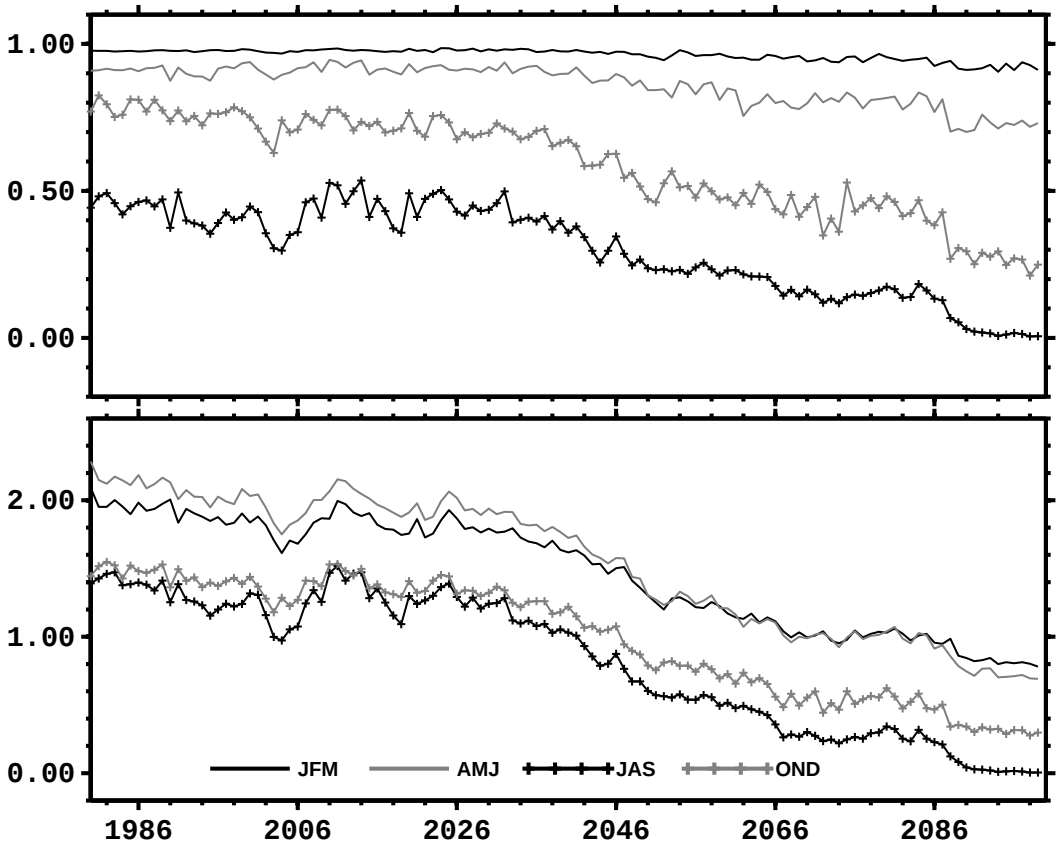

Figure 5.6: Simulated inter-annual variation of the averaged seasonal ice concentration (upper) and thickness (lower, unit: m) within the CAA (same as figure 5.2) over the time period 1980–2099 (solid black line: January–March; gray solid line: April–June; black line with plus marker: July–September; gray line with plus marker: October–December)

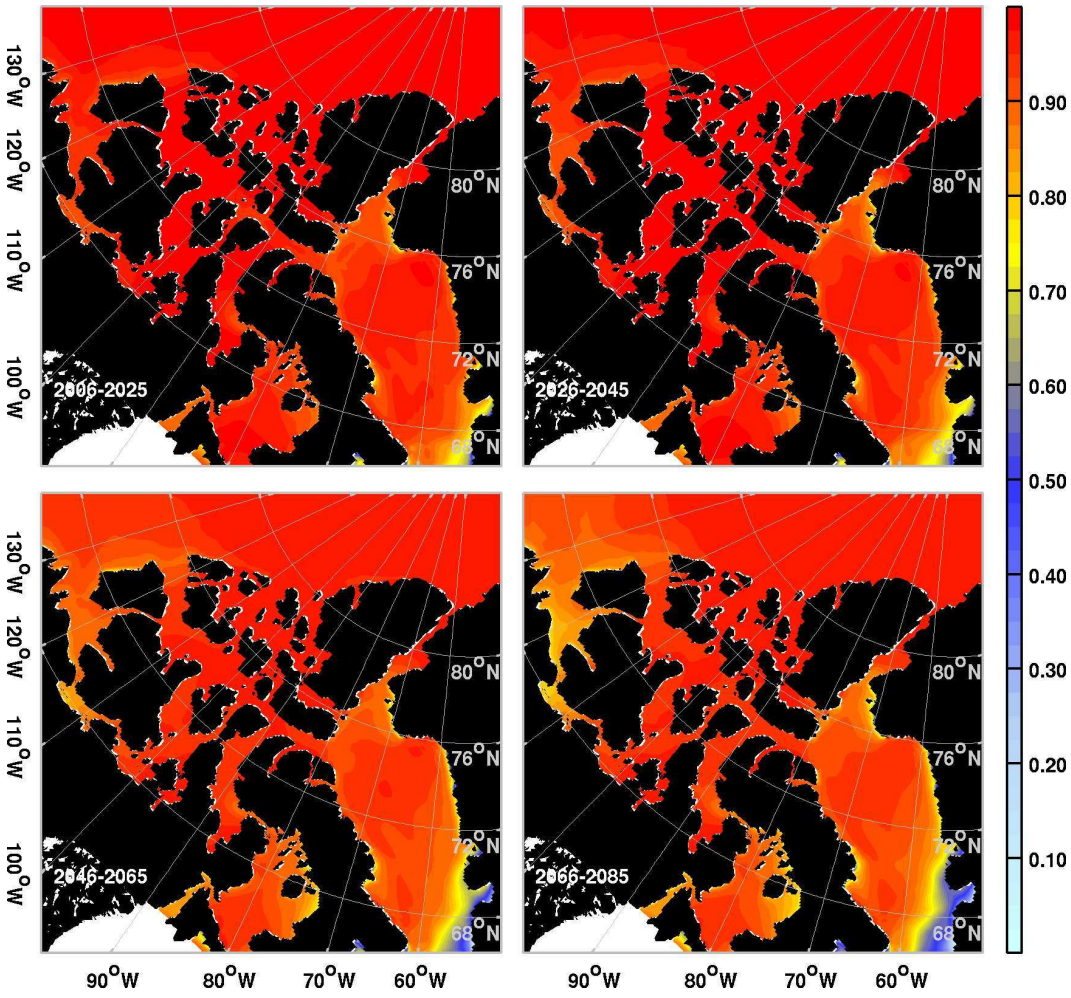

Figure 5.7: Winter (January–March) ice concentration in four time periods (upper left: 2006–2025; upper right: 2026–2045; lower left: 2046–2065; lower right: 2066–2085)

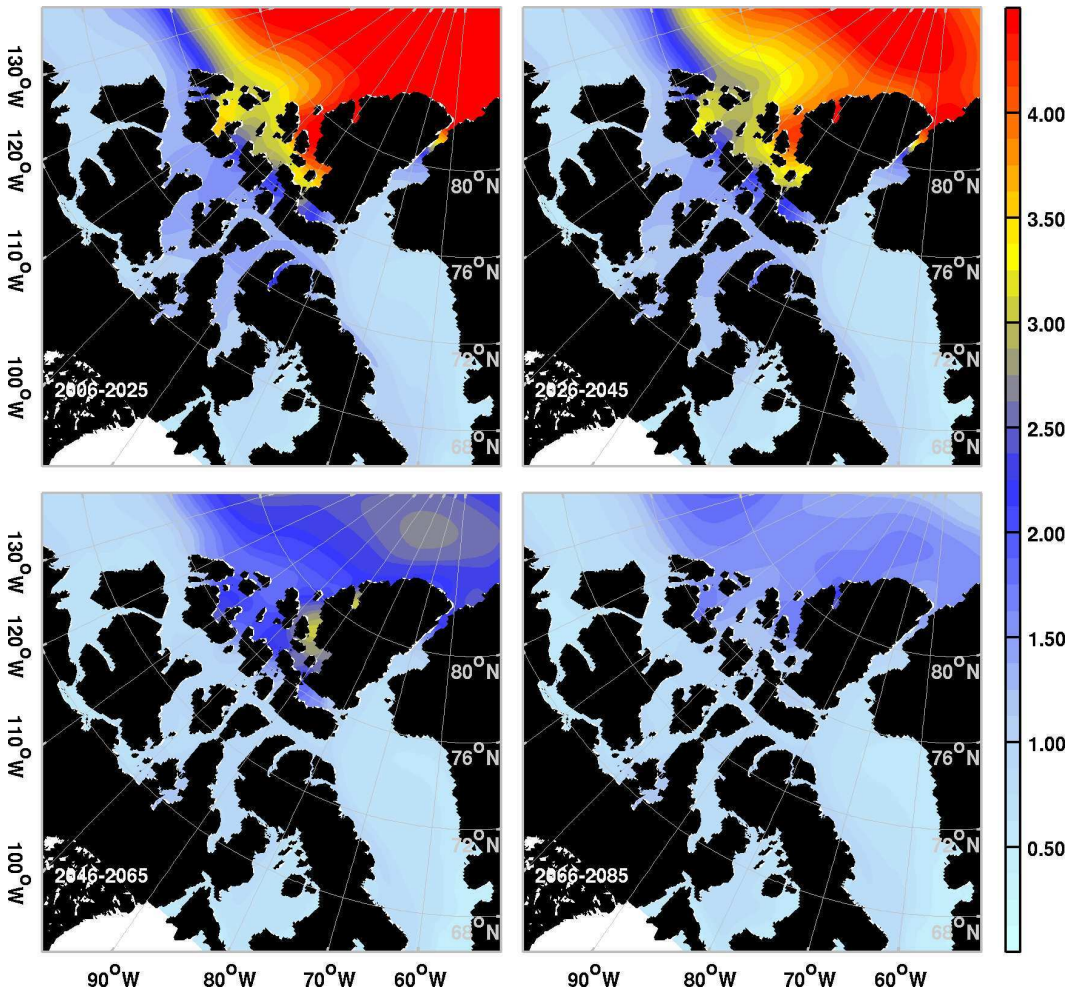

Figure 5.8: Winter (January–March) ice thickness (unit: m) in four time periods (upper left: 2006–2025; upper right: 2026–2045; lower left: 2046–2065; lower right: 2066–2085)

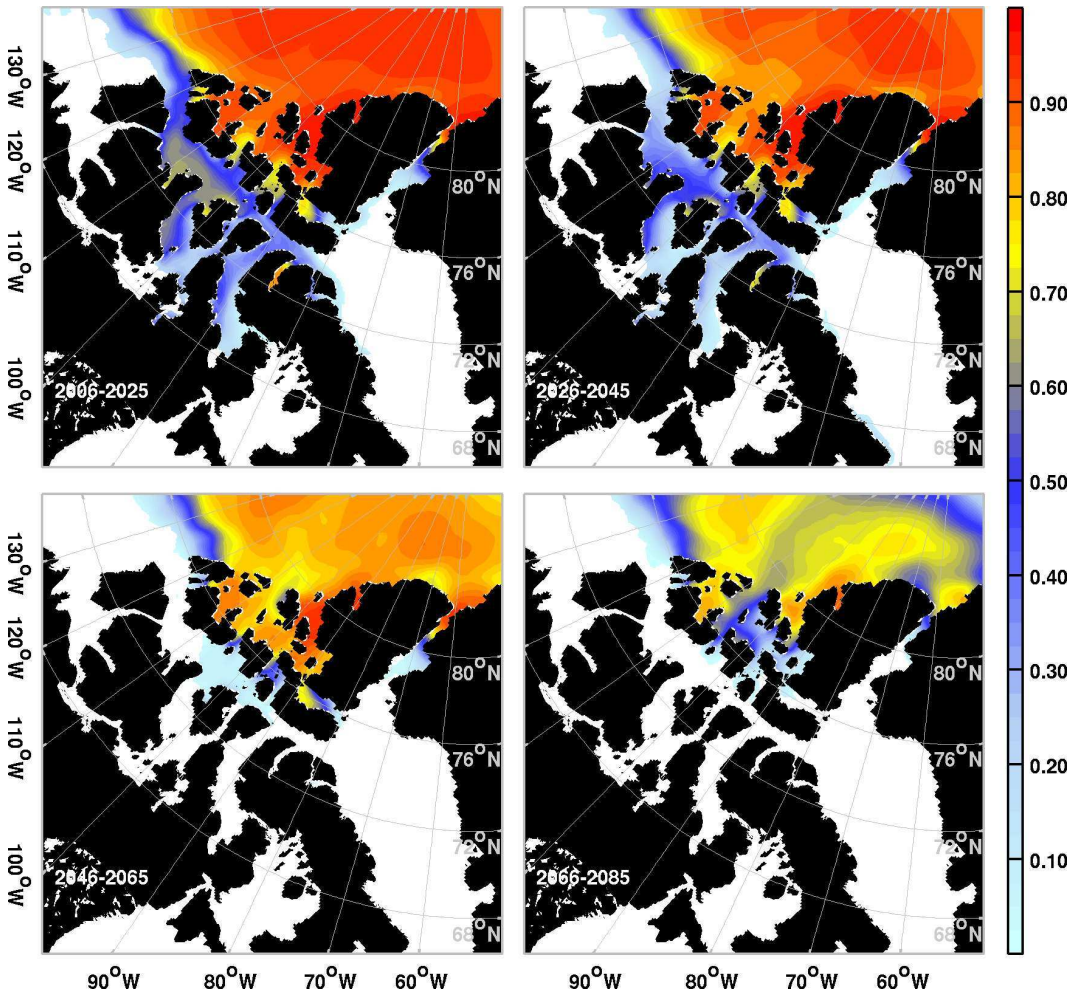

Figure 5.9: Same as figure 5.7 but for summer (July–September)

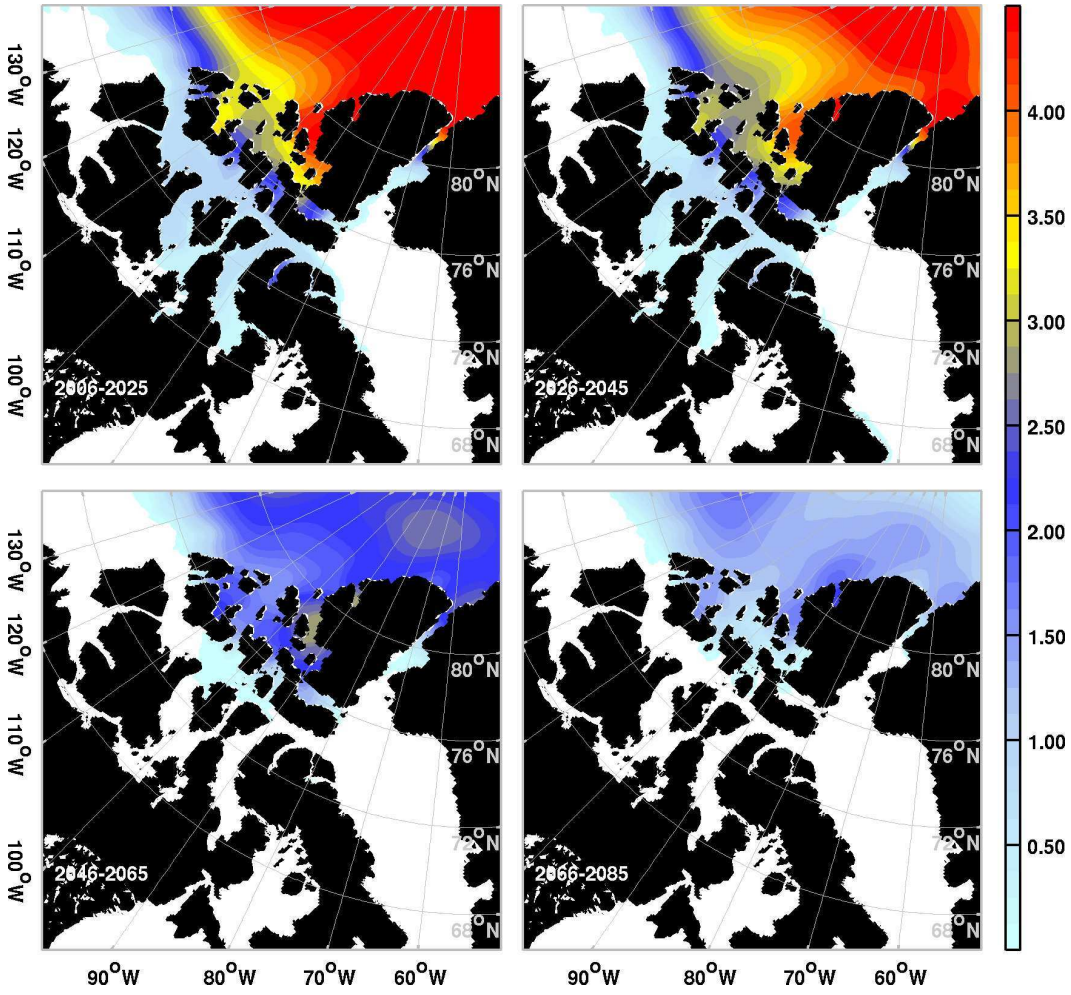

Figure 5.10: Same as figure 5.8 but for summer

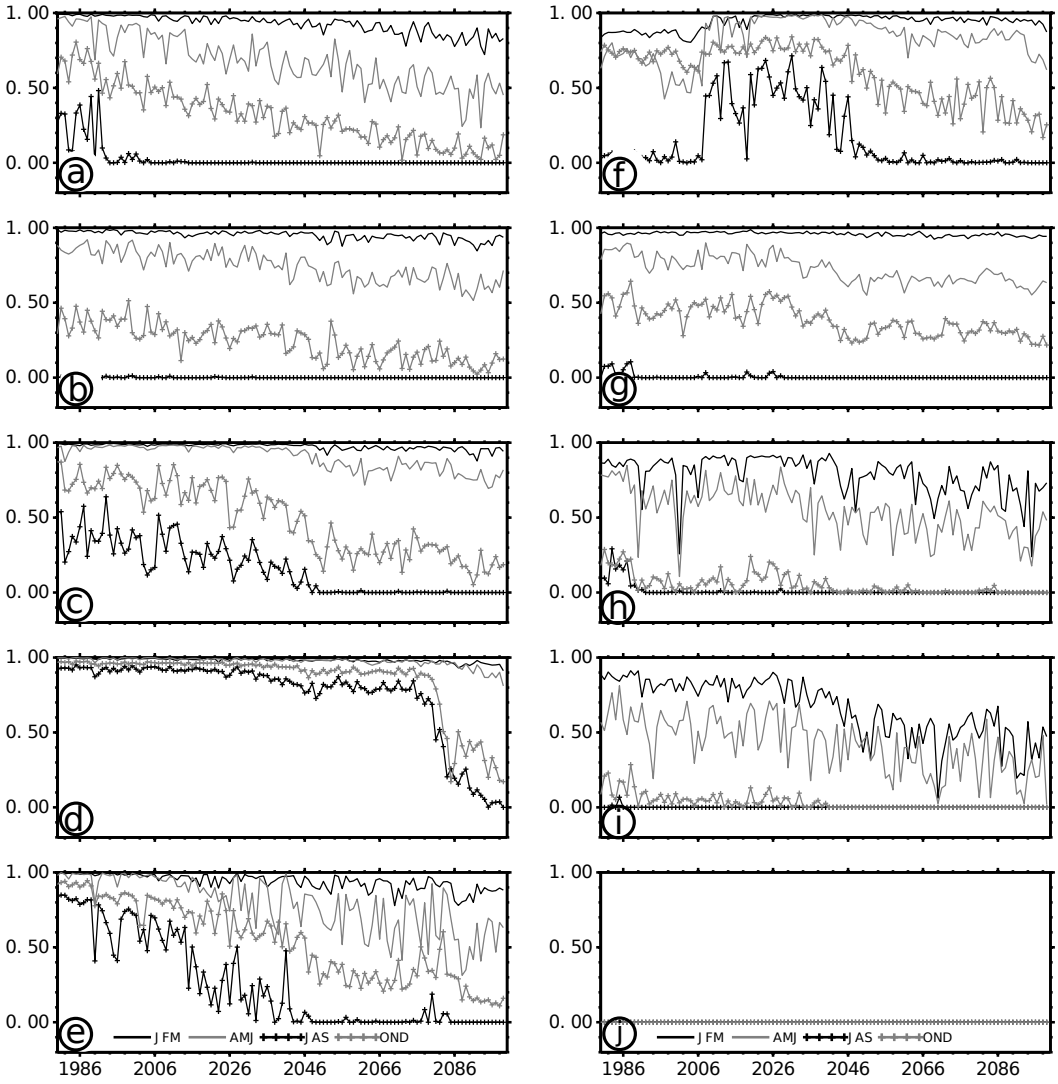

Figure 5.11: Simulated inter-annual variation of the averaged seasonal ice concentration at the select sites (locations are given in figure5.1 and table 5.1) over the time period 1980–2099 (solid black line: January–March; gray solid line: April–June; black line with plus marker: July–September; gray line with plus marker: October–December)

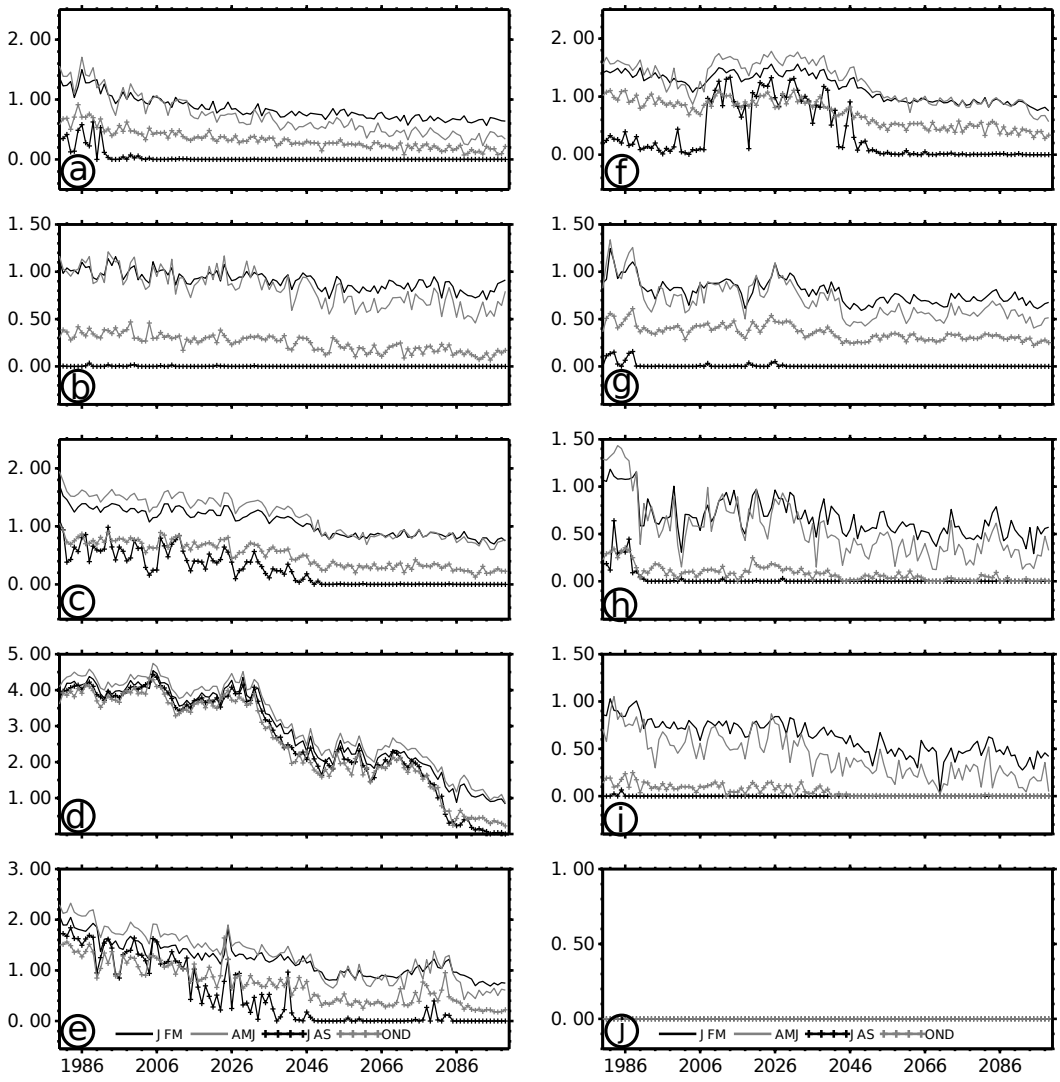

Figure 5.12: Same as figure 5.11 but for ice thickness (unit: m)

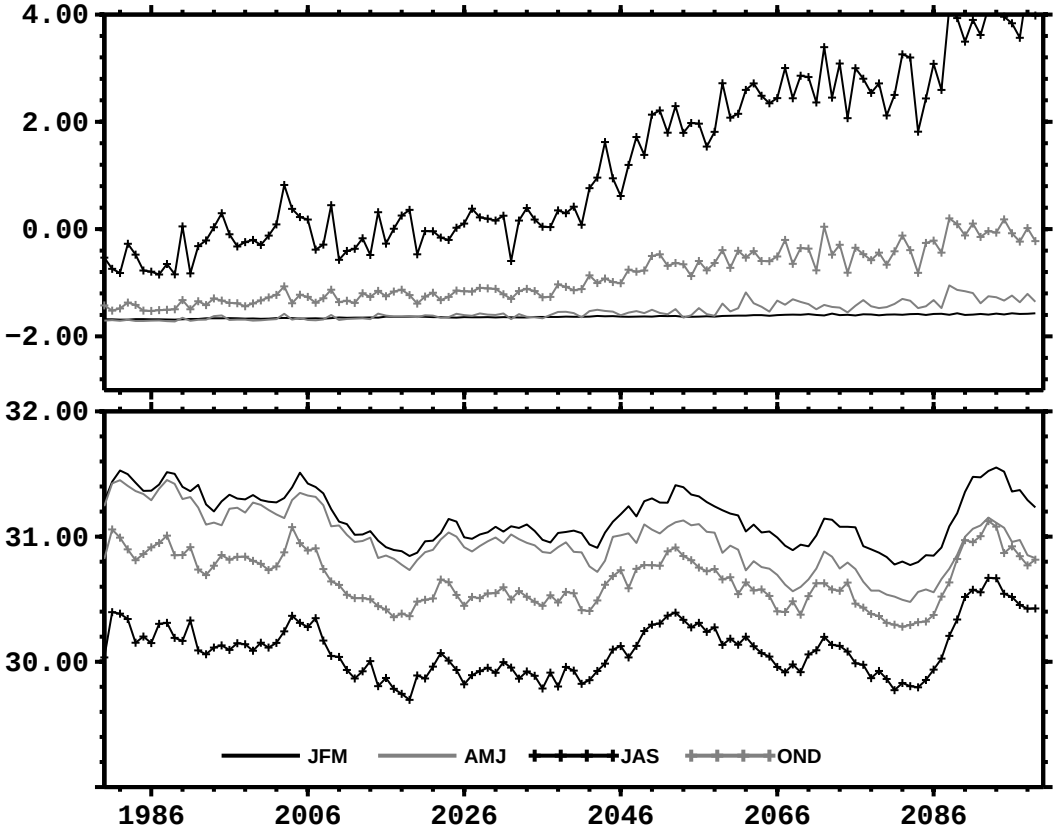

Figure 5.13: Simulated inter-annual variation of the averaged seasonal sea surface temperature (upper, unit: $°C$) and salinity (lower) within the CAA (same as figure 5.2) over the time period 1980–2099 (solid black line: January–March; gray solid line: April–June; black line with plus marker: July–September; gray line with plus marker: October–December)

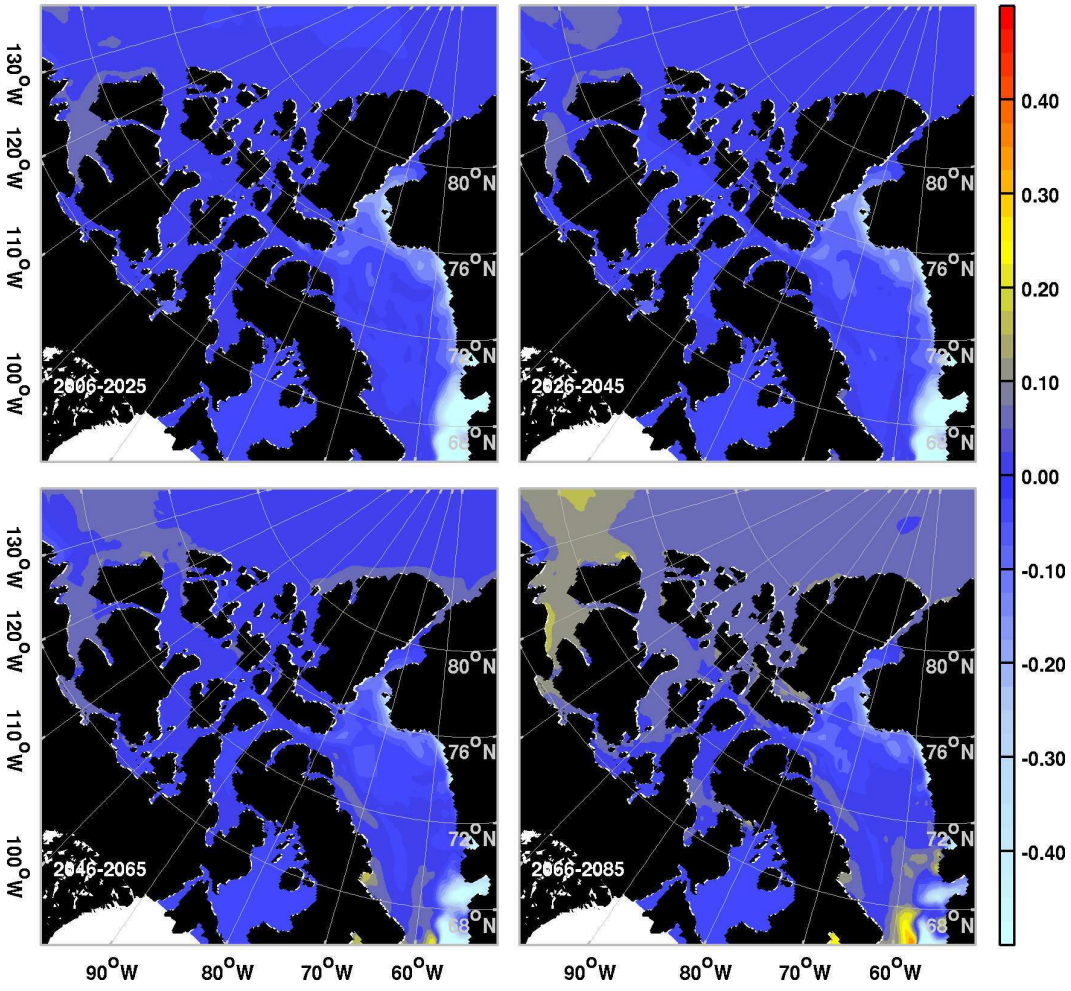

Figure 5.14: Winter sea surface temperature (SST, unit: $°C$) anomaly in 2006–2025 (upper left), 2026–2045 (upper right), 2046–2065 (lower left) and 2066–2085 (lower right), compared to the winter SST in 1986–2005

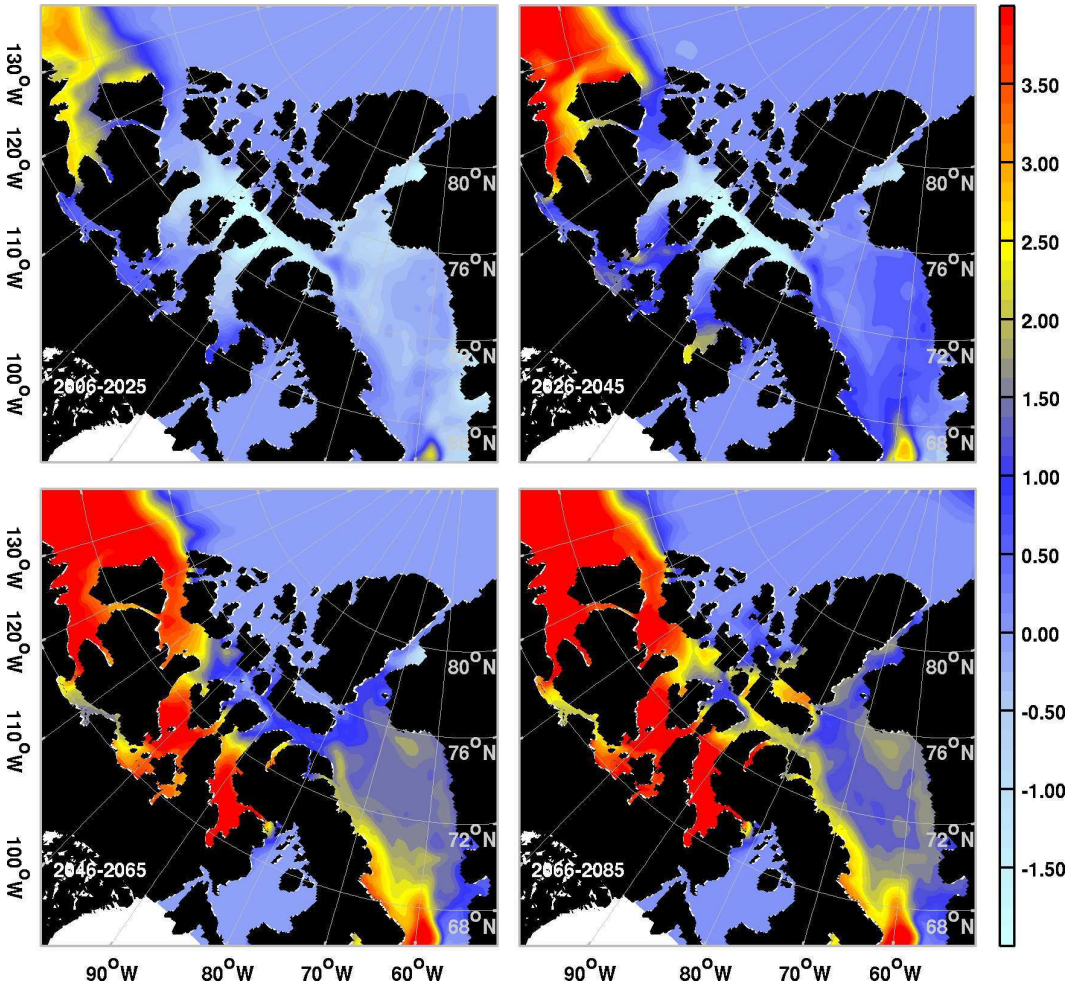

Figure 5.15: Same as figure 5.14 but for summer

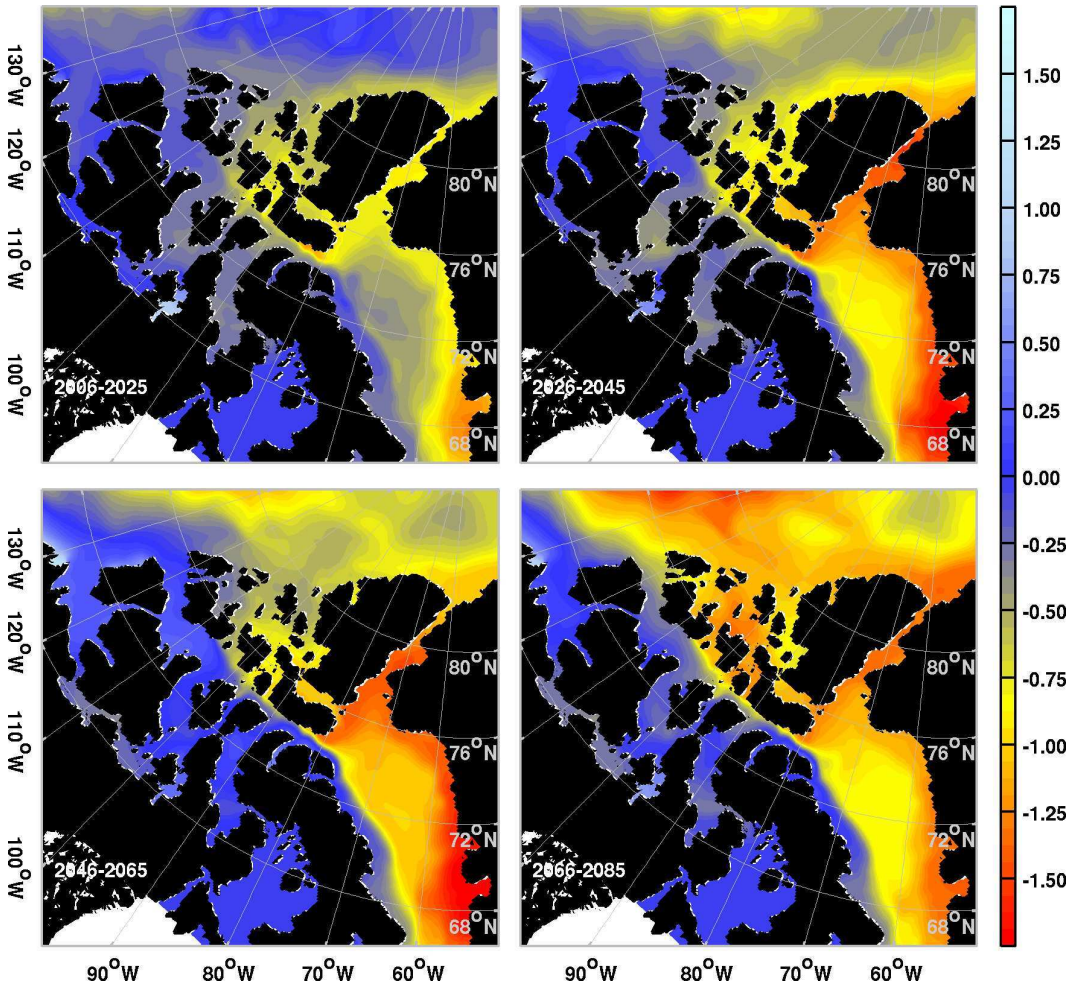

Figure 5.16: Winter sea surface salinity (SSS) anomaly in 2006–2025 (upper left), 2026–2045 (upper right), 2046–2065 (lower left) and 2066–2085 (lower right), compared to the winter SSS in 1986–2005. Note that the colors are used in reverse order from the previous figures.

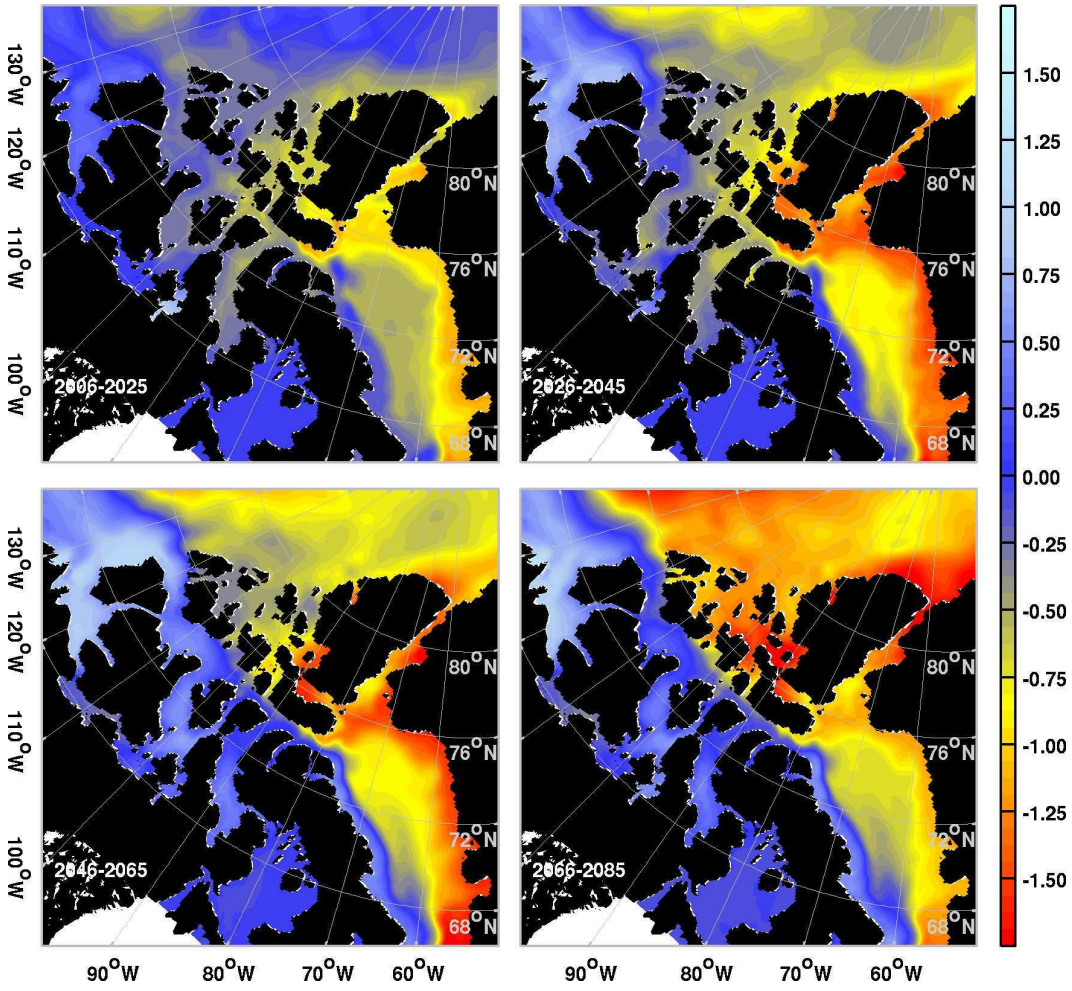

Figure 5.17: Same as figure 5.16 but for summer

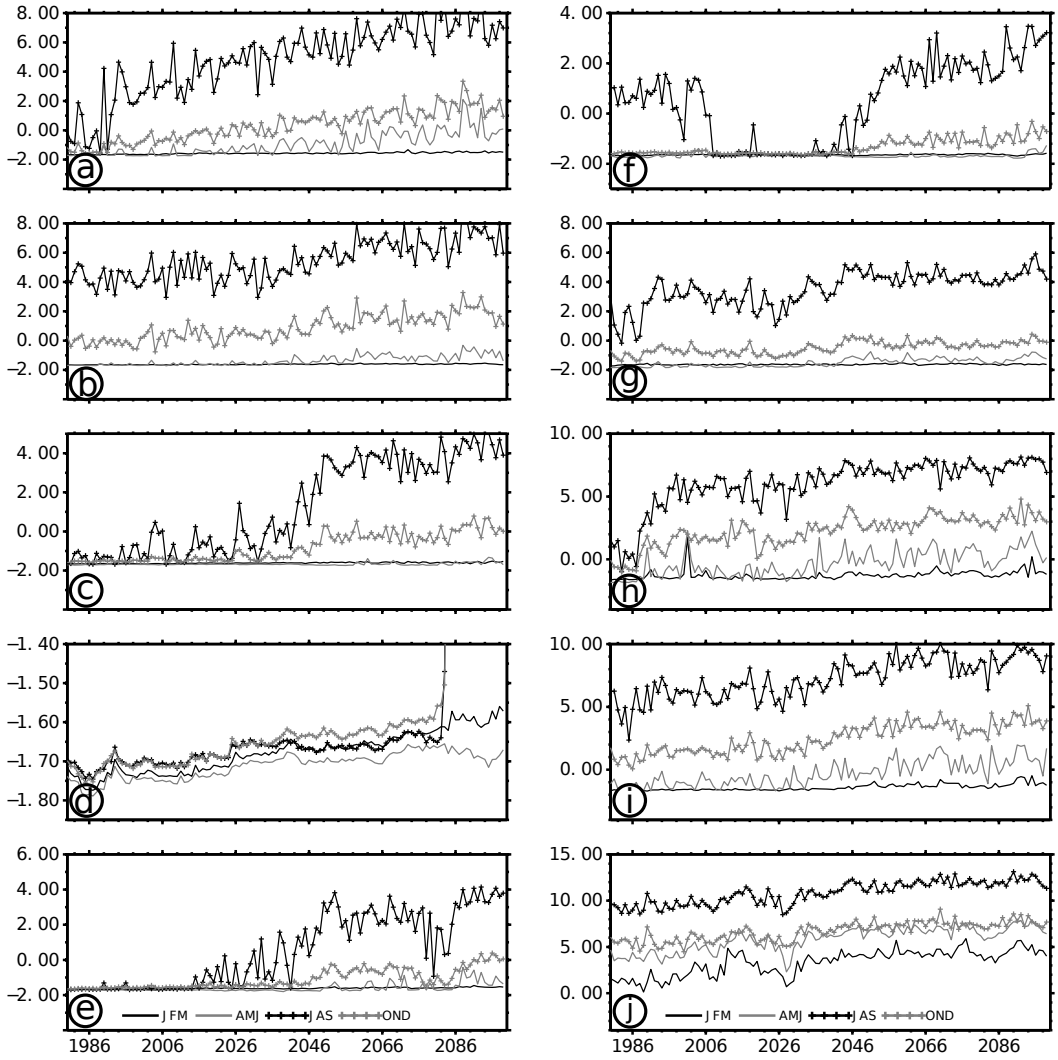

Figure 5.18: Simulated inter-annual variation of the averaged seasonal sea surface temperature (unit: $^{\circ}C$) at the select sites over the time period 1980–2099 (solid black line: January–March; gray solid line: April–June; black line with plus marker: July–September; gray line with plus marker: October–December)

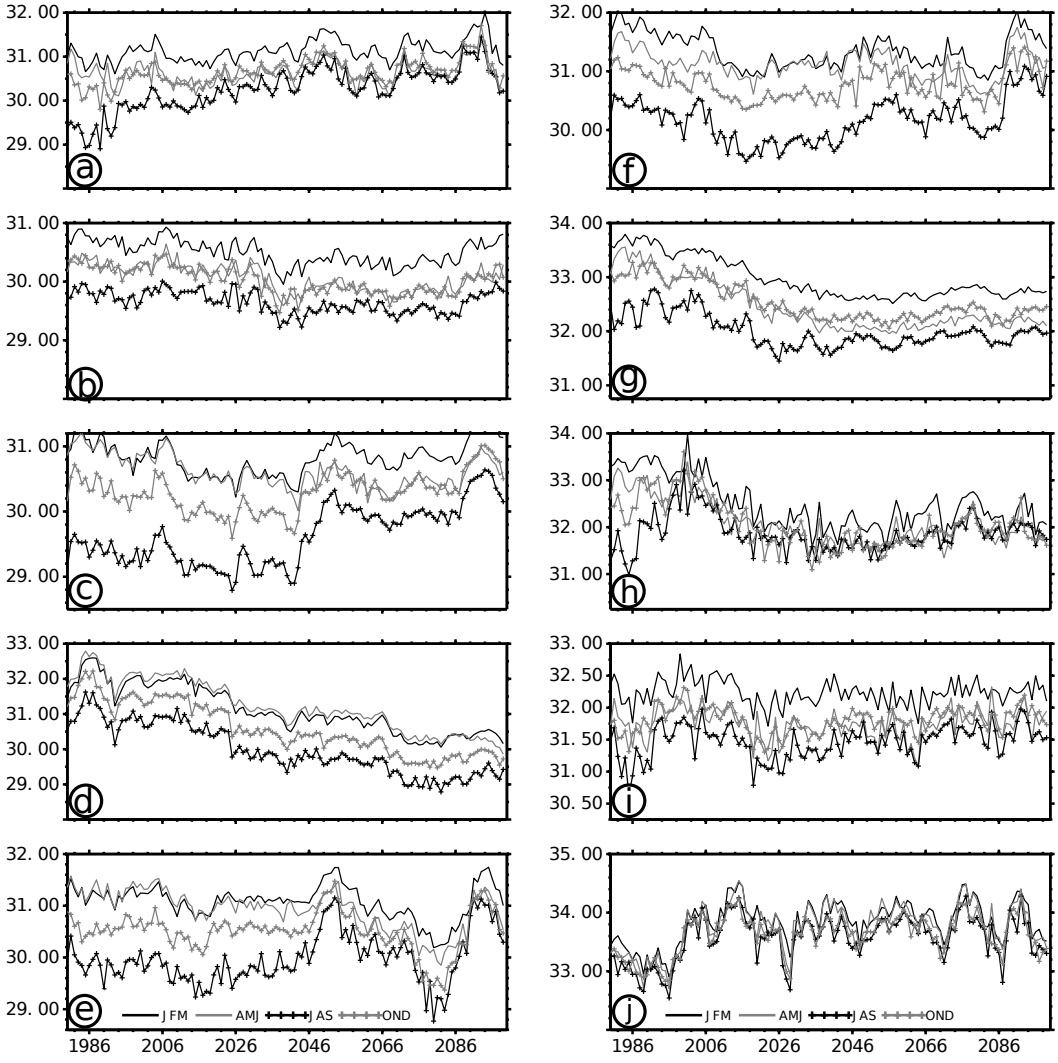

Figure 5.19: Same as figure 5.18 but for sea surface salinity

Bibliography

Amante, C., and B. W. Eakins (2009), ETOPO1 1 Arc-minute global relief model: procedures, data sources and analysis, *NOAA Technical Memorandum NESDIS NGDC-24*, *19*.

Barnier, B., et al. (2006), Impact of partial steps and momentum advection schemes in a global ocean circulation model at eddy-permitting resolution, *Ocean Dynamics*, *56*(5), 543–567, doi:10.1007/s10236.

Boé, J., A. Hall, and X. Qu (2009), September sea-ice cover in the Arctic Ocean projected to vanish by 2100, *Nature Geoscience*, *2*(5), 341–343.

Bourke, R. H., and R. P. Garrett (1987), Sea ice thickness distribution in the Arctic Ocean, *Cold Regions Science and Technology*, *13*(3), 259–280.

CIS (2002), Sea Ice Climatic Atlas: Northern Canadian Waters, 1971–2000.

Comiso, J. C., C. L. Parkinson, R. Gersten, and L. Stock (2008), Accelerated decline in the Arctic sea ice cover, *Geophysical Research Letters*, *35*(1), L01,703.

Dumas, J. A., G. M. Flato, and R. D. Brown (2006), Future projections of landfast ice thickness and duration in the Canadian Arctic, *Journal of Climate*, *19*(20), 5175–5189.

Eisenman, I., N. Untersteiner, and J. S. Wettlaufer (2007), On the reliability of simulated Arctic sea ice in global climate models, *Geophysical Research Letters*, *34*(10).

Fichefet, T., and M. A. M. Maqueda (1997), Sensitivity of a global sea ice model to the treatment of ice thermodynamics and dynamics, *Journal of Geophysical Research*, *102*(C6), 12,609–12,646, doi:10.1029/97JC00480.

Flato, G. M., and G. J. Boer (2001), Warming asymmetry in climate change simulations, *Geophysical Research Letters*, *28*(1), 195–198, doi: 10.1029/2000GL012121.

Goosse, H., T. Fichefet, and J.-M. Campin (1997), The effects of the water flow through the Canadian Archipelago in a global ice-ocean model, *Geophysical Research Letters*, *24*(12), 1507–1510, doi:10.1029/97GL01352.

Gordon, C., C. Cooper, C. A. Senior, H. Banks, J. M. Gregory, T. C. Johns, J. F. B. Mitchell, and R. A. Wood (2000), The simulation of SST, sea ice extents and ocean heat transports in a version of the Hadley Centre coupled model without flux adjustments, *Climate Dynamics*, *16*(2), 147–168.

Haas, C., A. Pfaffling, S. Hendricks, L. Rabenstein, J.-L. Etienne, and I. Rigor (2008), Reduced ice thickness in Arctic Transpolar Drift favors rapid ice retreat, *Geophysical Research Letters*, *35*(17), L17,501, doi: 10.1029/2008GL034457.

Howell, S. E. L., A. Tivy, J. J. Yackel, and S. McCourt (2008), Multi-year sea-ice conditions in the western Canadian Arctic Archipelago region of the Northwest Passage: 1968-2006, *Atmosphere-Ocean*, *46*(2), 229–242.

Howell, S. E. L., C. R. Duguay, and T. Markus (2009), Sea ice conditions and melt season duration variability within the Canadian Arctic Archipelago: 1979–2008, *Geophysical Research Letters*, *36*(10), L10,502.

Hu, X., and P. G. Myers (2013), A Lagrangian view of Pacific water inflow pathways in the Arctic Ocean during model spin-up, *Ocean Modelling*, *in press*.

Hunke, E. C., and J. K. Dukowicz (1997), An elastic-viscous-plastic model for sea ice dynamics, *Journal of Physical Oceanography*, *27*(9), 1849–1867.

IPCC (2000), Special report on emissions scenarios, *Intergovernmental Pannel on Climate Change*.

Kauker, F., T. Kaminski, M. Karcher, R. Giering, R. Gerdes, and M. Voßbeck (2009), Adjoint analysis of the 2007 all time Arctic sea-ice minimum, *Geophysical Research Letters*, *36*(3), L03,707.

Komuro, Y., and H. Hasumi (2005), Intensification of the Atlantic deep circulation by the Canadian Archipelago throughflow, *Journal of Physical Oceanography*, *35*(5), 775–789.

Kwok, R. (2006), Exchange of sea ice between the Arctic Ocean and the Canadian Arctic Archipelago, *Geophysical Research Letters*, *33*(16), L16,501.

Kwok, R. (2011), Observational assessment of Arctic Ocean sea ice motion, export, and thickness in CMIP3 climate simulations, *Journal of Geophysical Research*, *116*(C9).

Kwok, R., and D. A. Rothrock (2009), Decline in Arctic sea ice thickness from submarine and ICESat records: 1958–2008, *Geophysical Research Letters*, *36*(15), L15,501.

Kwok, R., G. F. Cunningham, M. Wensnahan, I. Rigor, H. J. Zwally, and D. Yi (2009), Thinning and volume loss of the Arctic Ocean sea ice cover: 2003–2008, *Journal of Geophysical Research*, *114*(C7), C07,005.

Large, W. G., and S. G. Yeager (2009), The global climatology of an interannually varying air–sea flux data set, *Climate Dynamics*, *33*(2), 341–364.

Lietaer, O., T. Fichefet, and V. Legat (2008), The effects of resolving the Canadian Arctic Archipelago in a finite element sea ice model, *Ocean Modelling*, *24*(3), 140–152.

Madec, G., and the NEMO team (2008), *NEMO ocean engine*, Note du Pôle de modélisation, Institut Pierre-Simon Laplace (IPSL), France, No 27, ISSN No 1288-1619.

Marshall, J., and F. Schott (1999), Open-ocean convection: Observations, theory, and models, *Reviews of Geophysics*, *37*(1), 1–64.

Melling, H. (2002), Sea ice of the northern Canadian Arctic Archipelago, *Journal of Geophysical Research*, *107*(C11), 3181.

Moore, S. E., and H. P. Huntington (2008), Arctic marine mammals and climate change: impacts and resilience, *Ecological Applications*, *18*(sp2), S157–S165.

Murray, R. J. (1996), Explicit generation of orthogonal grids for ocean models, *Journal of Computational Physics*, *126*(2), 251–273.

Parkinson, C. L., and D. J. Cavalieri (2008), Arctic sea ice variability and trends, 1979–2006, *Journal of Geophysical Research*, *113*(C7), C07,003.

Parkinson, C. L., and J. C. Comiso (2013), On the 2012 record low Arctic sea ice cover: Combined impact of preconditioning and an August storm, *Geophysical Research Letters*, *40*(7), 1356–1361, doi:10.1002/grl.50349.

Parkinson, C. L., D. J. Cavalieri, P. Gloersen, H. J. Zwally, and J. C. Comiso (1999), Arctic sea ice extents, areas, and trends, 1978–1996, *Journal of Geophysical Research*, *104*(C9), 20,837–20,856.

Peterson, I., J. Hamilton, S. Prinsenberg, and R. Pettipas (2012), Wind-forcing of volume transport through Lancaster Sound, *Journal of Geophysical Research*, *117*(C11), C11,018, doi:10.1029/2012JC008140.

Rothrock, D. A., Y. Yu, and G. A. Maykut (1999), Thinning of the Arctic sea-ice cover, *Geophysical Research Letters*, *26*(23), 3469–3472.

Rothrock, D. A., D. B. Percival, and M. Wensnahan (2008), The decline in arctic sea-ice thickness: Separating the spatial, annual, and interannual variability in a quarter century of submarine data, *Journal of Geophysical Research*, *113*, C05,003.

Serreze, M. C., et al. (2003), A record minimum arctic sea ice extent and area in 2002, *Geophysical Research Letters*, *30*(3), 1110.

Serreze, M. C., M. M. Holland, and J. Stroeve (2007), Perspectives on the Arctic's shrinking sea-ice cover, *Science*, *315*(5818), 1533–1536.

Solomon, S., D. Qin, M. Manning, Z. Chen, M. Marquis, K. B. Averyt, M. Tignor, H. L. Miller, et al. (2007), The physical science basis. Contribution of Working Group I to the Fourth Assessment Report of the Intergovernmental Panel on Climate Change, *4*.

Sou, T., and G. Flato (2009), Sea ice in the Canadian Arctic Archipelago: Modeling the past (19502004) and the future (204160), *Journal of Climate*, *22*(8), 2181–2198.

Steele, M., R. Morley, and W. Ermold (2001), PHC: A global ocean hydrography with a high-quality Arctic Ocean, *Journal of Climate*, *14*(9), 2079–2087.

Stroeve, J., M. Serreze, S. Drobot, S. Gearheard, M. Holland, J. Maslanik, W. Meier, and T. Scambos (2008), Arctic sea ice extent plummets in 2007, *Eos, Transactions American Geophysical Union*, *89*(2), 13–14.

Wang, M., and J. E. Overland (2009), A sea ice free summer Arctic within 30 years, *Geophysical Research Letters*, *36*(7), L07,502.

Wang, M., and J. E. Overland (2012), A sea ice free summer Arctic within 30 years: An update from CMIP5 models, *Geophysical Research Letters*, *39*(18).

Wang, Q., P. G. Myers, X. Hu, and A. B. Bush (2012), Flow constraints on pathways through the Canadian Arctic Archipelago, *Atmosphere-Ocean*, *50*(3), 373–385.

Chapter 6

Changes in the Central Canadian Arctic Archipelago Through-flow in a Future Warming Scenario

Abstract

In this study, the central Canadian Arctic Archipelago through-flow is simulated under the IPCC 20C3M and A1B climate forcing scenarios using a coupled ocean and sea ice pan-Arctic model. The present day simulated volume and liquid freshwater transport through the Lancaster Sound are in reasonable agreement with the up-to-date observations. A significant decrease in this oceanic transport is noticed in our simulation after 2020, which is related to the change in the along-channel sea surface height (SSH) gradient, particularly the lift of SSH in Baffin Bay. Freshwater storage increases both upstream and downstream of the archipelago. The increase in the Arctic Ocean freshwater storage is found to be associated with both lateral oceanic transport and surface input under the 20C3M forcing for 1970–1999 but can be mainly attributed to surface input under the A1B forcing for 2000–2099. The increase in Baffin Bay freshwater storage is the result of accumulation of lateral freshwater input, particularly through the central CAA. Lagrangian trajectories indicate that Pacific water entering the central CAA mainly follows the Alaskan route, with a "flat" Beaufort Gyre in the future simulation.

6.1 Introduction

Freshwater plays an important role in the high-latitude-oceans with the density stratification being more determined by the salinity difference (*Aagaard et al.*, 1981; *Sigman et al.*, 2004). Particularly in the Arctic Ocean, large amounts of freshwater from the continental rivers, precipitation minus evaporation (P-E) and fresher Pacific inflow (e.g., *Serreze et al.*, 2006) accumulate in the upper layer of the Beaufort Gyre due to Ekman convergence caused by the clockwise atmospheric circulation (e.g., *Proshutinsky et al.*, 2009). The variations in Arctic Ocean freshwater outflow is a big question because it will potentially have an impact on deep convection, deep water formation in subarctic seas, and in turn, the strength of the Atlantic Meridional Overturn Circulation (AMOC) (e.g. *Aagaard et al.*, 1985; *Aagaard and Carmack*, 1989; *Dickson et al.*, 1988; *Holland et al.*, 2001; *Mysak et al.*, 2005).

The Canadian Arctic Archipelago (CAA), a complex network of narrow straits, shallow ocean sills and basins (figure 6.1), is one of the two major pathways (the other is Fram Strait) of Arctic Ocean freshwater outflow to the North Atlantic (*Serreze et al.*, 2006; *Dickson et al.*, 2007). While freshwater exported through Fram Strait is dominated by sea ice, freshwater exported through the CAA is almost completely in the liquid phase. Recent observations (*Prinsenberg and Hamilton*, 2005; *Melling et al.*, 2008) and modeling results (*Aksenov et al.*, 2010; *McGeehan and Maslowski*, 2012; *Jahn et al.*, 2012) have suggested the CAA through-flow is a significant contributor to the net Arctic Ocean outflow. Cold fresh polar water from upstream passes the CAA through three major straits, Nares Strait, Jones Sound and Lancaster Sound, and then flows downstream, through Baffin Bay to the Labrador Sea.

Because the ocean flux through Jones Sound is relatively small (e.g., *Melling et al.*, 2008), most waters entering the CAA through M'Clure Strait and the Queen Elizabeth Islands (QEI) must pass Lancaster Sound ($\sim 250\,m$ deep and $\sim 65\,km$ wide). Ocean volume transport through Lancaster Sound is estimated

to be 0.46–0.7 Sv ($1\,Sv = 10^6\,m^3\,s^{-1}$) (*Melling et al.*, 2008; *Peterson et al.*, 2012), which accounts $\sim$ 35%–40% of the total CAA through-flow (*Kliem and Greenberg*, 2003; *Melling et al.*, 2008; *Peterson et al.*, 2012; *McGeehan and Maslowski*, 2012). These facts make Lancaster Sound an ideal location for monitoring the freshwater fluxes through the central CAA (*Prinsenberg and Hamilton*, 2005).

Previous studies show that the central CAA through-flow is controlled by the sea surface height (SSH) difference between the Arctic Ocean and Baffin Bay (e.g. *Kliem and Greenberg*, 2003; *Jahn et al.*, 2010; *Houssais and Herbaut*, 2011; *McGeehan and Maslowski*, 2012). Considering that variations in freshwater through the central CAA is mainly determined by velocity anomalies (*Lique et al.*, 2009; *Jahn et al.*, 2010; *Peterson et al.*, 2012), changes in SSH could significantly affect the freshwater delivered to downstream through the central CAA by modifying the currents. Note that it is still an open question if the variations are more sensitive to the changes in the upstream (*Houssais and Herbaut*, 2011) or downstream (*Jahn et al.*, 2010; *McGeehan and Maslowski*, 2012).

According to the *IPCC* (2007), an increase in precipitation over the arctic region has been predicted under the context of surface air warming in the future. That means the freshwater stored within the Arctic Ocean is very likely to increase in the future, as shown in numerical simulations (e.g. *Holland et al.*, 2006; *Koenigk et al.*, 2007; *Lehner et al.*, 2011; *Vavrus et al.*, 2012). Although enhanced freshwater export from the CAA might not initially impact the interior convection of the Labrador Sea (e.g. *Myers*, 2005; *McGeehan and Maslowski*, 2011), it is still of importance to know what impact the changes in Arctic freshwater content will have on the central CAA through-flow. Instead of an increase over the entire 21st century (*Koenigk et al.*, 2007), *Vavrus et al.* (2012) found a decrease in freshwater transport through the CAA after 2070 in their simulation, after an initial increase. *Hu and Myers* (2013a) also proposed the possibility that the SSH on the Baffin Bay side is lifted faster than that on

the Arctic Ocean side due to enhanced freshwater from Greenland, significantly reducing the central CAA through-flow.

In addition, waters within the central CAA are mainly of Pacific origin (*Jones et al.*, 2003), fed either by a Transpolar or Alaskan route (*Jones et al.*, 1998; *Steele et al.*, 2004; *Hu and Myers*, 2013b). Pacific water has different timescales for transiting the two routes before entering the central CAA. *Hu and Myers* (2013b) showed that the proportions of Pacific water delivered by the two routes are related to the spatial distribution of freshwater within the Canadian Basin. How the central CAA upstream inflow will change in the future is still unknown.

In this paper, we look at some of these questions related to the freshwater transport to, into and out of the CAA using a coupled ocean sea ice pan-Arctic model with IPCC scenarios forcing. The model configuration and experiment setup are exactly same as those in chapter 5, thus we will not repeat this section in this chapter. In the results section, we will first validate the simulated present day central CAA through-flow by comparing with the mooring data at Lancaster Sound, and interpret its variation with the evolution of along channel SSH gradient. Then we will present upstream changes with the evolution of simulated freshwater content within the Arctic Ocean and changes in Pacific water pathways. Changes in SSH and freshwater storage downstream in Baffin Bay will be discussed in the third section. A summary and discussion will be given at the end.

6.2 Results

6.2.1 Variation of the central CAA through-flow

6.2.1.1 Validation of the present day central CAA through-flow

Figure 6.2a shows the monthly simulated volume transport through west Lancaster Sound against the 1999–2010 mooring data (*Peterson et al.*, 2012). A

zoom of the overlapping time period is shown in figure 6.2b. The model estimates the volume transport to be $0.66Sv$ for 1999–2000, which is a bit higher than the observations ($0.49Sv$). The model captures the general feature of the seasonal cycle, with maximum in summer months (July–September) and lows in winter months, although the seasonal amplitude range is smaller than the observations. In terms of inter-annual variations, the enhanced flow during 2000–2001 is partly reproduced, however, the transport reduction observed during 2007–2008 is not found in the simulation. The overall correlation coefficient between the monthly time series is 0.41 (significant at the 95% level).

In our simulation, the freshwater flux through Lancaster Sound (figure 6.2c) is dominated by volume transport (correlation coefficient > 0.95). The average freshwater flux over 1999–2000 is $53mSv$ ($1mSv = 10^3 m^3 s^{-1}$), which is higher than the observations ($34mSv$). This is mainly due to the higher volume flux in the model. The correlation coefficient between the monthly simulated and observed freshwater fluxes over 1999–2010 is 0.48 (significant at 95% level, figure 6.2d).

6.2.1.2 Long term trend of the central CAA through-flow and changes in SSH

Over the simulation, the central CAA through-flow is strong in the 1980s and early 1990s and generally decreasing in the 21st century with the IPCC A1B climate scenario forcing (figure 6.2a). It reduces more significantly after 2020, even with westward flow toward the Arctic Ocean in some years after 2040.

To explain these changes, SSH are extracted along a track (figure 6.3) from the interior of the Canadian Basin, along the center line of Parry Channel, to the interior of Baffin Bay and shown as a Hovmöller diagram in figure 6.4 (left). A SSH gradient exists along the track, with generally higher SSH on the west side (Arctic Ocean) and lower SSH on the east side (Baffin Bay). The annual SSH differences between the west (averaged between point B and C in figure 6.3) and the east ends (averaged between point D and E in figure 6.3) is

found to be highly correlated to the central CAA through-flow volume transport, with an coefficient of 0.86 (significant at 95% level). Most of the variance is caused by the changes in SSH close to the mouth of Lancaster Sound in Baffin Bay. This is consistent with *McGeehan and Maslowski* (2012), who found a similar correlation coefficient between the SSH difference and the central CAA volume transport. But *McGeehan and Maslowski* (2012) used a different location (point M in figure 6.3) to represent the Arctic Ocean SSH. Why do we get the same results with a different upstream point? We think there are two possible reasons. One is that the variation is mainly determined by changes in downstream SSH. The other one is that waters passing M'Clure Strait and the point M (figure 6.3) have similar sources of variability (e.g., *Houssais and Herbaut*, 2011). Changes in downstream SSH is discussed in detail in section 6.2.3.

6.2.2 Changes in freshwater and Pacific water pathway in the upstream

6.2.2.1 Changes in Arctic Ocean freshwater storage

The sea ice fields (area and volume) are relatively stable in their annual means before 2000 under the 20C3M forcing but experience large decreases in the 21st century under the A1B forcing (figure 6.5, a and b). As the winter air temperature is still low even in the context of future warming, the central Arctic Ocean is always covered by sea ice during the winter. Thus, the shrinking of the sea ice cover is more significant during the summer months (lower edge of the shading in figure 6.5a). An summer ice-free Arctic Ocean only occurs toward the end of the simulation. For the annual ice area, it starts decreasing roughly from 2000, when the model is switched to the A1B forcing. From the beginning of the 2020s, the rate of decrease accelerates to be more than 5 times faster, from $\sim 6000\,km^2\,year^{-1}$ during 1980–2019 to $\sim 32000\,km^2\,year^{-1}$ during 2020–2049. After a short recovery in the 2050s, the ice area continues to

retreat over the rest of the integration. During the 1970s, there is an increase in ice volume due to ice thickness growth caused by low air temperatures (figure 6.5, b). There is no obvious tendency in ice volume during the period 1980–2020 although it decreases in the late 1990s and 2010s. From 2020, the ice volume dramatically declines almost steadily through to the end of our simulation, except for a small recovery in the 2050s. The rate of decrease of ice volume during the period 2020–2049 is more than 13 times faster than that during the period 1980–2019. By comparing with the changes in ice area, sea ice must be thinning at the same time.

The Arctic Ocean liquid freshwater storage demonstrates a steady increase over the whole simulation (figure 6.5c). The calculation is made following (*Serreze et al.*, 2006) with a reference salinity of 34.8, the climatologic mean of Arctic Ocean salinity (*Aagaard and Carmack*, 1989). Note waters with a salinity higher than the reference salinity are ignored in our calculation as in *Serreze et al.* (2006). The domain of the Arctic Ocean is defined as an area enclosed by Bering Strait, the northern coast of the CAA, Nares Strait, Fram Strait and the Barents Sea Opening (figure 6.1). The increase in freshwater storage within the Arctic Ocean in the future agrees with other model studies (e.g., *Holland et al.*, 2006; *Koenigk et al.*, 2007; *Lehner et al.*, 2011). By the end of the 21st century, the freshwater storage reaches $\sim 1.4 \times 10^5\, km^3$, similar to the *Koenigk et al.* (2007). However, our simulation shows an acceleration before 2020 instead of after 2040 as in *Koenigk et al.* (2007). A faster increase at the beginning of 21st century agrees with *Holland et al.* (2006). The rate of increase slows down after 2020 but liquid freshwater storage still increases to the end of our simulation.

A simple freshwater budget is presented in figure 6.5d, including both the freshwater received at the surface (precipitation, snow fall, ice melting and runoff) and total freshwater flux through the lateral straits (negative values means net freshwater inflow to the Arctic Ocean). It shows that both the lateral inflow and surface input contribute to the increase in freshwater through

to the end of the 1990s. Under the A1B forcing after 2000, there is a net freshwater outflow with large inter-annual variability (figure 6.5d), which is possibly associated with the evolution of the large-scale atmospheric circulation (*Condron et al.*, 2009). Over this period, the surface input is the major contributor to Arctic Ocean freshwater in most years.

6.2.2.2 Changes of Pacific water pathway in the future

To track the Pacific water, a mass-preserving Lagrangian package named ARIANE (*Blanke and Raynaud*, 1997; *Blanke et al.*, 1999) is used to compute the three-dimensional trajectories. Here two time periods are selected to represent different states of the central CAA through-flow (2020–2029: strong; 2050–2059: weak). The Pacific water pathway from the model spin-up (Year 5) is also chosen for comparison. As the particles are enough to resolve the major pathways of Pacific water within the Arctic Ocean, we reduced the number of particles from $\sim$ 36700 under the spin-up case to $\sim$ 4300 for the inter-annual cases. All the particles are released along a Bering Strait section, and tracked over 10 years with a sampling interval of 10 days. Each particle is assigned an initial volume (computed from the initial normal-to-section velocity and cross-section area), which is used to compute the volume of Pacific water passing a specific section. Because the pathways of Pacific water are similar for particles released in different months, here we show particles released in July as representative of all months.

Compared to the spin-up (Year 5, figure 6.6a), increased Arctic Ocean freshwater does not result in SSH increasing within the Beaufort Gyre but instead in the Eurasian Basin during both 2020–2029 and 2050–2060 (figure6.6, b and c), implying a redistribution of freshwater within the Arctic Ocean. Such a change may be associated with the variation of large scale atmospheric circulation (e.g., *Timmermans et al.*, 2011). As there is a positive Arctic Oscillation (AO) response to greenhouse gas forcing in HadCM3 (*Gillett et al.*, 2002), we can expect an increase in the positive phase of the AO in the 21st

century in our forcing (*Collins et al.*, 2001), exporting freshwater out of the Arctic to the North Atlantic (*Condron et al.*, 2009) and freshening the Eurasian Basin (*Timmermans et al.*, 2011).

Due to the Coriolis deflection, one might expect Pacific inflow to turn right upon entering the Arctic from Bering Strait. But with a SSH high centered on the Beaufort Gyre (figure 6.6a), the associated large pressure gradient force directed towards the coast generates a strong westward geostrophic flow, pushing Pacific water to the west and results in most of the Pacific water entering the central CAA from the Transpolar route (figure 6.6d). During both 2020–2029 and 2050–2060, the "flattened" Beaufort Gyre does not generate strong enough westward geostrophic flows, leading to all the Pacific water that exits the Arctic Ocean through the CAA (the portion of Pacific water passing Fram Strait is not shown in the figure) traveling along the Alaskan route (figure6.6, e and f). During 2020–2029, with a relatively strong eastward central CAA through-flow, $\sim 47\,\%$ of the total Pacific water ($\sim 1.15\,Sv$, in July 2020) can enter the central CAA (gray box in figure 6.6, d–f), exiting the Arctic Ocean in 10 years. But during 2050–2059, due to a weak central CAA through-flow, only $\sim 6\,\%$ of this inflow ($0.37\,Sv$) can flow into the central CAA within 10 years. About another $30\,\%$ of the incoming Pacific water is exported through Fram Strait during both the above time periods.

6.2.3 Changes in freshwater and SSH in the downstream

In section 6.2.1.2, we show the changes in SSH in Baffin Bay drives the changes in the central CAA through-flow. So what happens to waters downstream? At present, Baffin Bay features a cyclonic circulation, receiving waters through Nares Strait from the north, Jones Sound and Lancaster Sound from the west and eastern Davis Strait from south with the West Greenland Current and exporting relatively fresh water southward as the Baffin Island Current (e.g., *Dunlap and Tang*, 2006). SSH is high in boundary current regions and low in the interior of the Basin (figure 6.6a).

Under the IPCC A1B scenario forcing, SSH raises rapidly in Baffin Bay, especially along the west Greenland coast and in the northwest corner of the bay (figure 6.6, b and c). At the mouth of Lancaster Sound ($\overline{DE}$ in figure 6.3), SSH increases by $\sim 0.1\,m$ from the late 1980s to 2020 (figure 6.4). At the same time, the SSH increases by $\sim 0.15\,m$ in the Canadian Basin but with very limited impact on the eastern shelf, e.g., $\sim 0.05\,m$ at the mouth of M'Clure Strait. These changes in a drop by $\sim 0.05\,m$ in the SSH difference between the western and eastern ends of Parry Channel, reducing the central CAA through-flow (figure 6.4) by $\sim 50\%$. This agrees with *Kliem and Greenberg* (2003) that a decrease of $0.05m$ in Baffin Bay elevation could double the CAA through-flow. Over 2020–2060, SSH decreases faster at the west end, leading to another drop of $\sim 0.05\,m$ in the SSH difference by the end of this period. After that, although the SSH experiences large inter-annual variation at both the west and east ends of the CAA, there is no obvious trend in the SSH difference through to the end of 2080s. During this period, the central CAA through-flow also varies very little with an annual mean volume transport close to zero.

As SSH increases, freshwater storage in Baffin Bay also increases by $\sim 4000\,km^3$ before stabilizing in the beginning of the 2020s (figure 6.7a). The increase in freshwater accumulated in Baffin Bay is mainly a contribution of lateral exchange, mainly from the central CAA (figure 6.7b). The net southward volume transport through Davis Strait slowly decreases through to the mid of the 21st century (figure 6.7c).

6.3 Summary and discussion

Using forcing from the IPCC 20C3M and A1B climate scenarios, the volume transport through the CAA slows down, with periods of westward flow from Baffin Bay to the Arctic Ocean occurring occasionally after 2040 in our simulation. This variation in volume transport is found to be associated with

the evolution of the SSH difference between the west and east ends of Parry Channel. The main driver is the lifting of SSH at the mouth of Lancaster Sound in Baffin Bay.

Upstream of the CAA, freshwater storage in the Arctic Ocean increases significantly before 2020, driven by both the surface and net lateral (straits) freshwater input. Afterwards, surface input is the main contributor for the rest of our simulation. The freshwater storage downstream of the CAA, in Baffin Bay, also increase but is a result of the accumulation of lateral input, particularly from the central CAA before 2020.

At the same time, there is a loss of solid freshwater from the Arctic Ocean. The loss of sea ice accelerates from the beginning of the 2020s. More than 50% of ice volume is lost during 2020–2050. An summer ice-free Arctic Ocean likely will occur by 2100 based on our simulation.

Due to variations in the SSH fields, both the Pacific water circulation and the central CAA through-flow may experience substantial changes. With a "flat" Beaufort Gyre produced by a transfer of freshwater from the Canadian Basin to Eurasian Basin in our simulation, Pacific water entering the central CAA follows the Alaskan route rather than the Transpolar route. The amount of Pacific water is also impacted by the reduction in the CAA volume transport.

Our result is contrary to previous studies suggesting more outflow through the CAA in the future when more freshwater accumulates in the Arctic Ocean (e.g. *Koenigk et al.*, 2007; *Vavrus et al.*, 2012). By examining the effect of Greenland glacier melting on the flows, both *Rudels* (2011) and *Hu and Myers* (2013a) suggested changes in the Baffin Bay dynamic height field can reduce the eastward flow through the central CAA. Thus, this is still a question for future study.

6.4 Acknowledgements

This work has been supported by NSERC and Government of Canada International Polar Year awards. We are grateful to Westgrid and Compute Canada for computational resources. We thank C. Boening and A. Biastoch for providing us model output that was used for model spin-up open boundary forcing. We thank Canadian Centre for Climate Modelling and Analysis (CCCma) for the inter-annual open boundary forcing. We thank B. Blanke and N. Grima for freely sharing the Lagrangian analysis package ARIANE (available from http://stockage.univ-brest.fr/ grima/Ariane/). We also thank the Met Office Hadley Centre for making HadCM3 output available.

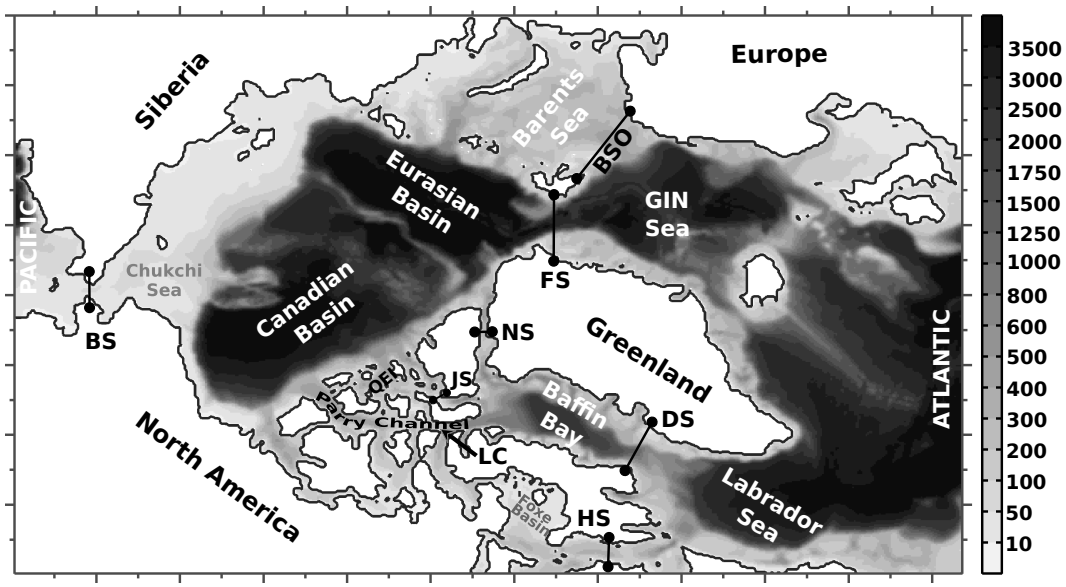

Figure 6.1: Model Domain and Bathymetry (gray shades: isodepth contours in meter, BS: Bering Strait; HS: Hudson Strait; DS: Davis Strait; QEI: Queen Elizabeth Islands; LC: Lancaster Sound; JS: Jones Sound; NS: Nares Strait; FS: Fram Strait; BSO: Barents Sea Opening)

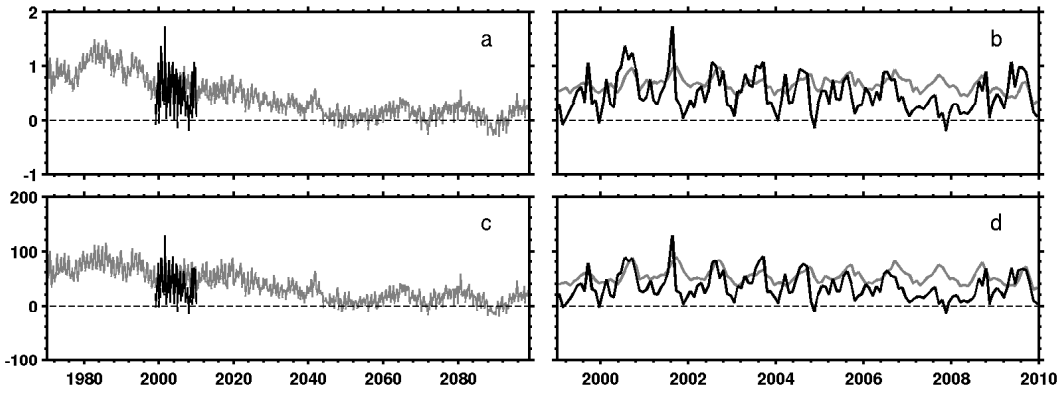

Figure 6.2: Simulated (gray solid line) against observational (black solid line) Lancaster Sound volume flux (unit: Sv) over the model simulation (a) and zoomed into 1999–2010 (b). c and d are similar but for freshwater flux (unit: mSv). The zero line is shown as a dashed horizontal line.

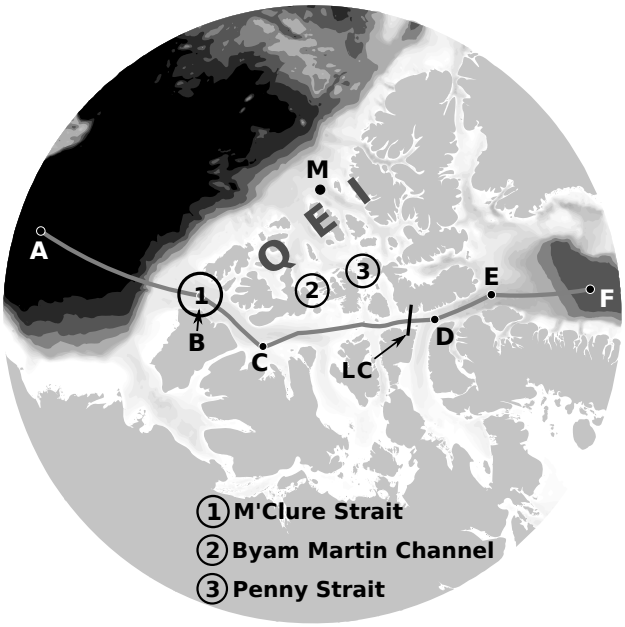

Figure 6.3: Map of the central CAA (background color: water depth, solid line: track for SSH calculation)

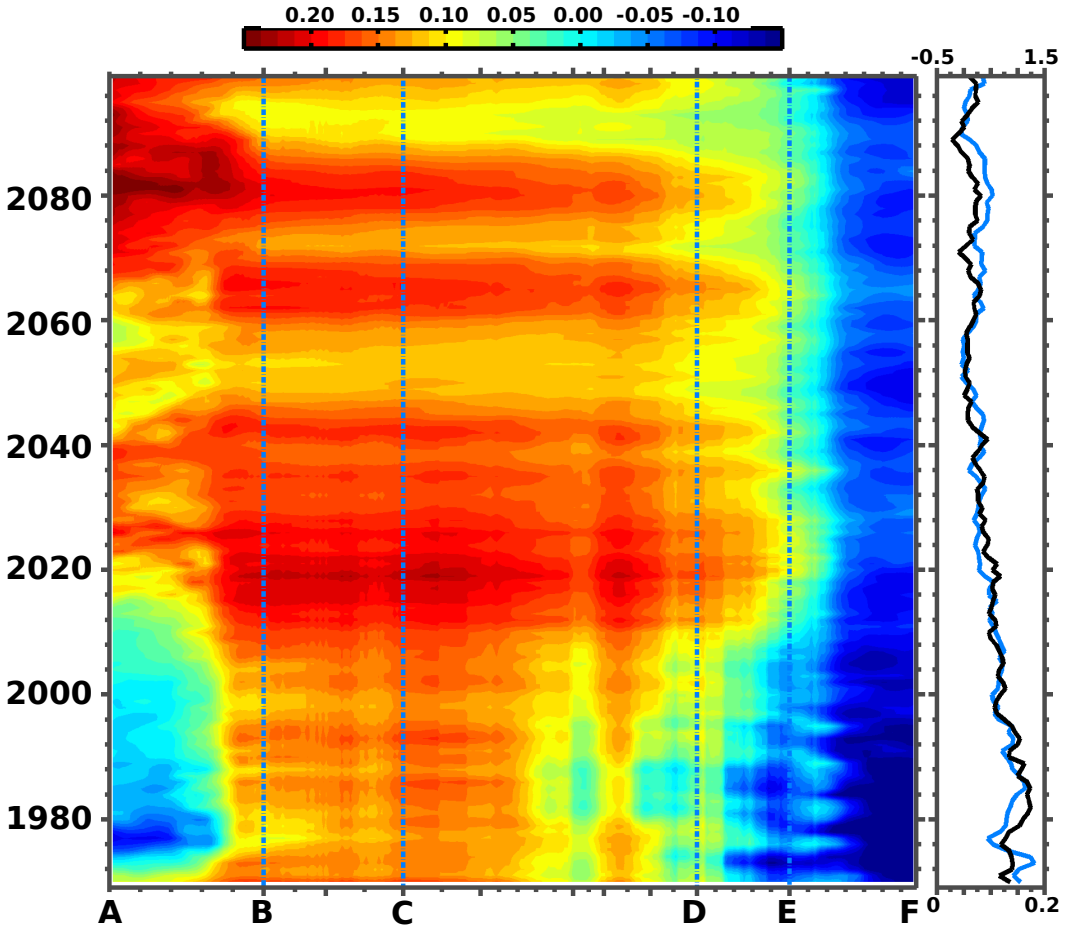

Figure 6.4: Left: annual mean SSH (*meter*) along the track (figure 6.3) over the model simulation. Right: SSH difference (blue line, $\text{SSH}_{\overline{BC}}$ – $\text{SSH}_{\overline{DE}}$, bottom-axis, unit: m) against Lancaster Sound volume transport (black line, top-axis, unit: Sv)

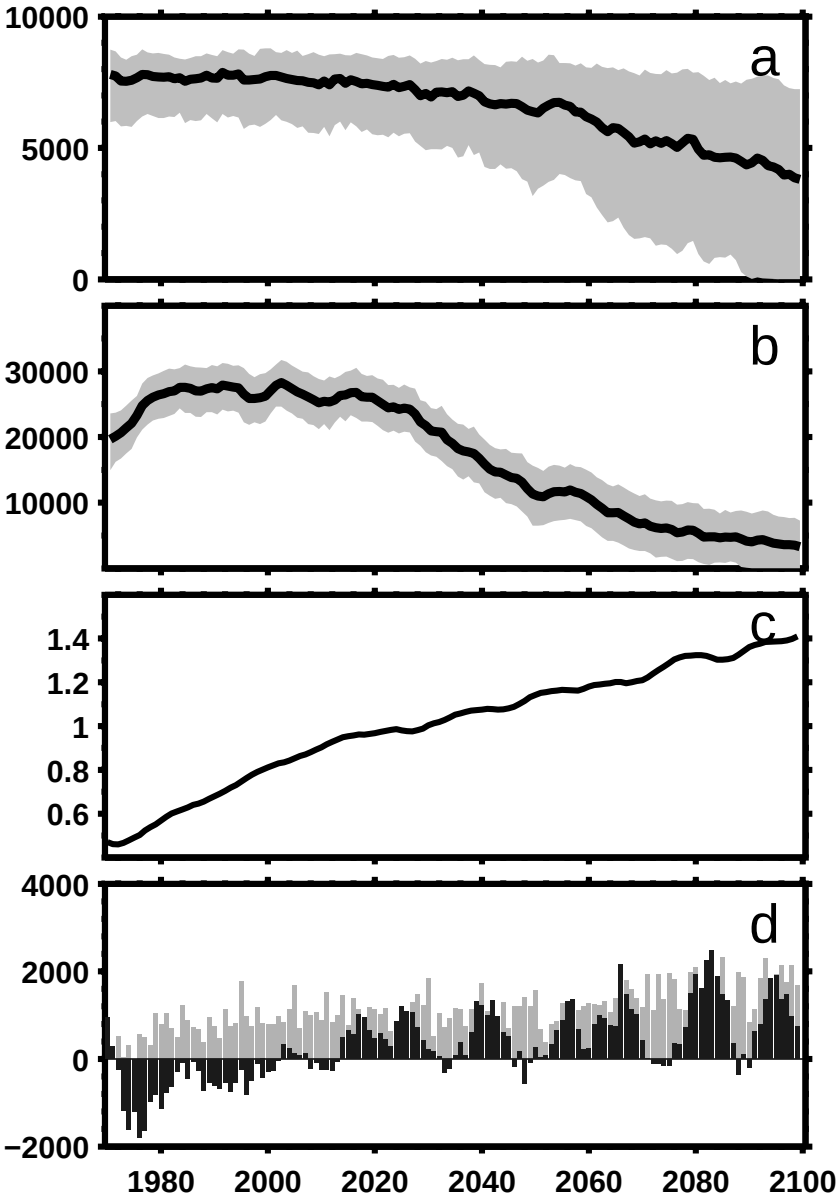

Figure 6.5: Simulated Arctic Ocean annual a) ice area (unit: $10^3\,km^2$, shading: annual range), b) ice volume (unit: km^3, shading: annual range), c) liquid freshwater storage (unit: $10^5\,km^3$), and d) freshwater input from ocean surface (gray bars, positive: into Arctic Ocean, unit: $km^3\,year^{-1}$) and lateral straits (black bars, positive: export from Arctic Ocean, unit: $km^3\,year^{-1}$)

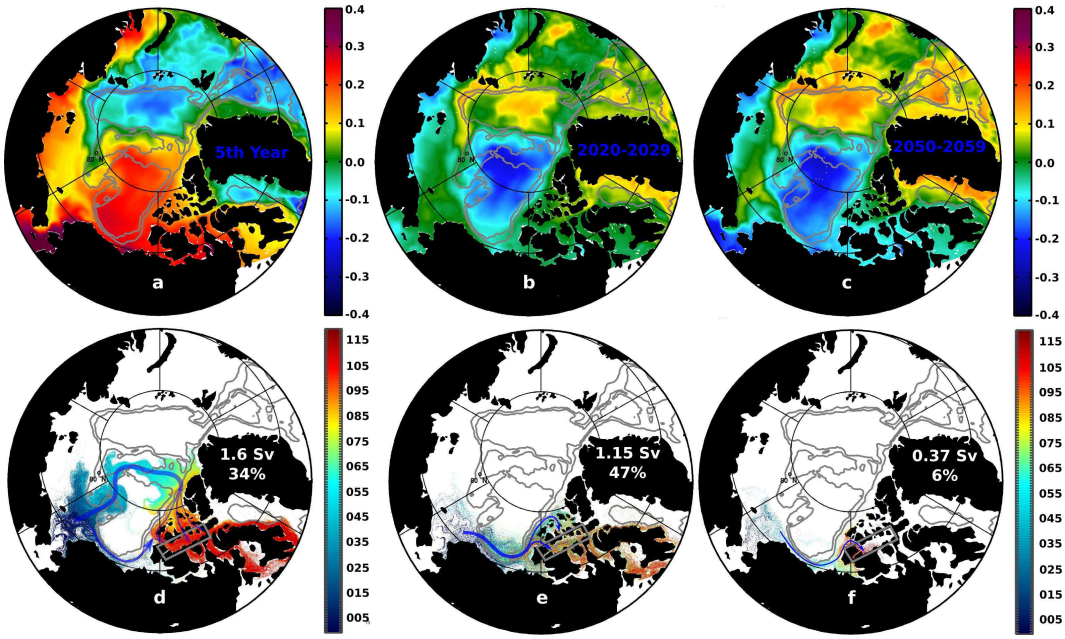

Figure 6.6: Time averaged SSH (a: annual average in year 5 during spin-up; b: anomaly from year 5 during 2020–2029; c: anomaly from year 5 during 2050–2059; contours: 1000 m and 2500 m water depth) and Pacific Water trajectories (d, e and f: released in July and only for Pacific water entering the central CAA within 10 years) during the same time period (colors: the integration time in month; blue arrows: major Pacific Water routes; text: the volume of Pacific inflow and percentage of Pacific water entering the central CAA; thick gray box: the central CAA for particle counting)

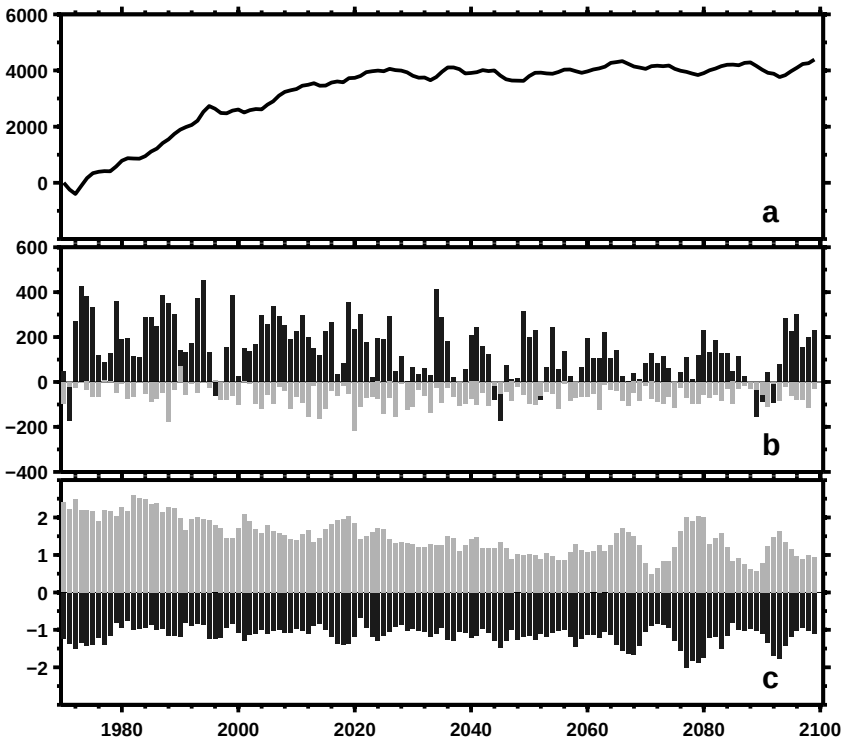

Figure 6.7: Simulated Baffin Bay annual a) liquid freshwater storage anomaly (unit: km^3), b) freshwater input from ocean surface (gray bars, positive: into Baffin Bay, unit: $km^3\,year^{-1}$) and lateral straits (black bars, positive: export from Baffin Bay, unit: $km^3\,year^{-1}$), c) southward (gray bars, unit: Sv) and northward (black bars) volume transport through Davis Strait

Bibliography

Aagaard, K., and E. C. Carmack (1989), The role of sea ice and other fresh water in the Arctic circulation, *Journal of Geophysical Research*, *94*(C10), 14,485–14,498.

Aagaard, K., L. K. Coachman, and E. C. Carmack (1981), On the halocline of the Arctic Ocean, *Deep Sea Research Part A. Oceanographic Research Papers*, *28*(6), 529–545.

Aagaard, K., J. H. Swift, and E. C. Carmack (1985), Thermohaline circulation in the Arctic Mediterranean seas, *Journal of Geophysical Research*, *90*(C3), 4833–4846.

Aksenov, Y., S. Bacon, A. C. Coward, and N. P. Holliday (2010), Polar outflow from the Arctic Ocean: A high resolution model study, *Journal of Marine Systems*, *83*, 14–37.

Blanke, B., and S. Raynaud (1997), Kinematics of the Pacific Equatorial Undercurrent: An Eulerian and Lagrangian approach from GCM results, *Journal of Physical Oceanography*, *27*(6), 1038–1053.

Blanke, B., M. Arhan, G. Madec, and S. Roche (1999), Warm water paths in the equatorial Atlantic as diagnosed with a general circulation model, *Journal of Physical Oceanography*, *29*(11), 2753–2768.

Collins, M., S. F. B. Tett, and C. Cooper (2001), The internal climate variabil-

ity of HadCM3, a version of the Hadley Centre coupled model without flux adjustments, *Climate Dynamics*, *17*(1), 61–81, doi:10.1007/s003820000094.

Condron, A., P. Winsor, C. Hill, and D. Menemenlis (2009), Simulated response of the Arctic freshwater budget to extreme NAO wind forcing, *Journal of Climate*, *22*(9), 2422–2437.

Dickson, R., B. Rudels, S. Dye, M. Karcher, J. Meincke, and I. Yashayaev (2007), Current estimates of freshwater flux through Arctic and subarctic seas, *Progress in Oceanography*, *73*(3-4), 210–230.

Dickson, R. R., J. Meincke, S. Malmberg, and A. J. Lee (1988), The "great salinity anomaly" in the Northern North Atlantic 1968-1982, *Progress in Oceanography*, *20*(2), 103–151, doi:10.1016/0079.

Dunlap, E., and C. C. L. Tang (2006), Modelling the mean circulation of Baffin Bay, *Atmosphere-Ocean*, *44*(1), 99–110.

Gillett, N. P., M. R. Allen, R. E. McDonald, C. A. Senior, D. T. Shindell, and G. A. Schmidt (2002), How linear is the Arctic Oscillation response to greenhouse gases?, *Journal of Geophysical Research*, *107*(D3), doi:10.1029/2001JD000589.

Holland, M. M., C. M. Bitz, M. Eby, and A. J. Weaver (2001), The role of ice-ocean interactions in the variability of the North Atlantic thermohaline circulation, *Journal of Climate*, *14*(5), 656–675, doi:10.1175/1520.

Holland, M. M., J. Finnis, and M. C. Serreze (2006), Simulated Arctic Ocean freshwater budgets in the twentieth and twenty-first centuries, *Journal of Climate*, *19*(23), 6221–6242.

Houssais, M.-N., and C. Herbaut (2011), Atmospheric forcing on the Canadian Arctic Archipelago freshwater outflow and implications for the Labrador Sea variability, *Journal of Geophysical Research*, *116*(C8), C00D02, doi:10.1029/2010JC006323.

Hu, X., and P. G. Myers (2013a), Impact of enhanced melt from west Greenland on the Canadian Arctic Archipelago throughflow, *Geophysical Research Letters*, *submitted*.

Hu, X., and P. G. Myers (2013b), A Lagrangian view of Pacific water inflow pathways in the Arctic Ocean during model spin-up, *Ocean Modelling*, *in press*.

IPCC (2007), Climate change 2007, the science of cliamte change, *Intergovernmental Pannel on Climate Change*.

Jahn, A., L. B. Tremblay, R. Newton, M. M. Holland, L. A. Mysak, and I. A. Dmitrenko (2010), A tracer study of the Arctic Ocean's liquid freshwater export variability, *Journal of Geophysical Research*, *115*(C7), C07,015.

Jahn, A., et al. (2012), Arctic Ocean freshwater: How robust are model simulations?, *Journal of Geophysical Research*, *117*(C8), C00D16, doi: 10.1029/2012JC007907.

Jones, E. P., L. G. Anderson, and J. H. Swift (1998), Distribution of Atlantic and Pacific waters in the upper Arctic Ocean: Implications for circulation, *Geophysical Research Letters*, *25*(6), 765–768.

Jones, E. P., J. H. Swift, L. G. Anderson, M. Lipizer, G. Civitarese, K. K. Falkner, G. Kattner, and F. A. McLaughlin (2003), Tracing Pacific water in the North Atlantic Ocean, *Journal of Geophysical Research*, *108*(C4), 3116.

Kliem, N., and D. A. Greenberg (2003), Diagnostic simulations of the summer circulation in the Canadian Arctic Archipelago, *Atmosphere-Ocean*, *41*(4), 273–289.

Koenigk, T., U. Mikolajewicz, H. Haak, and J. Jungclaus (2007), Arctic freshwater export in the 20th and 21st centuries, *Journal of Geophysical Research*, *112*(G4), G04S41, doi:10.1029/2006JG000274.

Lehner, F., C. C. Raible, D. Hofer, and T. F. Stocker (2011), The freshwater balance of polar regions in transient simulations from 1500 to 2100 AD using a comprehensive coupled climate model, *Climate Dynamics*, pp. 1–17.

Lique, C., A. M. Treguier, M. Scheinert, and T. Penduff (2009), A model-based study of ice and freshwater transport variability along both sides of Greenland, *Climate dynamics*, *33*(5), 685–705.

McGeehan, T., and W. Maslowski (2011), Impact of shelf-basin freshwater transport on deep convection in the western Labrador Sea, *Journal of Physical Oceanography*, *41*(11), 2187–2210, doi:10.1175/JPO.

McGeehan, T., and W. Maslowski (2012), Evaluation and control mechanisms of volume and freshwater export through the Canadian Arctic Archipelago in a high-resolution pan-Arctic ice-ocean model, *Journal of Geophysical Research*, *117*(C8), C00D14, doi:10.1029/2011JC007261.

Melling, H., et al. (2008), Fresh-water fluxes via Pacific and Arctic outflows across the Canadian polar shelf, *Arctic-Subarctic Ocean Fluxes: Defining the Role of the Northern Seas in Climate*, pp. 193–247.

Myers, P. G. (2005), Impact of freshwater from the Canadian Arctic Archipelago on Labrador Sea water formation, *Geophysical Research Letters*, *32*(6), L06,605.

Mysak, L. A., K. M. Wright, J. Sedláček, M. Eby, and E. S. M. Group (2005), Simulation of sea ice and ocean variability in the arctic during 1955–2002 with an intermediate complexity model, *Atmosphere-Ocean*, *43*(1), 101–118.

Peterson, I., J. Hamilton, S. Prinsenberg, and R. Pettipas (2012), Wind-forcing of volume transport through Lancaster Sound, *Journal of Geophysical Research*, *117*(C11), C11,018, doi:10.1029/2012JC008140.

Prinsenberg, S. J., and J. Hamilton (2005), Monitoring the volume, freshwater

and heat fluxes passing through Lancaster Sound in the Canadian Arctic Archipelago, *Atmosphere-Ocean*, *43*(1), 1–22.

Proshutinsky, A. Y., et al. (2009), Beaufort Gyre freshwater reservoir: State and variability from observations, *Journal of Geophysical Research*, *114*(C1), C00A10.

Rudels, B. (2011), Volume and freshwater transports through the Canadian Arctic Archipelago—Baffin Bay system, *Journal of Geophysical Research*, *116*(C8), C00D10, doi:10.1029/2011JC007019.

Serreze, M. C., et al. (2006), The large-scale freshwater cycle of the Arctic, *Journal of Geophysical Research*, *111*(C11), C11,010, doi:10.1029/2005JC003424.

Sigman, D. M., S. L. Jaccard, and G. H. Haug (2004), Polar ocean stratification in a cold climate, *Nature*, *428*(6978), 59–63.

Steele, M., J. Morison, W. Ermold, I. Rigor, M. Ortmeyer, and K. Shimada (2004), Circulation of summer Pacific halocline water in the Arctic Ocean, *Journal of Geophysical Research*, *109*(C2), C02,027.

Timmermans, M., A. Proshutinsky, R. A. Krishfield, D. K. Perovich, Richter, T. P. Stanton, and J. M. Toole (2011), Surface freshening in the Arctic Ocean's Eurasian Basin: An apparent consequence of recent change in the wind-driven circulation, *Journal of Geophysical Research*, *116*(C8), C00D03, doi:10.1029/2011JC006975.

Vavrus, S. J., M. M. Holland, A. Jahn, D. A. Bailey, and B. A. Blazey (2012), Twenty-first-century Arctic climate change in CCSM4, *Journal of Climate*, *25*(8), 2696–2710, doi:10.1175/JCLI.

Chapter 7

Summary and discussion

In this thesis, a series of numerical simulations exploring several important freshwater processes on both sides, as well the interior, of the Canadian Arctic Archipelago (CAA), are conducted using a coupled ocean and sea ice pan-Arctic model based on the Nucleus for European Modelling of the Ocean (NEMO) numerical framework version 3.1. These results improve current knowledge about

- circulation and residence time of Pacific water in the Arctic Ocean; entry of Pacific water into the central CAA; impact of Arctic Ocean freshwater on the shifting of Pacific water pathways
- potential impacts of the melting of Greenland ice sheet on surrounding waters both in the tracer fields and circulations
- sea ice and surface ocean condition within the CAA; changes in Arctic Ocean freshwater and sea surface height and their influences on the central CAA throughflow and Pacific water circulation under a warmer climate

In the Arctic Ocean, in chapter 3, two major Pacific water pathways are identified using three dimensional (3D) Lagrangian trajectories based upon simulated ocean velocity fields. Compared to previous studies using ocean

tracers or nutrients (e.g., *Jones et al.*, 1998, 2008; *Steele et al.*, 2004), our analysis directly and quantitatively estimates the volumes/proportions of Pacific water delivered by Transpolar route and Alaskan route as well as the associated residence times. Typically, Pacific water spends about one year within the Chukchi Sea before entering the interior of the deep basins. Within 10 years, more than 70% of the Pacific water is exported out of the Arctic Ocean, either from Fram Strait or the CAA channels (Nares Strait, Jones Sound and Lancaster Sound). About $\sim$ 50% of this water flows through the central CAA (Lancaster Sound) through the openings in Queen Elizabeth Islands in the north and M'Clure Strait in the west. Travel time to the central CAA is $\sim$ 4–8 years in the deep basin for the Transpolar route while only $\sim$ 2–5 years for the Alaskan route.

Model drift provides us the opportunity to use velocity fields associated with different Arctic Ocean circulation regimes. With different circulation patterns, the total amount of Pacific water entering the central CAA is similar, e.g., $0.34\,Sv$, $0.35\,Sv$, $0.35\,Sv$ based upon Year 5, 10 and 15 velocity fields, respectively. But the proportions of Pacific water delivered by the two routes are different, e.g., about 98% of Pacific water entering the central CAA comes from Transpolar route in Year 5 but only 35% in Year 15. Such a shift reduces the time scale for Pacific water to enter the central CAA. In addition, although the Transpolar route (including Pacific water passing Fram Strait) shifts in space, its outer edge is always approximately the $7\,m$-contour of freshwater content (top $227\,m$). Changes in freshwater content can directly affect the dynamic height (*McPhee et al.*, 2009). We show changes in velocity are related to the changes in the pressure gradient force (PGF) normal to the current.

To estimate the contribution of the evolution of the model freshwater content to the pressure gradient force (PGF), we calculate the PGF in two different ways, one computing the dynamic height including both the baroclinic effect and barotropic effect (sea surface height) and one following (*Steele and Ermold*, 2007) with the 3D salinity and temperature from Year 5 as fixed refer-

ence fields. The salinity component using the reference fields exactly tells how the PGF changes from the first method. This shows that the evolution of the geostrophic circulation is a result of the evolution of the large scale freshwater content in the Beaufort Gyre.

On the Baffin Bay side, melting of the Greenland ice sheet also potentially influences the waters within the CAA. By adding different amounts of freshwater in runoff, a series of sensitivity experiments are conducted to study the impacts of Greenland melt on surrounding waters. Compared to a control run, enhanced Greenland melt significantly increases the freshwater stored within Baffin Bay on inter-annual timescales due to a reduction of salinity in the upper layers of the water column. As a result, dynamic heights are raised in Baffin Bay, particularly in the coastal regions, reducing the pressure gradient across the CAA. The CAA throughflow is driven by the sea surface height (SSH) difference between the Arctic Ocean and Baffin Bay (e.g., *Jahn et al.*, 2010; *Houssais and Herbaut*, 2011; *McGeehan and Maslowski*, 2012). Therefore, the weakened PGF leads to a reduction in volume and freshwater transport through the CAA channels. This phenomenon is also noticed in our climate scenario simulation for the 21st century. However, the total freshwater exported from the Arctic Ocean varies very little because the outflow through Fram Strait is strengthened to compensate the reduction through the CAA. Also the strengthened cyclonic circulation in Baffin Bay may lift the warm West Greenland Intermediate Water, which affects the heat content in the upper water column. How much of this can be explained by the changes in baroclinic transport (*Rudels*, 2011) is for future study.

Within the CAA, the future condition of sea ice and ocean is studied using forcing data from global climate models under the IPCC 20C3M and A1B climate scenarios. Remarkable changes in sea ice are shown in the simulation from the mid 2020s to the mid 2060s, with a shrinking of 65% in concentration and a thinning of 75% over the 40 years. This leads to the opening of Northwest Passage by the 2050s. The east route, through Peel Sound, Victoria Strait

and Amundsen Gulf, is most likely to open first. Some regions, such as central Parry Channel, show an increase in sea ice, related to enhanced ice velocity with lower concentration. At the same time, lower albedo results in more heat absorbed by the ocean, increasing the sea surface temperature, especially in summer. But sea surface salinity within the CAA does not show any trend, showing a strong decadal oscillation with a period of $\sim$ 40 years. Freshening is more obvious in the upstream (Beaufort Sea) and downstream (Baffin Bay) waters.

In this thesis, we have presented many processes that might affect the waters within the CAA. A higher resolution model, which can resolves the CAA straits, e.g., Nares Strait, better, with higher spatial and temporal resolution atmospheric forcing, is the next step to improve the accuracy of the simulation and the estimation of the fluxes through the CAA. Updated runoff data including the melting of Greenland ice sheet (e.g., *Velicogna*, 2009; *van den Broeke et al.*, 2009) and Canadian Arctic ice caps (*Sharp et al.*, 2011) also should be considered. To reach a more robust simulation of future sea ice and ocean in the Arctic, including the CAA, more simulations using different models and forcings are required to estimate the range of variability.

Bibliography

Houssais, M.-N., and C. Herbaut (2011), Atmospheric forcing on the Canadian Arctic Archipelago freshwater outflow and implications for the Labrador Sea variability, *Journal of Geophysical Research*, *116*(C8), C00D02, doi: 10.1029/2010JC006323.

Jahn, A., B. Tremblay, L. A. Mysak, and R. Newton (2010), Effect of the large-scale atmospheric circulation on the variability of the Arctic Ocean freshwater export, *Climate Dynamics*, *34*(2), 201–222.

Jones, E. P., L. G. Anderson, and J. H. Swift (1998), Distribution of Atlantic and Pacific waters in the upper Arctic Ocean: Implications for circulation, *Geophysical Research Letters*, *25*(6), 765–768.

Jones, E. P., L. G. Anderson, S. Jutterström, L. Mintrop, and J. H. Swift (2008), Pacific freshwater, river water and sea ice meltwater across Arctic Ocean basins: Results from the 2005 Beringia Expedition, *Journal of Geophysical Research*, *113*(C8), C08,012.

McGeehan, T., and W. Maslowski (2012), Evaluation and control mechanisms of volume and freshwater export through the Canadian Arctic Archipelago in a high-resolution pan-Arctic ice-ocean model, *Journal of Geophysical Research*, *117*(C8), C00D14, doi:10.1029/2011JC007261.

McPhee, M. G., A. Y. Proshutinsky, J. H. Morison, M. Steele, and M. B. Alkire (2009), Rapid change in freshwater content of the Arctic Ocean, *Geophysical Research Letters*, *36*(10), L10,602, doi:10.1029/2009GL037525.

Rudels, B. (2011), Volume and freshwater transports through the Canadian Arctic Archipelago—Baffin Bay system, *Journal of Geophysical Research*, *116*(C8), C00D10, doi:10.1029/2011JC007019.

Sharp, M., D. O. Burgess, J. G. Cogley, M. Ecclestone, C. Labine, and G. J. Wolken (2011), Extreme melt on Canada's Arctic ice caps in the 21st century, *Geophysical Research Letters*, *38*(11), doi:10.1029/2011GL047381.

Steele, M., and W. Ermold (2007), Steric sea level change in the Northern Seas, *Journal of Climate*, *20*(3), 403–417, doi:10.1175/JCLI4022.1.

Steele, M., J. Morison, W. Ermold, I. Rigor, M. Ortmeyer, and K. Shimada (2004), Circulation of summer Pacific halocline water in the Arctic Ocean, *Journal of Geophysical Research*, *109*(C2), C02,027.

van den Broeke, M., J. Bamber, J. Ettema, E. Rignot, E. Schrama, W. J. van de Berg, E. van Meijgaard, I. Velicogna, and B. Wouters (2009), Partitioning recent Greenland mass loss, *Science*, *326*(5955), 984–986, doi:10.1126/science.1178176.

Velicogna, I. (2009), Increasing rates of ice mass loss from the Greenland and Antarctic ice sheets revealed by GRACE, *Geophysical Research Letters*, *36*(19), L19,503.

Appendix A

Kinematic boundary condition

A.1 Solid earth kinematic boundary condition

In the model, the water-bottom interface, is assumed to be time independent and impenetrable to fluid. This is the solid earth kinematic boundary condition. The water depth (sea floor) is expressed as a function of the horizontal vector ($\mathbf{i}$, $\mathbf{j}$),

$$z = -H(\mathbf{i}, \mathbf{j}) \tag{A.1}$$

and the unit normal (from the ocean into the underlying sea floor) is

$$\hat{\mathbf{n}}_H = -\frac{\nabla(z + H)}{|\nabla(z + H)|} \tag{A.2}$$

Thus, the no-normal flow condition at the bottom requires

$$\mathbf{v} \cdot \hat{\mathbf{n}}_H = 0 \tag{A.3}$$

which can be expanded as

$$w|_{z=-H} + \mathbf{U}_h \cdot \nabla(H)|_{z=-H} = 0 \tag{A.4}$$

A.2 Upper surface kinematic boundary condition

Compared to the sea floor, the upper ocean surface is considered to be time-dependent,

$$z = \eta\,(\mathbf{i},\,\mathbf{j},\,\mathbf{t}) \tag{A.5}$$

with mass transport crossing the interface through precipitation, evaporation, runoff and ice melt. The mass transport rate crossing an area element at the surface is

$$dM_\eta = -\,dA_\eta \hat{\mathbf{n}}_\eta \cdot (\hat{\mathbf{n}}_P\,P\,\rho_P + \hat{\mathbf{n}}_E\,E\,\rho_E + \hat{\mathbf{n}}_R\,R\,\rho_R + \hat{\mathbf{n}}_I\,I\,\rho_I) \tag{A.6}$$

where the $\hat{\mathbf{n}}_P$, $\hat{\mathbf{n}}_E$, $\hat{\mathbf{n}}_R$, $\hat{\mathbf{n}}_I$ represent the direction of Precipitation (P), Evaporation (E), Runoff (R) and Ice melt (I). The unit normal at the surface is given by

$$\hat{\mathbf{n}}_\eta = \frac{\nabla(z - \eta)}{|\nabla(z, -\eta)|} \tag{A.7}$$

and the area element is

$$dA_\eta = |\nabla(z - \eta)|\,d\mathbf{i}d\mathbf{j} \tag{A.8}$$

Here we assume that the direction of mass transport is always normal to the surface,

$$\hat{\mathbf{n}} \cdot \hat{\mathbf{n}}_P = -1,\ \hat{\mathbf{n}} \cdot \hat{\mathbf{n}}_R = -1,\ \hat{\mathbf{n}} \cdot \hat{\mathbf{n}}_I = -1,\ \hat{\mathbf{n}} \cdot \hat{\mathbf{n}}_E = 1 \tag{A.9}$$

and the density is generalized as ρ_w, thus the mass flux (q_w) can be expressed in the following form,

$$q_w = \frac{dM_\eta}{\rho_w\,dA} = P - E + R + I \tag{A.10}$$

where $dA = d\mathbf{i}\,d\mathbf{j}$.

Considering mass conservation, within a region (dA), the time tendency of mass is given by

$$\frac{\partial M}{\partial t} = \frac{\partial}{\partial t}\left(\int_{-H}^{\eta} \rho_w\,dz\right) = \rho_w\,\frac{\partial \eta}{\partial t}$$

which is balanced by the fluxes crossing the ocean surface ($\rho_w\, q_w$), convergence of mass due to horizontal convergence ($\nabla \cdot \int_{-H}^{\eta} \rho_w\, \mathbf{U}_h dz$) and sources within the vertical water column (S_M, ignored by the model). Thus,

$$\begin{aligned}
\rho_w \frac{\partial \eta}{\partial t} &= \rho_w\, q_w \,-\, \nabla \cdot \int_{-H}^{\eta} \rho_w\, \mathbf{U}_h\, dz \\
&= \rho_w\, q_w \,-\, \rho_w \left(\mathbf{U}_h \cdot \nabla \eta|_{z=\eta} \,+\, \mathbf{U}_h \cdot \nabla H|_{z=-H} \,+\, \int_{-H}^{\eta} \nabla \cdot \mathbf{U}_h\, dz \right) \\
&= \rho_w\, q_w \,-\, \rho_w \left(\mathbf{U}_h \cdot \nabla \eta|_{z=\eta} \,+\, \mathbf{U}_h \cdot \nabla H|_{z=-H} \,-\, \int_{-H}^{\eta} \frac{\partial w}{\partial z}\, dz \right) \\
&= \rho_w\, q_w \,-\, \rho_w \left(\mathbf{U}_h \cdot \nabla \eta|_{z=\eta} \,-\, w|_{z=\eta} \right) \,+\, \rho_w \underbrace{\left(\mathbf{U}_h \cdot \nabla H|_{z=-H} \,+\, w|_{z=-H} \right)}_{0} \\
&= \rho_w\, q_w \,-\, \rho_w \left(\mathbf{U}_h \cdot \nabla \eta|_{z=\eta} \,-\, w|_{z=\eta} \right)
\end{aligned} \tag{A.11}$$

Using q_w from eq(A.10), the final kinematic boundary condition is given in the following form:

$$w|_{z=\eta} \,=\, \frac{\partial \eta}{\partial t} \,+\, \mathbf{U}_h \cdot \nabla \eta|_{z=\eta} \,-\, (P \,-\, E \,+\, R \,+\, I) \tag{A.12}$$

Appendix B

Prognostic equation of free sea surface height

The prognostic equation of η can be obtained from vertical integration of the continuity equation using the above bottom (A.4) and surface (A.12) kinematic conditions:

$$
\begin{aligned}
0 &= \int_{-H}^{\eta} \left(\frac{\partial w}{\partial z} + \nabla \cdot \mathbf{U}_h \right) dz \\
&= w|_{z=\eta} - w|_{z=-H} + \nabla \cdot \int_{-H}^{\eta} \mathbf{U}_h \, dz - \mathbf{U}_h \cdot \nabla \eta_{z=\eta} + \mathbf{U}_h \cdot \nabla(-H)|_{z=-H} \\
&= \underbrace{w|_{z=\eta} - \frac{\partial \eta}{\partial t} - \mathbf{U}_h \cdot \nabla \eta_{z=\eta} + (P - E + R + I)}_{0} \\
&\quad + \underbrace{w|_{z=-H} + \mathbf{U}_h \cdot \nabla H}_{0} \\
&\quad + \frac{\partial \eta}{\partial t} - (P - E + R + I) + \nabla \cdot \int_{H}^{\eta} \mathbf{U}_h \, dz
\end{aligned}
$$

$\Rightarrow$

$$
\frac{\partial \eta}{\partial t} = (P - E + R + I) - \nabla \cdot \left[(H + \eta) \, \overline{\mathbf{U}}_h \right] \tag{B.1}
$$

where the vertical averaged horizontal velocity $\overline{\mathbf{U}}_h = \frac{1}{H+\eta} \int_H^{\eta} \mathbf{U}_h \, dz$.

Appendix C

Curvilinear coordinate system operators

Here we take q as a scalar variable, and $\mathbf{A} = (a_1, a_2, a_3)$ as a vector in the curvilinear coordinate system (i, j, k).

$$\nabla q = \frac{1}{e_1}\frac{\partial q}{\partial i}\mathbf{i} + \frac{1}{e_2}\frac{\partial q}{\partial j}\mathbf{j} + \frac{1}{e_3}\frac{\partial q}{\partial k}\mathbf{k}$$

$$\nabla \cdot \mathbf{A} = \frac{1}{e_1\, e_2}\left[\frac{\partial(e_2\, a_1)}{\partial i} + \frac{\partial(e_1\, a_2)}{\partial j}\right] + \frac{1}{e_3}\frac{\partial a_3}{\partial k}$$

$$\begin{aligned}
\nabla \times \mathbf{A} &= \begin{pmatrix} \mathbf{i} & \mathbf{j} & \mathbf{k} \\ \frac{\partial}{e_1 \partial i} & \frac{\partial}{e_2 \partial j} & \frac{\partial}{e_3 \partial k} \\ a_1 & a_2 & a_3 \end{pmatrix} \\
&= \left[\frac{1}{e_2}\frac{\partial a_3}{\partial j} - \frac{1}{e_3}\frac{\partial a_2}{\partial k}\right]\mathbf{i} \\
&\quad + \left[\frac{1}{e_3}\frac{\partial a_1}{\partial k} - \frac{1}{e_1}\frac{\partial a_3}{\partial i}\right]\mathbf{j} \\
&\quad + \frac{1}{e_1\, e_2}\left[\frac{\partial e_2\, a_2}{\partial i} - \frac{\partial e_1\, a_1}{\partial j}\right]\mathbf{k}
\end{aligned}$$

$$\Delta\, q = \nabla \cdot (\nabla q)$$

$$\Delta\, \mathbf{A} = \nabla\,(\nabla \cdot \mathbf{A}) - \nabla \times (\nabla \times \mathbf{A})$$